Universität Bonn

Physikalisches Institut

Towards a cryogenic operation of a dielectric haloscope

Juan Pablo Arcila Maldonado

Dieser Forschungsbericht wurde als Masterarbeit von der
Mathematisch-Naturwissenschaftlichen Fakultät der Universität Bonn angenommen.

Angenommen am:	29.09.2023
1. Gutachter:	Prof. Dr. Béla Majorovits
2. Gutachter:	Prof. Dr. Klaus Desch

Quiero dedicarle este trabajo a mi familia, por su incondicional apoyo.
Ata, Litis, Tasisi, Paola, Lili, Hernán, Delita, y mi muy amada madre.
Sé que no es fácil estar tan lejos, pero sé también cuan reconfortante es
para ustedes saber que durante este tiempo en Alemania encontré salud,
felicidad, crecimiento personal y académico.

Acknowledgements

I am deeply grateful for the support and care provided by the German healthcare system, which not only covered my needs but also allowed me to regain my health. I am constantly reminded of the unfortunate reality that many talented individuals are held back by health issues, unable to fully exploit their potential or access the means to improve their conditions. It is my hope that systematic disadvantages like these can be continuously reduced, and I strongly believe that the academic world should actively engage in this endeavor.

My heartfelt appreciation goes out to my family and friends for their unwavering support over the past two years. To Basfi, Angela, and Angie: your presence has made my experience in Europe more delightful.

I extend my sincerest gratitude to the University of Bonn for providing me with the opportunity to study in Germany. Throughout my time there, I faced various challenges that ultimately shaped me into a better and more prepared physicist. I thank my co-supervisor Prof. Dr. Klaus Desch for his genuine interest in my project and the invaluable advice he provided during the year, as well as Prof. Dr. Ingrid-Maria Gregor for listening to me when I needed it.

The Max Planck Institute for Physics deserves my deepest gratitude. From the moment I arrived, they believed in me and supported my journey. I want to express my appreciation to Dr. Hanrieder and Prof. Dr. Henn for coordinating and awarding the fellowship that had a life-changing impact.

Working on MADMAX provided me with invaluable skills and opportunities beyond my imagination. I am grateful to all my colleagues, including Anton, Johannes, Derek, Chang, for their kindness and support at the institute. The members in Aachen, Marseille, and Hamburg also provided stimulating discussions and support. Although the list is extensive, I must give a special mention to Dagmar and Chris, who helped me immensely with the cryogenic measurements.

Lastly, my immense gratitude goes to my supervisor at the Max Planck Institute, Prof. Dr. Bela Majorovits. Thank you for constantly challenging me, engaging in thought-provoking discussions, providing constructive feedback, and maintaining a perfect balance of professionalism and approachability. Above all, I am grateful for your unwavering belief in my potential. Finding an excellent supervisor is both important and challenging, and I am truly fortunate to have had you by my side.

Contents

CHAPTER 1

The QCD axion and its searches

The Quantum Chromodynamics (QCD) axion is a hypothetical particle proposed to solve the Strong Charge-Parity (CP) problem in particle physics, by which a CP violating term is allowed under the symmetries of the QCD lagrangian causing a dielectric dipole moment in the neutron[1–3], which, however, has not been observed experimentally [4–6]. By incorporating a spontaneously broken new potential $U(1)$ either before or after inflation, the QCD axion is generated along with new particles depending on the theoretical model [7], causing the value of this CP violating term to be dynamically driven to zero [8]. Having an allowed law that is not observed requires either an explanation as to why this effect cannot be measured, or a fundamental change in the way we have built our particle theory.

If this $U(1)$ potential is broken before inflation, causality over the small volume causes the value to be homogeneous across the universe. This possibility is referred to as the *pre-inflationary scenario*. On the other hand, in the *post-inflationary scenario*, there will be many causally disconnected patches with different values, which ultimately produces different predictions for the QCD axion mass [9]. In both cases, the range 1×10^2 to 1×10^3 μeV is allowed on most pre- and post-inflationary models, and especially well-motivated in the post-inflationary scenario. This will be one of the main motivations for the MAgnetized Disc and Mirror Axion eXperiment (MADMAX), as discussed below.

On the other hand, it was noted that under certain conditions, this new particle could also be the dark matter content in the universe [10–12]. Dark matter is the name that has been used to describe the unknown apparent mass content in the universe that does not interact with light as ordinary (or *baryonic*) matter but has a gravitational effect measurable in different cosmological and astrophysical observations. It has been estimated by different independent measurements across many orders of magnitude in space and time that there is around five times more dark matter than baryonic matter in the universe [13, 14], making the dark matter puzzle (i.e., *what is dark matter made of?*) one of the most critical research topics in astrophysics and cosmology.

Solving both puzzles *at once* has propelled the QCD axion to be one of the most popular and well-motivated dark matter candidates. Moreover, there is a relation of the QCD axion coupling strength and its mass [15], thus reducing the space of parameters of possible discovery, and marking a clear sensitivity goal for the experiments.

1.1 Axion searches

Most of the axion-search experiments exploit one of the theoretically allowed interactions between axions and baryonic matter or radiation [15]. Currently, the largest exclusion limits in the axion parameter space result from astrophysical observations, as axions can, in theory, be produced in diverse astrophysical environments, producing effects in stellar cooling and stellar evolution[16]. These limits are set mainly in the $m_a > 10\,\mathrm{eV}$ or $g_{a\gamma} > 1 \times 10^{-10}$ GeV as seen in Fig. 1.1. Moreover, there are also experimental efforts on Earth to directly detect the effect of these interactions. A more detailed review of Earth-based axion search experiments can be found in [17, 18].

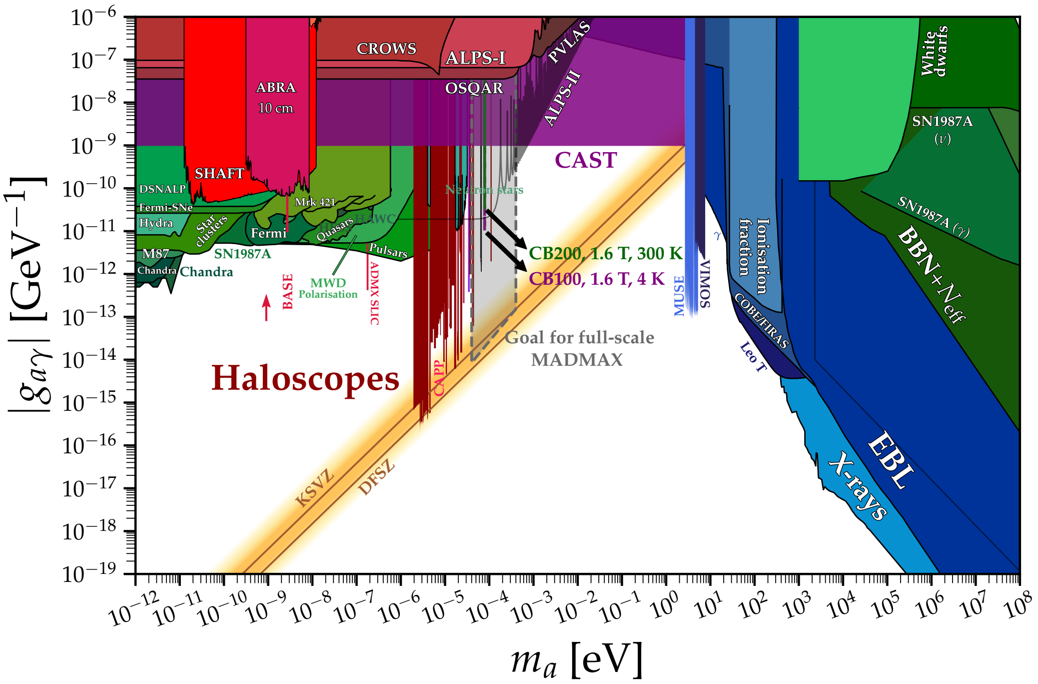

Figure 1.1: Current status of the axion-search experiments and astrophysical limits. The aspirational sensitivity of MADMAX, along with the sensitivity of the current prototypes is displayed around $m_a = 80\,\mu\mathrm{eV}$

In particular, for radiation-based detection, the lagrangian density that describes the interaction between axions and radiation includes $\mathcal{L} = g_{a\gamma}\mathbf{E} \cdot \mathbf{B}$ [19]. Because the axion occupation number is high, if the de Broglie wavelength at axion-like masses is larger than the experiment dimensions, and the measurement takes a time shorter than the axion coherent time, then it is possible to think of the axion content as a field that permeates space, called a degenerate Bose-Einstein condensate, oscillating with a frequency proportional to the inverse of its mass [20]. Therefore, the aforementioned interaction can be interpreted as follows: **By using a strong external magnetic field covering a given volume, the oscillating axion field can be converted to an oscillating electric field**[21]. The presence of axions in terrestrial experiments is predicted by the dark matter content of the Milky Way, and its dynamics are governed by our relative velocity through the axion field. Because the aim of this approach is to detect the axions in the galactic halo, these experiments receive the name of *haloscopes*, the first one being proposed in 1983 [22]. They usually consist of cavities that can resonate at a particular frequency, thus amplifying the possible axion-induced electric field. A cavity can be tuned (i.e., changing its resonance frequency) over a limited range of frequencies usually by using a tuning rod to physically change its dimensions. This is why the dark matter limits coming from haloscopes are characterized by deep narrow lines, as seen in Fig. 1.1, corresponding roughly to the resonance amplitude and bandwidth of the cavity, as well as to its limited tunability and volume. Some examples of axion haloscopes can be found in [19, 23–26]. MADMAX proposes a way to overcome the limited tunability of conventional haloscopes without compromising the reachable sensitivity. This is explained in Section 1.2.

Another approach to using the axion-photon coupling (also called the Primakoff effect) is to exploit the fact that inside the sun the photons in a hot thermal bath are immersed in a strong magnetic field, which can induce the production of axions at keV energies. Then, on Earth, an inverse conversion can be accomplished by using a large magnetic field to produce X-rays. In contrast to haloscopes, given that the produced axions are relativistic, the sensitivity of these experiments is almost independent of the axion mass[27]. Examples of this approach can be found in [28, 29], and correspond to the quasi-frequency-independent lines below $m_a \approx 1$ eV in Fig. 1.1.

1.2 The MADMAX experiment

As outlined in Section 1.1, cavity-based approaches can reach high sensitivities at the cost of limited bandwidth to search for axions. Moreover, when increasing in frequency, the volume of the cavity decreases, thus losing sensitivity at higher axion masses (usually $m_a \gtrapprox 50\,\mu\text{eV}$. This is problematic since the range of allowed masses extends for several orders of magnitude, and most of the post-inflationary scenario models motivate axion masses of 1×10^2 to 1×10^3 µeV, so broadband approaches are a necessity. MADMAX proposed a novel approach in which a quasi-broadband resonator, from now on called *booster*, could provide the sensitivity of conventional cavity experiments with a set of movable dielectric discs that could tune the resonance frequency. This experimental concept is known as a *dielectric haloscope* [21, 30, 31].

1.2.1 MADMAX aspirational design

The aim of MADMAX is to reach the sensitivity needed to search for the QCD axion between 40 to 400 µeV, corresponding to operating at frequencies between 10 to 100 GHz. The aspirational setup originally proposes to reach this sensitivity is shown in Fig. 1.2(a) and corresponds to the *goal for full scale* constraint shown in Fig. 1.1. To do so, a booster made up of many dielectric discs with tunable positions roughly evenly spaced is placed in the center of a strong dipole magnetic field, as shown in Fig. 1.2.

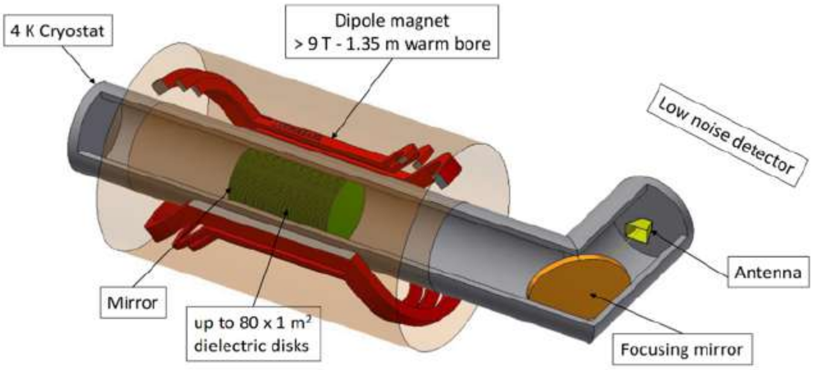

(a) MADMAX aspirational setup to reach the sensitivity required to probe the QCD axion between 40 to 400 µeV [21, 30].

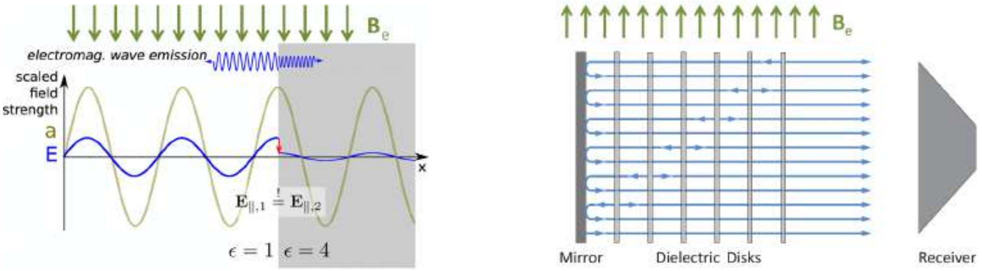

(b) Physical principle of the booster: Inside an external magnetic field, an axion field induces an oscillating electric field that features discontinuities at the interface with the dielectric surface. This produces the emission of electromagnetic waves.

(c) Effect when several discs are placed at convenient distances: Emission on each one can be added coherently. By placing a mirror on one of the sides, all the radiation can be directed to the antenna, and resonance at the *booster frequency* is possible.

Figure 1.2: The MADMAX experiment proposal: aspirational setup and signal amplification mechanism. Credits to the MADMAX collaboration.

The booster concept is based on the following principle: The electromagnetic waves emitted to compensate for the electric discontinuity generated by the difference between the parallel components of the axion-induced oscillating electric fields can be added up coherently if the distance between discs is convenient (see 1.2(c)). Moreover, by placing a mirror on one end of the booster, the radiation will reflect and resonate at some frequency. These two effects will effectively amplify the original power emitted by a single mirror, and be three to four orders of magnitude larger than the signal that would have been acquired if only the mirror without booster was placed inside the magnet. Mathematically, we define this effect as the *boost factor* of our experiment in Eq. (1.1).

$$\beta^2(\nu) = \frac{P_{\text{sig}}}{P_{\text{mirror}}}. \tag{1.1}$$

Where it is explicit that the boost factor is frequency-dependent. To understand how important the boost factor is for this experiment, consider the sensitivity that MADMAX can reach as a function of the different theoretical and experimental parameters

$$\begin{aligned} g_{a\gamma} = 0.2\,\text{GeV}^{-1} &\left(\frac{m_a}{1\,\text{GeV}}\right)\left(\frac{5\times 10^4}{\beta^2}\right)^{\frac{1}{2}}\left(\frac{10\,\text{T}}{B_e}\right)\left(\frac{1\,\text{m}^2}{A}\right)^{\frac{1}{2}} \\ &\times\left(\frac{\text{SNR}}{5}\right)^{\frac{1}{2}}\left(\frac{T_{\text{sys}}}{4\,\text{K}}\right)^{\frac{1}{2}}\left(\frac{1.8\,\text{d}}{\tau}\right)^{\frac{1}{4}}\left(\frac{\Delta\nu}{20\,\text{kHz}}\right)^{\frac{1}{4}}\left(\frac{300\,\text{MeV}\,\text{cm}^{-3}}{\rho}\right)^{\frac{1}{2}}. \end{aligned} \tag{1.2}$$

Where B_e is the external magnetic field applied, A the surface area of the dielectric discs, τ the integration time, and $\Delta\nu$ and ρ parameters determined by dark matter physics, namely, the axion-induced signal bandwidth which depends on the axion field velocity with respect to the experiment, and the axion density in our galactic halo, respectively [21].

To optimize our sensitivity $g_{a\gamma}$ we can integrate for longer times the received signal, build bigger boosters with larger surface area, use stronger magnetic fields, and increase the boost factor. Although all of these directions are investigated and pushed as much as possible, there is an intrinsic limit on most of them: The integration time scales with the fourth root, being the most inefficient term to maximize in order to increase our sensitivity. Hence, it is important to have a receiver with close to zero dead time. Then, even though the magnetic field is the only term that is linear, there is an experimental limit on the strength of a dipole magnetic field with a large bore to fit the booster. It has been demonstrated lately that it is possible to build a magnet with a field strength of around 10 T. Currently, a research and innovation partnership between Max Planck Institute for Physics (MPP), Bilfinger, and CEA in Saclay is being performed to approach that goal. As this task requires several years to be accomplished, in the meantime, MADMAX is using the Morpurgo magnet from European Organization for Nuclear Research (CERN). This magnet, first used in 1978, has a large warm bore of 1.6 m and a strong 1.6 T field used for the ATLAS experiment research and development [32].

Prototypes with discs of 100 to 300 mm in diameter are being tested. However, bigger discs are required to reach the final sensitivity target. On the one hand, this requires the production of large discs with very demanding tolerances. On the other hand, it demands a bigger magnet bore, so a compromise must be made between field strength and disc size, to reach the goal of 100 $\text{m}^2\,\text{T}^2$. The boost factor exhibits the highest potential for enhancement of the resonance output power, and it can be optimized by employing a larger number of dielectric discs and selecting the appropriate dielectric material based on its permittivity and tangent loss characteristics. This is why β^2 is a crucial parameter for MADMAX. Currently, prototypes with three to five discs are being investigated, while the aspirational setup proposes around eighty discs with a diameter of 1.2 m.

1.2.2 Prototype used and thesis goals

As a first approach to the MADMAX concept, a **C**losed **B**ooster of **100 mm** in diameter (Closed Booster 100mm (CB-100)) was built at MPP. The booster is closed to have well-defined boundary conditions, as open boundary conditions are too complicated when interested in the analysis of the wave propagation and the effect of resonances. Fig. 1.3 shows an exploded view of the prototype, which houses three sapphire discs as dielectric discontinuities.

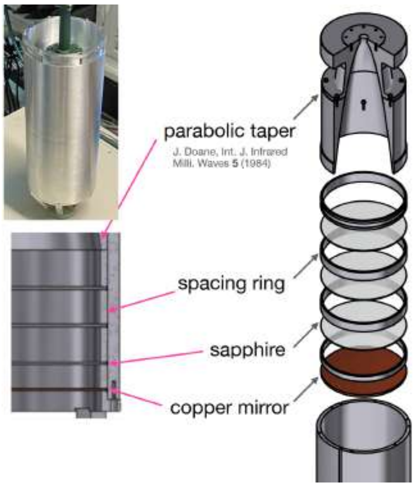

Figure 1.3: Exploded view of the current booster prototype, CB-100. Credits to the MADMAX collaboration

Inside the booster, the three sapphire discs are fixed in position using spacing rings. At the end of the cylinder, a copper mirror is placed to reflect the incoming Radiofrequency (RF) signals directing them to the parabolic taper that smoothly matches the waveguide impedance to the coaxial impedance connected on the other side, where the signal can be directed to the receiver chain and ultimately be read out. Sapphire is used because it offers a good compromise between high relative permittivity, low tangent loss, and the feasibility of fabricating discs with the needed diameter. With three discs, simulations from the collaboration have estimated the effective boost factor of the final setup to be of $\beta^2 \sim 700$.

The magnet used for the current prototype measurements and test runs is the Morpurgo 1.6 T dipole magnet located in the North Area at CERN [33]. This magnet provides the opportunity to test different booster prototypes and to perform the first MADMAX runs before the dedicated magnet is built and commissioned.

The current prototype setup CB-100 at room temperature ($\sim 300\,\mathrm{K}$) has been thoroughly characterized by the collaboration and has already been used for the first runs at CERN in 2022 and 2023, as detailed in Chapter 3 using the same setup up to the receiver (cables, waveguides, noise diodes, amplifier, and calibration standards) to minimize variability between the results due to hardware components. The sensitivity of this setup for an axion mass around $78\,\mu\mathrm{eV}$ can be obtained by plugging the mentioned values in Eq. (1.2). The experiment can probe Axion-like particle (ALP)s[1] around $m \sim 78\,\mu\mathrm{eV}$ and couplings $g_{a\gamma} > 1 \times 10^{-9}\,\mathrm{GeV}^{-1}$. Since this region in the parameter space has already been excluded [28], the main motivation of the first runs was the proof of principle of the concept and feasibility of a full setup calibrated and operating smoothly inside a strong magnetic field. However, to constrain unexplored regions, all the different experimental variables introduced in Eq. (1.2) have to be improved in parallel. Most of them are long-term projects that require a lot of understanding and funding to scale up. The only parameter that can be optimized at a lower cost and in a shorter timescale is the system temperature T_{sys}.

1.2.3 Goals for this thesis

Note that for a setup at a cryogenic temperature around $4\,\mathrm{K}$, the sensitivity would increase by roughly one order of magnitude with respect to the room temperature case. This is due to the fact that noise background generated by the thermal photons in the frequency range of 18 to $20\,\mathrm{GHz}$, where the measurements are conducted using CB-100, would undergo a decrease of two orders of magnitude. Consequently, the sensitivity, which scales with the square root of the power, would experience a corresponding increase of around one order of magnitude, allowing us to explore so far unconstrained regions for ALPs. Development of key technologies is required to approach the sensitivity needed to reach the sensitivity needed to probe the coupling predicted by the QCD theoretical axion models [7].

The challenges of a cryogenic operation of the dielectric haloscope are manyfold: At these frequencies (high compared to other cavity-based axion-search experiments), the setup, and in particular the boost factor β^2 are sensitive to changes of tens of micron in the propagation length of the RF signal, as the location of the resonance frequency and its magnitude depend on the geometry of the setup. Since thermal shrinkage from $300\,\mathrm{K}$ to single-digit temperatures can be in that order of magnitude or potentially even higher, we can assume that even though the same hardware is used for both the room temperature and the cryogenic run, in reality, the booster systems behave differently and hence it is needed to characterize independently.

Moreover, the systematic uncertainties induced by different RF components, thermal gradients in the RF cables, user-induced changes in the propagation lengths (for example, when

---

[1] Particles with properties similar to the axion but that do not follow the predicted coupling-mass relation for the QCD axion

reconnecting components), time-drifts of the setup calibration, and more, can also be of the same order as the precision needed to ensure a high boost factor.

The current prototype setup is calibrated at room temperature by manually performing a set of $O(10)$ measurements, which then serve as an input for simulations and data analysis. However, at cryogenic temperatures, manually performing these steps would require $O(10)$ thermal cycles that would increase by orders of magnitude the time required to do a full calibration, its cost (mainly by the price of liquid helium), and these alter its reproducibility.

To the best of our knowledge, a cryogenic calibration of this type at these frequencies has never been performed with the required accuracy. It is well known that many room-temperature calibrations at frequencies around and well above ours have been proposed for example for radio telecommunications and military applications (see e.g. [34, 35]). At the same time, lower-frequency cryogenic applications have also been devised for quantum computing applications [36, 37] and cavity axion search experiments [19, 26]. Increasing in frequency or decreasing in temperature brings new challenges to any project, and MADMAX will be a pioneer in the quest for high-frequency and low-temperature calibrations. This is the main purpose of this thesis.

CHAPTER 2

Fundamentals of radiofrequency measurements and booster determination

2.1 Impedance and the scattering matrix

The media through which a wave travels can be characterized by its impedance. There are several ways to define this quantity, such as a complex number in which the real part corresponds to the resistance of the media and the imaginary component to its reactance. It can be also described as the complex ratio between the voltage and the current in that medium (which is expected from the previous definition and Ohm's law). Finally, it also corresponds to the complex ratio between the electric and the magnetic field components of the traveling wave in that particular media.

In optics, it is common to describe the effects of a media in the propagation of light by the refractive index. When light passes from one media to another, some part is reflected and some are transmitted, depending on the relative difference between the refractive indices of both media. This is intuitively the reason why light seems to be deflected and partially reflected when crossing from air to water. The role of impedance in microwave engineering is the same as the refractive index in optics, and the same intuition is valid. When a signal passes through devices of different impedances, it will be partially reflected and partially transmitted depending on the relative difference of these quantities. When this happens (most of the time) both devices are said to be *impedance mismatched*. If, on the other hand, both devices have exactly the same impedance, they are said to be *impedance matched*, and full transmission of the signal (and null reflection) will be achieved.

As motivated by the lumped-element circuit formalism used to describe RF behavior, any transmission line can be described by a set of resistors, inductors, and capacitors that describe the frequency-dependent behavior induced by the line. For example, the impedance of an infinite azimuthally symmetric lossy coaxial cable is given by Eq. (2.1) [38].

$$Z = \sqrt{\frac{R + i\omega L}{C + i\omega C}}. \tag{2.1}$$

Where R is the series resistance, L is the series inductance, G is the shunt conductance, and C is the shunt capacitance. As can be seen in this simple example, the impedance is frequency-dependent, due to the capacitive and inductive terms. This is what makes *impedance-mismatched* setups unavoidable, and broadband *impedance matching* practically impossible.

To quantify how waves are reflected and transmitted through any component, the S-matrix formalism can be used. Imagine that an RF signal travels through transmission line 1 (TL1) characterized by an impedance of $Z_1(\omega)$and encounters transmission line 2 (TL2) with impedance $Z_2(\omega)$, as shown in Fig. 2.1. Then, the percentage of the wave that will be reflected back because of the impedance mismatch is given by Eq. (2.2)

$$\Gamma(\omega) = S_{11} = \frac{Z_1 - Z_2}{Z_1 + Z_2}. \tag{2.2}$$

This is expected, as it precisely corresponds to the relative difference between the impedances of both lines. Moreover, it shows explicitly that this coefficient is in general frequency-dependent. Finally, in microwave engineering, it is referred to as S_{11}. A first advantage of the S-matrix formalism can already be seen: If the wave now travels from TL2 to TL1 and we were interested in computing the reflection coefficient, in the S-matrix formalism this would naturally be labeled as S_{22}, because the signal came from port 2 and was reflected to port 2.

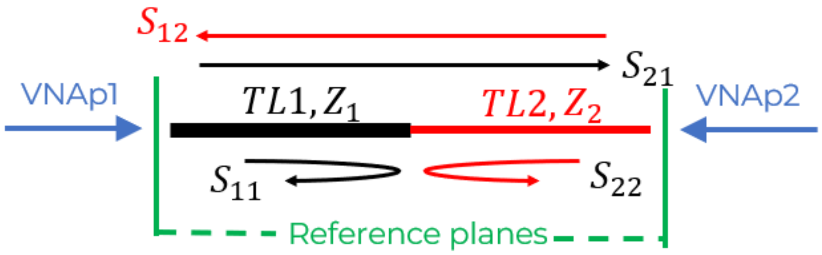

Figure 2.1: Sketch of how the S-parameters of a two-port transmission are defined. Here, simplified transmission lines represent two media where waves travel from both directions, being partially transmitted and partially reflected because of the impedance mismatch between the lines.

Therefore, to measure S_{11} and S_{22}, it suffices to connect the Vector Network Analyzer (VNA) to the beginning of the transmission lines (after calibrating it to move the reference plane to the needed position), send a signal at a particular frequency and measure the reflected part. Note that it is crucial to avoid any signal from port 2 from leaking into port 1 when the measurement of S_{11} is performed, as more signal would appear to be reflected (the reflected part from port 1 plus the leaked part from port 2). To avoid this, we can imagine that a fully absorptive element is placed on port 2 during this measurement so that any possible signal is absorbed before reaching the transmission lines. This is commonly referred to as *matching* the port. To sum up, in this example, when measuring S_{11}, port 2 has to be matched, and when measuring S_{22}, port 1 has to be matched

Naturally, with the setup of Fig. 2.1, it is also possible to send a signal through *VNAp1* and receive some of it on *VNAp2*. By conservation of energy, the received signal will always be less or equal to the emitted one, because some of it was reflected back, and some of the transmitted part was absorbed by the other line before arriving at the measuring port, except in the case where instead of having two lines, a device which generates power on its own is used, such as an amplifier. These devices are denoted as *active* components (in contrast to the *passive* ones). The parameter quantifying this transmission is denoted as S_{21}. As before, the reverse process is possible and denoted S_{12}.

We can call the network formed by both transmission lines as Device Under Test (DUT). This DUT has two ports through which the waves can enter or exit. The presence of the DUT alters the incoming signals and this alteration can be fully described by the four S-parameters here discussed, which form a rectangular *scattering* matrix S of 2 dimensions, where S_{12}, S_{21} give information about the transmission and S_{11} gives information about the reflection at port 1 when port 2 is matched. These values can be frequency dependent because the impedance is frequency dependent.

It is now possible to generalize this example as follows: The S-matrix of a n-port DUT is a $n \times n$ matrix with complex and frequency-dependent entries where the off-diagonal elements S_{ij} refer to the transmission from port j to port i while all the other ports are matched, and the diagonal elements S_{ii} quantify the reflected signal through port i, when the signal is sent through the same port and all the others, are matched. Moreover, the magnitude $\left|S_{ij}\right|$ is less than unity for passive components but can be higher for active ones. Finally, if for all frequencies $S_{ij} = S_{ji}$, the DUT is said to be *reciprocal* [38, 39].

2.1.1 Phasor and unwrapped phase

A single-frequency plane wave can be described by the equation:

$$E(x,t) = E_0 \cdot e^{j(2\pi\nu t - \mathbf{k}\cdot\mathbf{x})} \tag{2.3}$$

Here E is the amplitude of the wave, ν the frequency of the wave, t the time, $\mathbf{k}$ the wave vector, and $\mathbf{x}$ the direction of propagation. The phasor of the wave is obtained by dropping the spatial dependence. It is thus defined as

$$P(\nu,t) = E_0 \cdot e^{j(2\pi\nu t}, \tag{2.4}$$

such that the complete waveform can be described as

$$E(x,t) = P(\nu,t)\cdot e^{-j\mathbf{k}\cdot\mathbf{x}} \tag{2.5}$$

where the phasor contains all the information about time propagation and phase. $P(\nu,t)$ can be plotted in the complex plane as shown in Fig. 2.2.

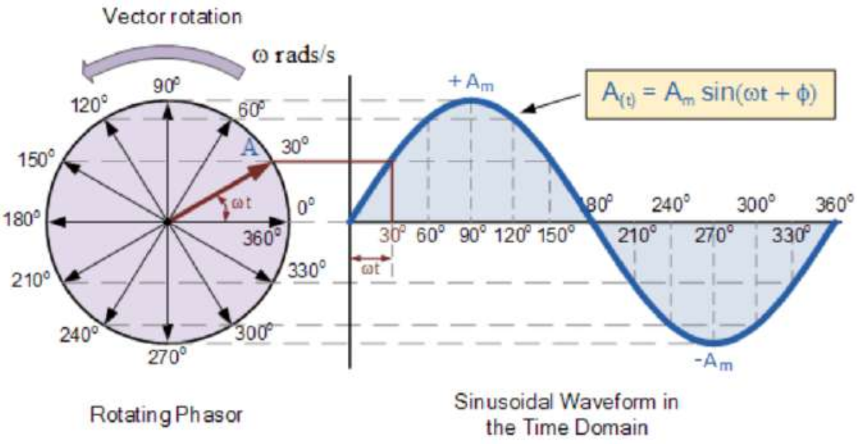

Figure 2.2: Phasor of a wave in radial coordinates. The magnitude of the vector represents the magnitude of the wave, and the phase measured from the positive x-axis represents the phase of the wave. There is a direct connection between the time-domain periodicity and the phasor angular periodicity. Credits to [40].

On this plot, when a wave traverses a full period, then $P(\nu,t) = P(\nu,t+2\pi)$, so the phasor ends up in the same point but does a full cycle in the complex plane by changing its phase by 2π rad $= 360^\circ$. If the wave traverses a length corresponding to 2λ, where λ is its wavelength, the phasor will circle twice and end up at the same point. Therefore, when studying the phase of the wave, it cannot be distinguished whether the wave has propagated any distance or an integer amount of wavelengths. A useful definition for this is thus the **unwrapped phase**, which consists of adding up the phase instead of periodically measuring in the interval $[0,2\pi]$. Therefore, after traversing two full wavelengths, the unwrapped phase will be 4π rad $= 720^\circ$.

Because the wavelength decreases with increasing frequency, the unwrapped phase values at higher frequencies are correspondingly higher. Considering that the systematic uncertainty induced by the VNA phase resolution is constant across frequencies, measuring the unwrapped phase at the highest possible frequency can provide the most precision in determining the length that the VNA signal traveled. This fact is largely used in this thesis.

2.1.2 Smith chart

A useful tool to visualize the complex S parameters as a function of frequency is the Smith chart, developed by Phillip H. Smith in the 1930s. The Smith chart is a graphical tool extensively used in RF and microwave engineering. It simplifies complex impedance calculations and aids in designing and analyzing RF circuits. It consists of a polar plot that visualizes complex impedance in the complex plane. The building elements are a unit circle representing normalized impedance (impedance divided by the characteristic impedance of the transmission line), *resistance circles* concentric around the unit circle to represent the constant resistant values, and *reactance arcs* as radial lines extending outward from the center to represent constant reactance values, intersecting the resistance circles at various points. Fig. 2.3 shows how the chart looks and the points corresponding to the Open, Short, and Load standards.

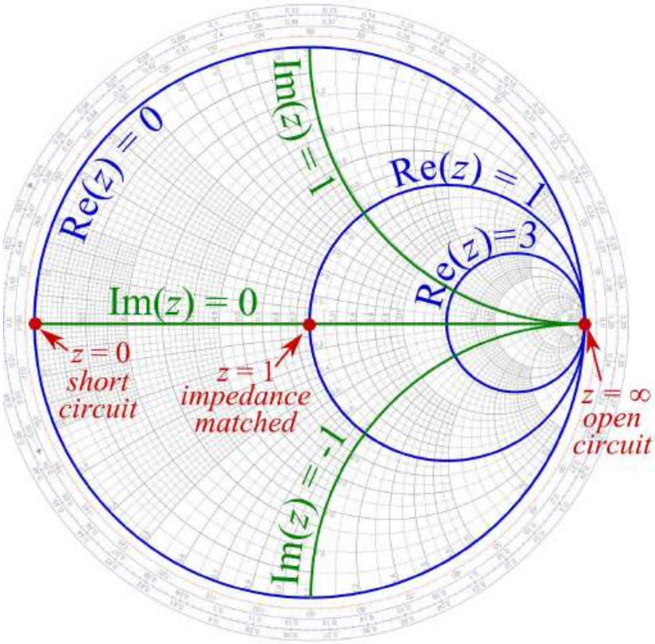

Figure 2.3: Construction of a Smith chart and ideal open, short, and load standards visualized. Credits to [41]

It is important to note that when a transmission line of finite distance is between the reflection point and the reference plane, the phase will accumulate a phase (360° per wavelength) when traversing the transmission line. Imagine that a transmission line has exactly a length of one wavelength at 18 GHz. Then, the phase accumulated by a phasor representing a wave that traverses it is exactly 360°. When frequency continuously increases, the phase does as well, because the wavelength decreases while the transmission line length is constant. Therefore, the phase in the phasor (related to the imaginary component in the Smith chart) becomes a continuous line with constant magnitude.

2.2 (De-)Embedding networks

In Fig. 2.1 the DUT between the reference planes correspond to the network composed by the transmission lines (TL) 1 and 2 and is characterized by the S-matrix S_{DUT}. Note that this DUT is composed by two 2-port devices, as each transmission line has one input and one output, therefore, it is possible to characterize each one with another S-matrix, namely S_{TL_1} and S_{TL_2}. We say that the DUT is the network resulting from *embedding* the networks of both transmission lines. A natural question is to ask: given S_{TL_1} and S_{TL_2}, can I obtain S_{DUT} without additional measurements? In theory, this is possible, and a simple expression can be obtained if we use the *transfer matrix* (T-matrix) approach. Here, the S-matrices can be converted to T-matrices by well-known formulas [38, 42], then, the relation between the *cascaded* transmission lines and the DUT is simply given by Eq. (2.6)

$$T_{\mathrm{DUT}} = T_{\mathrm{TL}_1} \times T_{\mathrm{TL}_2}. \tag{2.6}$$

Note that Eq. (2.6) can be solved for any of the networks. For example, given the measurement sketched in Fig. 2.1, we might need to obtain the S-matrix of TL_2 only. This could be done by multiplying the inverse T-matrix of TL_1 from the left on both sides, thus obtaining $T_{\mathrm{TL}_1}^{-1} \times T_{\mathrm{DUT}} = T_{\mathrm{TL}_2}$, which can then be transformed as explained in [42] to S_{TL_2}. This process is referred to as the *de-embedding* of TL_1 from the measurement and will be essential throughout this work to de-embed, for example, the RF components connecting the cold stage of the setup inside the cryostat to the exterior where the VNA is. In practice, however, de-embedding can cause additional uncertainties and lower the precision of the measurements [43].

2.3 Low noise amplifiers and noise model

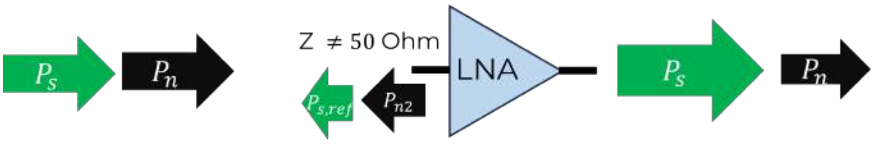

Figure 2.4: Incoming thermal noise from a calibration standard (or the booster) will interfere with its reflection from the LNA input, as well as with the noise emitted by the amplifier.

An amplifier is an active electronic component used to amplify a signal on a specific bandwidth to a certain level usually measured in decibels (dB). This is achieved by providing energy in the form of a bias current and voltage to the component. In a first approximation, the input impedance of an amplifier is designed to match the impedance of the other setup components, as maximum power transfer might be desired. However, this also means that the incoming noise will be amplified, as the device cannot distinguish between noise and signal. It is also possible to maximize the impedance mismatch on the input port to minimize noise from being amplified. By the same reasoning as before, this also minimizes the signal of interest. For applications where the signal is low compared to the noise, it is important to use an amplifier that does not add considerable additional noise while still providing high gain. This device is called a Low Noise Amplifier (LNA) and is extensively used in different RF applications such as in radio astronomy [44], telecommunications [45], and axion searches [46]. Fig. 2.4 presents a sketch showing how a LNA interacts with the incoming signal and noise.

Usually, LNA are manufactured by featuring an impedance mismatch on the input port, which optimizes the compromise between high power transfer and low noise transfer [47]. This can be achieved by creating an impedance-transforming path between the RF input and the gain point of the amplifier, somewhere inside the device, as sketched in Fig. 2.5. Note that we assume in our model that the noise from the amplifier is generated at the same point where the gain happens.

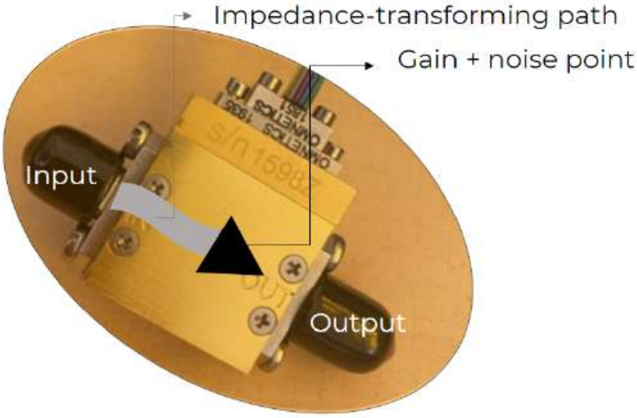

Figure 2.5: Simple sketch of how we are modeling the LNA. There is an impedance-transforming path of finite length between the input and the region where the gain happens, which we assume to be point-like.

The amplifier is an active device and generates its own noise. It is important to model the noise of the LNA because in the CB-100 setup, the LNA noise is reflected by the copper mirror into the input of the amplifier, which will cause it to interfere either constructively or destructively depending on the wavelength with the incoming noise from other components, e.g., CB-100. Currently, MADMAX models the noise generated by the LNA with three *a priori* unknown variables: A noise voltage V_n, a noise current I_n, and the correlation angle between both sources ϕ_n [38, 48].

Since these three variables are initially unknown, three independent noise measurements have to be performed to characterize each. When connecting a short, the current will flow through the minimum resistance path, thus bypassing the effect of the current source, which is connected in parallel to the LNA. Then, when connecting the open standard, as it behaves ideally as an infinite resistance device, by the same principle, all the current will flow in parallel, thus bypassing the noise source. In the last step, the load is connected, impedance matching the path, so current will flow through both, and information about the correlation between V_n and I_n can be obtained.

Finally, these three pieces of information can be gathered to fit the unknown parameters to the measurements in simulations.

2.4 Noise temperature and power calibration

The thermally generated noise power P_n generated by a resistor with resistance R at temperature T measured at a frequency ν with a resolution bandwidth B is given by Eq. (2.7)

$$P_\mathrm{n} = \frac{V_\mathrm{n}^2}{4R} = \frac{h\nu B}{e^{\frac{h\nu}{kT}} - 1}. \tag{2.7}$$

Where h is the Planck constant, and k the Boltzmann constant[38]. Usually, in radiofrequency applications, where frequencies and temperatures are high, $\frac{h\nu}{kT} << 1$, therefore, Eq. (2.7) can be simplified to

$$P_\mathrm{n} = kBT. \tag{2.8}$$

Eq. (2.8) is usually the expression used in our case. With the usual settings of our experiment, it can be seen that the relative error between both expressions at a frequency of 20 GHz and room temperature of 300 K is around 0.2 %. However, when the cryogenic operation is achieved, and the temperature is reduced to e.g. 4 K, the relative error will increase to 12 %. Therefore, care must be taken not to use the simplified version, but the full Planck radiation theory equation shown in Eq. (2.7).

The **noise temperature** T_e of any component is defined as the temperature of an equivalent black body that emits white noise with a power corresponding to the power measured by the component. Let this power be N_0, then the noise temperature is given by Eq. (2.9)

$$T_\mathrm{e} = \frac{N_0}{kBG} \tag{2.9}$$

Which is obtained by re-arranging Eq. (2.8) and where G is a possible gain if there is an additional amplifier in the setup (which is the case for our measurements).

The need for an amplifier comes from the fact that internal noise in the spectrum analyzer is usually higher than the thermal noise from a passive component, and hence would not be possible to measure it directly. In principle, by exactly knowing the gain of the amplifier used, and then measuring the noise power emitted by the component isolated from any thermal surrounding such as interconnecting cables that are also at room temperature, then Eq. (2.9) would be enough to find the equivalent noise temperature of the circuit. Usually, this is not practical, hence, an alternative approach is often performed, which is referred to as the **Y-factor calibration**.

In this approach, two matched resistors at different temperatures are measured. The noise power measured for each will be different, with the change being linear with temperature, as Eq. (2.8) suggests. With these two measurements, a slope for this linear behavior can be calculated. This is usually called Y-factor calibration in the literature. It relates the uncalibrated power measurement to the equivalent noise temperature, which is not receiver-dependent.

For the MADMAX CB-100 receiver calibration, a noise diode is used. When it is turned off, it acts as a matched resistor (also called a *load*) at room temperature, whereas when it is powered by a 28 V DC power supply, it emits thermal radiation with a Excess Noise Ratio (ENR)[1] of ~ 22.37 dB, followed by an attenuation of –30 dB. Therefore, the effective ENR is of $\sim -7.63\,\text{dB} \approx 0.17$. This means that the power emitted by the noise diode in this position corresponds to $\approx 300\,\text{K} \times (1 + 0.17) \approx 350\,\text{K}$.

Therefore, the *hot* and *cold* loads on our setup correspond to matched resistors at 350 K and 300 K respectively, corresponding to a difference of ~ 17 % between both. The 30 dB attenuator is needed to reduce the emitted power by the diode which could saturate the amplifier and to ensure the impedance match between the noise diode and the rest of the setup.

After performing both measurements, the calibrated noise temperature of a device can be expressed in terms of the Y-factor as in Eq. (2.10)

$$T_e = \frac{T_\mathrm{c} - YT_\mathrm{h}}{Y - 1}(1 - |\Gamma|^2) \tag{2.10}$$

Where $T_\mathrm{h}, T_\mathrm{c}$ are the hot and cold temperatures of the noise diode and Γ the reflection coefficient on the LNA input. This equation was obtained from [38] but modified to include the mismatch in the LNA.

Note that if in the denominator of Eq. (2.10) $Y \approx 1$, the expression becomes very sensitive to small changes in the Y-factor calculated. This is why in the literature [38] is recommended that the two temperatures are considerably different from each other, such that a Y-factor much greater than 1 (i.e., greater than 2) can be obtained, thus reducing the uncertainty on the equivalent noise temperature.

It is important to check that the Spectrum Analyzer (SA) does not saturate with the incoming signal, which could happen if the amplifier gain is too high. The amplifier cannot be removed because the receiver chain would change and the calibration would not correspond to the system used for the measurement campaign. Therefore, the maximum values for power input in the analyzer must be checked before proceeding. In this case, it corresponds to 30 mW, which is considerably higher than the expected noise power input for all the measurements performed for this experiment.

It is also logical to remove the baseline of the SA before performing the Y-factor calibration:

---

[1] The ENR is defined as the ratio between the power emitted and the reference power, which in this case corresponds to the power emitted by a matched resistor at room temperature

the receiver system, in this case, the SA plus the RF cable used to connect it to the device under test, are also emitting noise, partly thermal and partly electronic. The SA operates with active components that need to be used to perform the measurements. These components include, for example, local oscillators and amplifiers which require a constant voltage and current and which will produce additional noise that will affect both the *cold* and the *hot* measurements. Therefore, this internal noise needs to be characterized and removed from the diode measurements, to truly approach the expected noise temperature emitted by it. To do so, the load standard can be connected at the end of the cable, effectively match-terminating[2] the receiver system, such that no external noise is measured and no internal noise is reflected back to the analyzer.

2.5 Receiver and its sensitivity

The power in the RF regime is usually measured with a receiver [38], a common RF tool made up of an antenna to convert the RF electromagnetic signal to an electrical signal, and subsequent stages where the power corresponding to the measured signal is computed as a function of frequency. The principle used to detect this power is called *heterodyne detection*, in which the incoming high-frequency signal (of frequency ν)is mixed with a locally generated oscillating signal of frequency ν_{LO} to obtain two output waves, one with a higher frequency $\nu + \nu_{LO}$ and the other one with a lower frequency $\nu - \nu_{LO}$ [49]. The up-converted signal can be filtered out, while the down-converted one can be processed and digitized (taking into account that the maximum frequency that can be digitized by the instrument is limited by its sampling rate, according to the Nyquist sampling theorem [50].

In our case, the received used is a SA[51], a commercial specialized instrument used for RF research, which has a built-in receiver system to measure the power incoming from different components in the radio frequency range.

One of the governing equations for receivers is called the radiometer equation, as it describes the sensitivity that can be achieved by the receiver system. This equation can be derived from the central limit theorem [39] and is shown in Eq. (2.11)

$$\sigma_T = \frac{T_{\mathrm{sys}}}{\sqrt{B\tau}}. \tag{2.11}$$

Where σ_T is the RMS of the calibrated measured power, T_{sys} is the system noise temperature of the DUT, B the integrated bandwidth (also called here Resolution BandWidth (RBW)) and τ the integration time. Moreover, solving Eq. (2.11) for τ, one obtains

$$\tau = \frac{T_{\mathrm{sys}}}{B\sigma^2}. \tag{2.12}$$

This shows that it is possible to measure the lifetime of the experiment by studying the evolution

---

[2] attaching a 50 Ω resistor to maximize absorption and minimize reflections on a particular port

of the inverse variance of the signal measured.

2.6 VNA and its calibration

The VNA is a measurement instrument capable of emitting and receiving radio-frequency signals interacting with a DUT. By using a complex setup of active components such as amplifiers and local oscillators, as well as passive ones such as directional couplers, filters, and attenuators, it can compute the S-parameters of any device by using either homodyne of heterodyne detection to measure the quadrature components of the signals (magnitude and phase). The VNA used throughout this project was the Anritsu MS4647B [52].

To obtain a precise measurement, a *calibration* needs to be performed to understand and minimize the systematic errors associated with the instrument. A detailed explanation of the systematic errors that can be assessed by calibration can be found in [53].

Usually, a VNA has two ports, so a full measurement of a 2-dimensional S-matrix can be performed at once. If needed, however, only one of the ports can be used, if the DUT is a one-port device or a tiered calibration[54] is planned. Accordingly, there are one-port and two-port calibration procedures. As explained in [53, 55], a one-port calibration requires at least three independent measurements of devices with known RF response, whereas the two-port calibration requires at least seven. Then, these measurements and expectations can be used to implement a system of linear equations and find the values for each systematic error parameter. Finally, given a measurement of any DUT, a correction with the found parameters is applied to retrieve the *actual* S parameters of the device with the systematic uncertainties from the VNA corrected for.

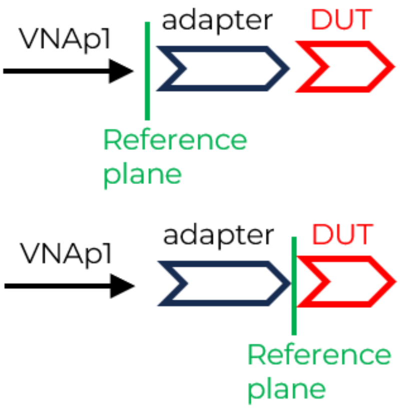

Figure 2.6: Effect of the VNA calibration. *VNAp1* denotes the first port of a VNA, which is used to measure a one-port DUT. Above, the calibration is performed to the tip of the VNA port, while below, the calibration is performed by connecting the calibration standards to the tip of the adapter, where the DUT is shown.

These calibrations are performed by plugging the calibration standards (short, open, load, mismatch, etc.) to the end of the VNA cables. This means that after the calibration is done, the systematic uncertainties from the instrument until the tip of the aforementioned cables will ideally vanish, this point is called *reference plane*. All the electronics behind this plane can be schematically replaced by an unphysical point-like source or receiver However, naturally, if a new cable, adapter, or component is added after the reference plane and before the DUT, its systematic uncertainties will not be corrected by the previous calibration, thus, a recalibration that includes these new intermediate components needs to be performed to maintain the precision of the measurement. By recalibrating, the reference plane will be *moved* to the new point where the second calibration was done. Fig. 2.6 shows this schematically. Another way to understand this process is by considering in this figure that if measuring without moving the reference plane, the S-parameters obtained will not describe the DUT only, but the embedded device with an adapter, i.e., the product between the T-matrices of the DUT and the adapter.

2.7 Booster and boost factor determination

The booster geometry determines its reflectivity behavior and the boost factor. A prediction of the position and shape of the booster resonance is provided by 1D simulations of the setup, for the reflectivity measurements, this allows to test the boost factor, however, it is not a direct measurement. As we need to take into consideration the differences in hardware that may alter the boost factor. Therefore, additional measurements are necessary.

The measurements that we do to determine the boost factor are mainly two: a reflectivity measurement with the VNA to obtain the group delay as a function of frequency, and a power measurement with the receiver, in our case, the SA, to obtain the power spectral density. These measurements also provide an estimation of the systematic uncertainties in determining the boost factor, as the systematic uncertainties of the measurements and mechanic tolerances of the booster geometry can be used to run Montecarlo simulations to obtain a systematic uncertainty in the boost factor. for CB-100, in both cases, measurements are performed in the 18 to 20 GHz bandwidth where many features can be observed, most notably the oscillation of the system temperature as a function of frequency expected from coherent self-interference of the LNA noise and a peak or dip-like structure due to the booster itself. The latter is centered at a frequency highly correlated to the peak seen in group delay, possibly frequency shifted by the different hardware with respect to the VNA. These features are also studied in a 40 MHz bandwidth centered at the booster behavior at resonance of interest, where the booster resonance can be studied in more detail with increased resolution. It is also at this smaller bandwidth where the data is acquired over a longer period of time for ALPs searches with the receiver system, in our case, the SA.

2.7.1 Group delay and phase stability

One of the derived measurements from the VNA of great utility for MADMAX is the group delay. This quantity is formally defined as the time derivative of the phase accumulated by a wave traveling through a transmission line or waveguide of finite electrical length and measures the time elapsed between the emission and arrival of a signal. A typical group delay measurement of CB-100 is displayed in Fig. 2.7.

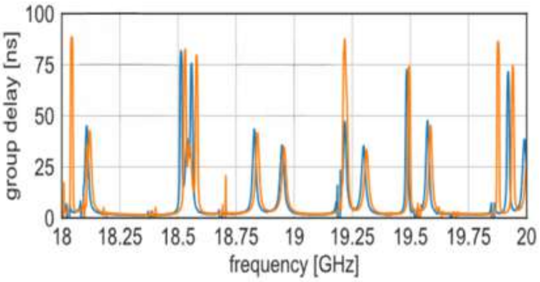

Figure 2.7: Measurement of the group delay as a function of frequency for CB-100. blue and orange are simulation and measurement, respectively.

Group delay can be a measure of the resonances inside CB-100. This is because, at the resonance frequency, the reflected power stays inside the cavity (resonating) for a finite time before coming back to the VNA, thus increasing the time taken for the signal to reach back the instrument. The peak at around 18.96 GHz corresponds to the booster frequency for the fundamental mode of the booster, mostly dependent on the distance between the mirror and first disc, while the other peaks correspond to resonance frequencies of different modes, that in our case are considered undesired as they do not couple as efficiently to the theoretically expected axion-induced field.

Systematic uncertainties in the group delay can be produced by the phase instabilities caused by the instrument's resolution, calibration degrading as a function of time, thermal shrinking or dilation as a function of temperature, user-induced systematics due to small differences in the connections made, etc. All these effects cause the effective electrical path traversed by the wave to change, thus changing the accumulated phase and the group delay.

2.7.2 Power measurement and noise interference

The other measurement considered to determine our boost factor and its systematic uncertainties is based on measuring the thermally generated power from the system as a function of frequency, with frequency resolution ensuring the coherence of the radiation. Thermal noise is broadband and in general totally uncorrelated Gaussian noise. Under this assumption, no interference between the noise produced at time t and at time $t' \neq t$ should occur. However, there are different mechanisms that can induce a noise correlation, which as a consequence produces noise to interfere with itself.

Some of these mechanisms are the use of narrow-frequency filters and reflections, both of which are present in the CB-100 setup: On the one hand, the booster itself acts as a frequency-dependent filter, depending on the resonance frequencies. On the other hand, the noise emitted from the LNA reflects back at the booster mirror and reaches the amplifier input again. Like this, if filtered narrowly, constructive or destructive interference of the LNA noise with itself can be produced. Therefore, the electrical length between the booster and the amplifier input is crucial in determining the shape of the interference. Therefore, it is possible to gain knowledge about the setup geometry and the booster frequency by studying the noise-interfering pattern measured with the SA coupled directly to CB-100. This measurement is shown in Fig. 2.8.

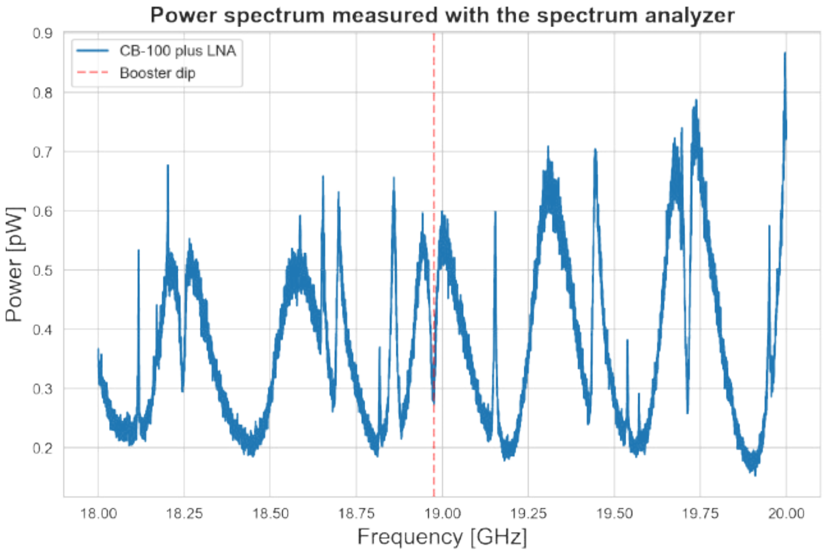

Figure 2.8: power spectral density measured with the SA for the system made up of CB-100 connected to the LNA. In red, is the location of the booster resonance for the desired mode.

Here, different noise-interfering effects are visible: The most evident one is an oscillation of the measured power as a function of frequency with a period of roughly 350 MHz. This corresponds to a wavelength of roughly $\lambda = c\nu^{-1} \approx 90\,\mathrm{cm}$), which is determined by twice the length of CB-100.

Another feature of this figure is the different narrow spikes. These are due to thermal noise coupling to the different modes of the system. Hence, at the frequency of these modes, more noise power is incoherently added to the system noise. As these modes are mostly narrow, they always appear as peaks.

Furthermore, several peaks and dips can be seen with similar bandwidths. These correspond to some of the resonance frequencies inside the booster. The one at the center marked with the dashed line corresponds to the resonance that we are interested in, and that is measured with higher resolution in the 40 MHz measurements. These features arise because the noise coming from the LNA travels inside the booster system and reflects back in the mirror. This reflected noise is correlated with the incoming noise and adds up constructively or destructively depending on the frequency and the path traversed. Therefore, whether the features are peaks or dips is defined by the electrical length between LNA and booster. For the configuration in 2023, the booster resonance of interest resulted in a noise dip, that from now on we call the *booster dip*.

From the explained measurements, it is evident that understanding the amount of noise coming from the LNA, as well as its input impedance and its distance to CB-100 is key to understanding the noise measurements and ultimately the boost factor. The interpretation of these measurements, most notably the boost factor extracted from the noise model and reflectivity behavior of CB-100, are limited by the precision that can be achieved when measuring electrical paths between components, i.e., by the phase resolution, stability, and reproducibility of the setup, and in particular, of the components between the LNA input and CB-100.

To sum up, being able to measure precisely the phase of the arriving signal is of utmost importance, as systematic deviations in these measurements affect the estimation of the boost factor significantly.

CHAPTER 3

Room temperature calibration of a closed dielectric haloscope

During spring 2023, a MADMAX CB-100 data run took place at the North Area, CERN, using the 1.6 T Morpurgo dipole magnet. The aim of this run was to understand the operation of the room temperature setup using the prototype CB-100 and the SA to extract the data from which ALPs limits could be derived. To perform these measurements, we did a full calibration both at MPP and at CERN, once all the equipment had been transported, to ensure that there were no changes induced by mechanical movement of the parts or additional Radiofrequency Interference (RFI) from the surroundings. The calibration steps were all done manually because the setup was at room temperature. However, the cold calibration will need the same steps, so understanding and calibrating the experiment during this campaign served as a hands-on learning experience to understand how the prototype system works and is characterized.

3.1 Calibration Measurements at MPP and at CERN

The setup used to perform the calibration as used at CERN is shown in Fig. 3.1. Each of the components used is described in Table 3.1.

The RF cable used should not be too lossy (no more than $\sim 3\,\mathrm{dB\,m^{-1}}$) and needs to be phase stable (in the order of single-digit degrees variation at 20 GHz). To ensure this, we minimize the mechanical movement of the cable. Once the cable is selected, it should not be changed during the entire run, as the Y-factor calibration also calibrates its attenuation.

The necessary measurements performed for obtaining the LNA noise model parameters are shown in Table 3.2. Both are performed in a 2 GHz and a 40 MHz span as explained in Section 2.7. After taking all the measurements required and following the procedure outlined in Section 2.4 it is possible to obtain the equivalent noise temperature for each measurement as a function of frequency. We automated and incorporated the calculation of the equivalent noise temperature as a function of frequency for individual measurements in the function

Hardware component	**Description**
Keysight SA UXA N9040B [51]	Spectrum analyzer used for the measurement campaign both at MPP and CERN .
1: LNA LNF-LNC6_20C 1675Z [56]	Low noise amplifier rated for operating between 6 to 20 GHz with gain around 32 dB used to amplify the noise from CB-100 to a power detectable by the spectrum analyzer. Needs also a dedicated Direct Current (DC) power supply
(not shown)DC-power supply LNF-PS3b for the amplifier [57].	Allows to bias the amplifier with voltages up to 2.4 V and currents up to 50 mA.
2: Calibration standards	From Rosenberger, namely short 02b68, open 223300, and load 01b50. They are used for the determination of the internal noise of the LNA and the baseline of the SA. Specifically, we used the Open02b13, Short02b70, load01b80, and a mismatch with a standing wave ratio of 1.5 and reference 46A24. All these standards are 1-port K-male connectors.
3: Noise diode W149 from NOISE COM INC.	Provides a voltage-tunable effective noise temperature. Thus, it is used as both the *cold* and the *hot* loads for the power calibration. When it is powered with a DC voltage of 28 V, it outputs a ENR between 22.19 to 22.31 dB in the frequency range of 18 to 20 GHz.
(not shown) Power supply Agilent E3630A [58]	Used to power the noise diode. To protect the equipment, a conventional multimeter is also used to verify the power supply voltage lecture before connecting it to the diode.
4: 30dB attenuator	Connected behind the noise diode, provides impedance matching between the LNA and the diode, and prevents the LNA from saturating.
5: Rosenberger male-2.92mm to male-2.92mm connectors (mk-mk) cable	Connects the SA to the LNA output. It has to be long enough such that the receiver is at a safe distance from the strong magnetic field. For this run, we used two cables connected in series, each one 3 m long.

Table 3.1: Hardware components and brief description for the power calibration

Power_to_noiseT in the *MADMON*(see Section 3.2) monitoring script. This enables the calibration of each new data file on the fly. The impedance of the LNA input, needed to compute

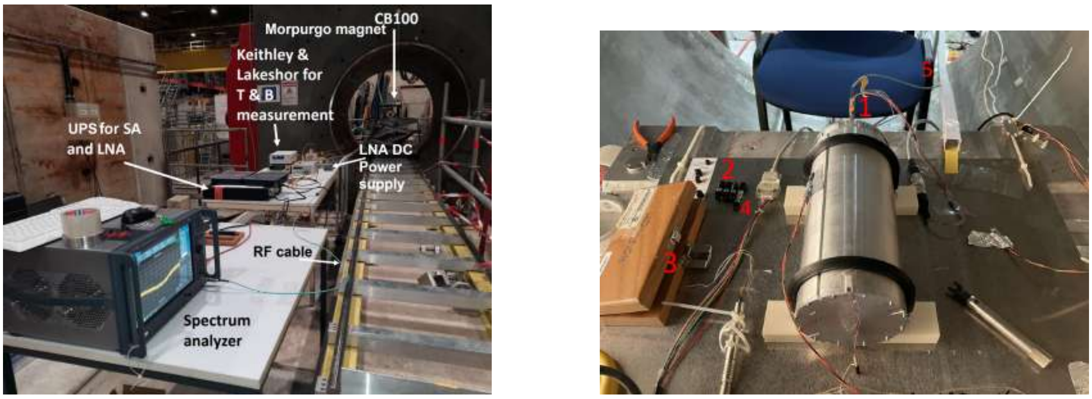

Figure 3.1: Setup used for the noise calibration of the prototype. The description of each numbered component is shown in Table 3.1

the reflection coefficient Γ in Eq. (2.10), was obtained by measuring it with the VNA in a separate measurement (see Section 2.3). The results are shown in Fig. 3.2.

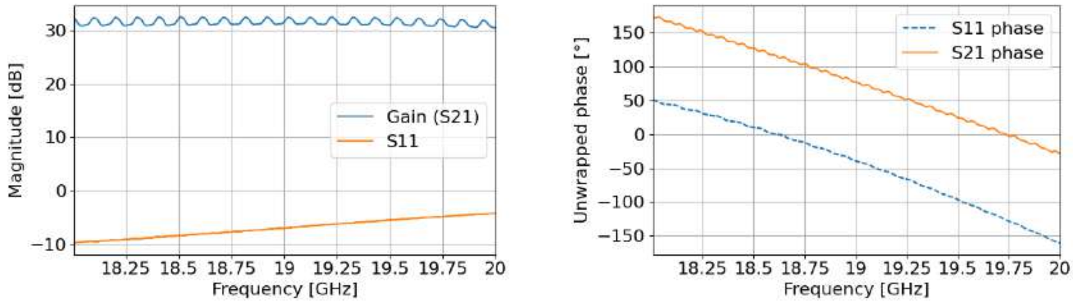

Figure 3.2: Relevant S parameters for the LNA LNC6_20 characterization at room temperature in magnitude and phase for the frequency range 18 to 20 GHz.

To measure high-gain amplifiers with the VNA it is important to lower the output power from the ports to around −40 dBm. From the datasheet [52], the maximum input power not to compromise the VNA is 27 dBm. With a gain of roughly 32 dB, the instrument saturates and does not display the correct gain value if the input power on the LNA is greater than −30 dBm. Regarding S_{11} it can be seen that in the frequency range of interest $|S_{11}| > -10\,\mathrm{dB}$. This reflection is enough to detect the reflected signal and determine the reflectivity at the input port needed for the LNA noise model.

Measurement	**Purpose**
load	Spectrum analyzer baseline noise
LNA with load	correlation between noise voltage and current in LNA noise model
LNA with open	Noise current in the LNA noise model
LNA with short	Noise voltage in the LNA noise model
LNA with mismatch	cross-check measurement for the LNA noise model
LNA with Noise diode ON	warm load for power calibration
LNA with Noise diode OFF	cold load for power calibration
LNA with CB-100	Geometry, booster frequency, and DAQ run

Table 3.2: Calibration measurements performed with the spectrum analyzer. Details on the purpose of each measurement can be found in Section 2.3 and Section 2.4.

3.1.1 Calibration at MPP

Prior to the measurement campaign at CERN, all the components of the setup to be used were characterized at MPP. It is in principle possible that some of them may have changed their expected behavior due to continuous use, exposure to variable environments such as different temperatures or high magnetic fields, mechanical shocks during transportation, etc. Therefore, we performed a full calibration and compared it to the results obtained in the previous year considering that all the hardware up to the receiver (waveguides, cables, standards, diode, and amplifier) were the same on both setups, as well as with the expected RF and noise behavior.

There were notably two differences seen in these results with respect to the measurements performed in 2022: First, when characterizing the noise response of the LNA LNF-LNC6_20C 1598z, the three calibration standards were connected to the amplifier input, and then measured at the output port with the SA. In Fig. 3.3 the individual equivalent noise temperatures are compared for measurements taken in 2022 with the measurements IN 2023 using the same LNA (MPP) and for a set of measurements taken at CERN with a different amplifier (*spare LNA*). It can be seen that the behavior of the amplified load is similar in both cases. However, the expected noise oscillation on both the short and the open cases, which comes from noise interfering with itself constructively and destructively has been altered between the 2022 and the MPP 2023 measurements. This is likely due to a physical change of the LNA due to external influences. When performing the same measurements with a different LNA from the same manufacturer, with serial number 1675z, we obtain a behavior similar to that observed in the 2022 measurements.

As it is known a priori that this behavior can be simulated as an impedance mismatched input port followed by a non-zero electrical path to the gain point of the LNA, we decided to use the amplifier 1675z (spare LNA) for the measurement campaign at CERN in 2023, instead of the amplifier 1598z that had been used in 2022.

The second difference observed during the calibration is related to the receiver used to measure and acquire the RF signal. In 2022, a custom-made receiver mounted at MPP

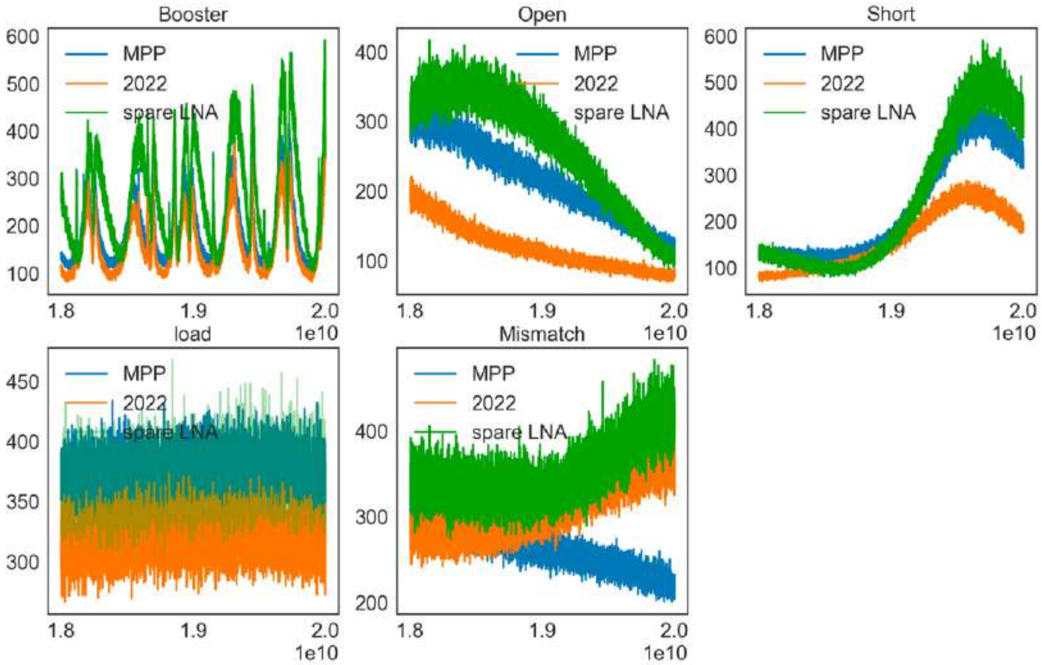

Figure 3.3: Measurements of the calibration standards and amplifier taken at CERN in 2022 (orange), taken at MPP in 2023 using the same LNA as in 2022 (MPP - blue), and taken with the spare LNA, later also used in the CERN 2023 measurements (spare LNA green). *main*, or simply *MPP* refers to the amplifier 1598z, used at CERN in 2022, while *spare* refers to the amplifier 1675z, used at CERN for 2023

was used. However, a non-linear behavior was observed when the data was being analyzed, which complicates the interpretation of the acquired data. Therefore, in 2023, we used the commercially available Keysight SA instead (see Table 3.1). The advantages of this system include it being convenient to transport with respect to the custom-made receiver, as all the receiver components are inside a box, whereas in the 2022 case, the receiver was made up of several oscilloscopes, amplifiers, mixers, cables, filters, and oscillators placed in two racks. Moreover, the SA has additional filters that contribute to reducing non-linearities as observed in 2022. The cost of using this SA as a receiver is mainly its deadtime as no data-streaming option was available. Whereas for the custom-made receiver the deadtime is less than 2 %, the SA deadtime is greater than 99 %.

For the 2024 measurement campaign in Morpurgo at CERN, it is planned to use another spectrum analyzer with an extension that allows the performance of the time-consuming Fast Fourier Transform (FFT)s in an Field Programmable Gate Array (FPGA) without stopping the data acquisition, thus approaching again the zero-deadtime scenario.

In order to cross-check the power calibration of the SA for both bandwidths (40 MHz and

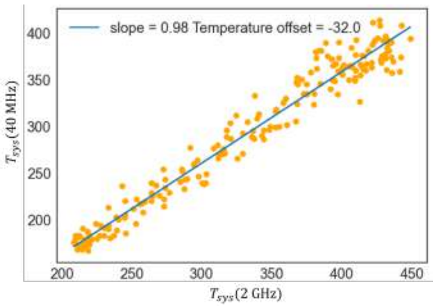

Figure 3.4: Correlation plot between two different registers. The 2 GHz one corresponds to the reference, while the 40 MHz register corresponds to the modified one.

2 GHz) a correlation scatter plot is shown in Fig. 3.4 can be used. Here, the obtained T_{sys} is plotted for the given frequencies once recorded with the 2 GHz and once taken with the 40 GHz bandwidths and SA settings. As can be seen, the high correlation found, given by the slope of the fit, ensures that the calibration measurements on both bandwidths are consistent. The offset comes from the fact that the bin width in the 2 GHz range is 1 MHz while for the 40 MHz range it is 1 kHz. This means that the frequency points sampled in both cases do not exactly match, producing an offset. The noisy nature of the measurement is shown in the dispersion of the correlation. As the integrated time increases, the dispersion decreases and the slope approaches 1, a longer integration time was not desired in this case because at the given precision it was clear that the calibrations were consistent.

3.1.2 Calibration at CERN

On March 2023 the full prototype setup was transported to the CERN North Area. It was re-mounted around the Morpurgo magnet, with CB-100 at the center of the warm bore, where the field is strongest. Care must be taken to position the taper and the booster in such a way that the TE_{11} mode is maximally coupled to the magnetic field for an axion-induced signal to occur [59].

Since the LNA can also change its behavior inside a magnetic field because the charges in the depletion region are sensitive to the Lorentz force exerted by the magnetic field, we also connected it in a direction such that this force is minimized. This had been tested in 2022, so the ideal orientation had not to be investigated again. Aside from these two remarks, we mounted the setup in the same way it had been done at MPP, using the exact same components. The full setup is displayed in Fig. 3.1.

The calibration steps outlined in Section 3.1 were again performed and compared to the results obtained in Munich. The fact that the noise calibration values were consistent with those found at MPP indicates that the transport of the setup did not cause any performance changes on the components, mainly in the geometry of CB-100. Moreover, it also suggests that the RFI in the North Area does not impact significantly the measurements.

After performing the full calibration outlined in Table 3.2, we connected the SA and the Data acquisition (DAQ) to a Uninterruptible power supply (UPS) to avoid power instabilities from reaching the components. We performed the measurements in the 40 MHz bandwidth around the booster dip and acquired automatically using a LabVIEW program, while the 2 GHz measured were acquired directly with the SA in local mode.

3.1.3 Data acquisition code for measurement campaigns

A LabVIEW program was set up by the MPP team. This code can acquire data by communicating with the SA through an Ethernet connection. On each loop, the program waits for the SA to average 400 sweeps and transfers it to the DAQ code. Six loops are averaged and written into one file that is sent to the local machine. One sweep corresponds to ~ 0.1 s integrated lifetime, so each file written to disc contains 400 × 4 sweeps averaged into a single value per frequency bin of uncalibrated power.

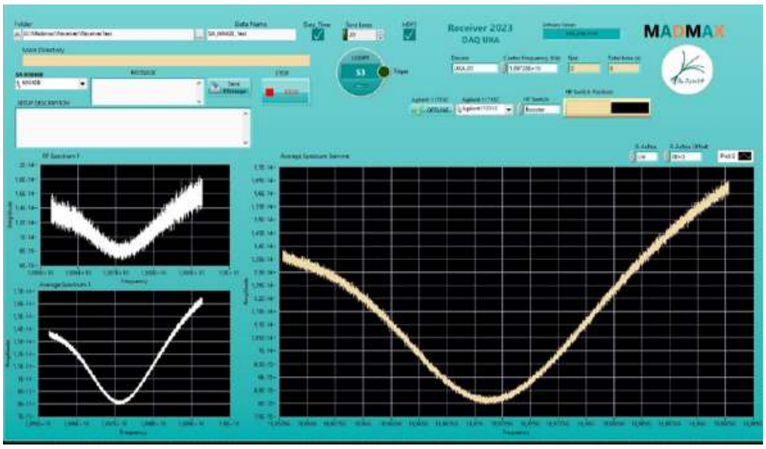

Figure 3.5: Interactive interface of the DAQ code used to record the data during the measurement campaigns in 2022 and 2023.

There is a user-defined time used to force a new acquisition (i.e., start again with six loops that average incoming files) in case a miscommunication between the computer and the SA freezes. Fig. 3.5 shows the interactive interface of the DAQ code to modify the user-defined parameters and visualize the last sweep read by the program.

The DAQ code stores new datafiles with a date-time timestamp in an ASCII file with no header, in contrast with the manual 2 GHz calibration measurements which are saved in ASCII formatted files with a header describing all the relevant settings from the SA. In both cases, two columns are stored, the first one with the frequency values and the second one with the uncalibrated power per bin measured. For 2023, the code wrote to disk a new *.smp* file containing the average of 2400 sweeps from the SA roughly every 12 minutes.

3.2 The MADMAX monitoring system

An important part of the work performed in the frame of this thesis is the Python script MADMON, the first monitoring system for MADMAX. The code collects data relevant for evaluating the stability of data taking. Most notably, it uses the CB-100 data taken, checks for its stability, and determines the level of the noise fluctuations of the last dataset as well as for the integrated data, updating every time a new file with the uncalibrated measured power is written to disk by the DAQ code, as explained in Section 3.1. This allows for the determination of the lifetime τ. A crucial parameter for determining the sensitivity of the ALP search is shown in Eq. (1.2). The MADmax MONitoring system (MADMON) code was first used in the measurement campaign at CERN in spring 2023 and will continue to be used in the next campaigns. The code is open and can be found in the main repository for this thesis (link in PDF version). In this section, the logic behind the script is explained block by block, along with the different parameters monitored.

3.2.1 Monitoring plot

The monitoring code outputs and updates a set of plots each time a new file is acquired. This set of plots can then be visually inspected by the operator to make sure that all parameters are according to expectations. As an example, in Fig. 3.6 the monitoring plot at the end of the 2023 data-taking campaign is shown.

The image features three rows of plots. These plots are referred to in the text as *plot X* with X from 1 to 9 in increasing order from top to bottom and left to right. The way to obtain all the quantities shown on the plot is explained in the present section. All the quantities are plotted and stored as data sets and saved as in ASCII format files on the DAQ machine.

As explained in Section 3.1.3, the average files are computed since the DAQ code is initialized. However, if the program is interrupted, for example, because an intermediate calibration is desired, the new average files will not consider the previous ones taken. This is problematic to compute the lifetime of the experiment, as well as to check the data quality across the full measurement campaign. Therefore, MADMON has a built-in function to calculate the running average considering the full set of raw data files. Finally, it outputs as a *csv* file a final averaged set ready to be analyzed. In the updating image shown in Fig. 3.6, the plots that refer to the *avg* files are not reading the ones provided by the DAQ code, instead, they read the running average that is computed by MADMON as follows:

Let N be the N-th raw file acquired. Then, the *last avg* file at time $t(N)$ can be computed as shown in Eq. (3.1).

$$\mathrm{avg}[t(N)] = \frac{\mathrm{raw}[t(N)]}{N} + \frac{N-1}{N}\mathrm{avg}[t(N-1)] \tag{3.1}$$

In this way, the monitoring system does not depend on whether the DAQ code crashes or is deliberately interrupted. More information on parameters, libraries, and functions developed in

MADMON are available in Appendix A.

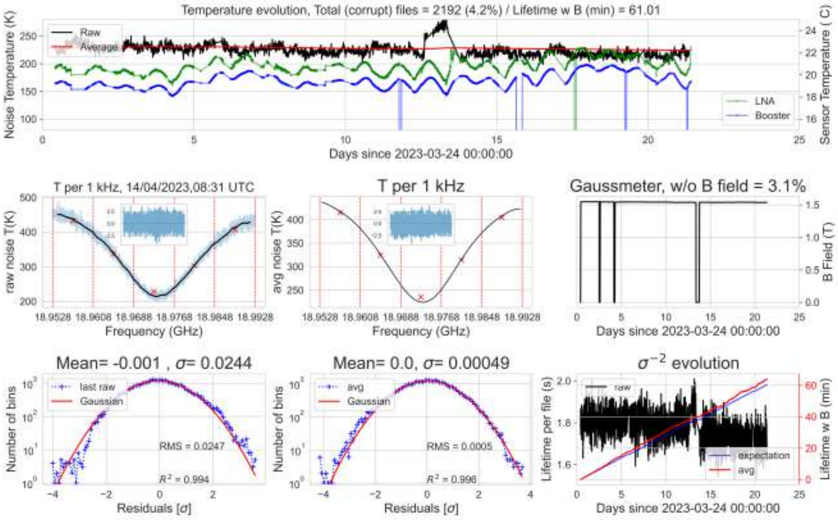

Figure 3.6: Final plot created by MADMON for the 2023 run at CERN. The different plots allow for visual inspection of relevant quantities such as lifetime, noise gaussianity, frequency-dependent gain changes, and receiver chain linearity.

System and physical temperature evolution

In the header, the information about total and corrupt[1] files can be found. Moreover, also contained in the header, is the total lifetime when the magnetic field was on, which is the τ parameter that should be inserted in Eq. (1.2) to extract a dark matter limit. This is computed using the radiometer equation introduced in Section 2.5. For 2023, the total integration time was over 1 hour.

In this plot, there are two y-axes corresponding to the equivalent noise temperature of the CB-100 setup in Kelvin on the left and physical temperature on the right in degrees Celsius measured on the LNA and on the top of the CB-100 metallic enclosure. The x-axis is shared and corresponds to a continuous evolution of time, denoting $t = 0$ the time at which the data taking started after the first calibration.

Regarding the equivalent noise temperature axis, two curves are plotted in black and red, for the last raw and last *avg* files acquired, respectively. Both are computed in the same way: First, a region of some kHz (in this case, 16 kHz) around the center of the booster dip is selected.

---

[1] A file that was stored by the DAQ code with invalid entries either in frequency, power, or both. This happens due to sudden glitches in the communication between SA and PC.

After calibrating the file's noise temperature, the average in this frequency range is computed and plotted as a function of time.

The objective of these plots is to monitor the stability of the calibration. The black curve should fluctuate around the CB-100 mean equivalent temperature $\sim 230\,\mathrm{K}$), while the red one should converge to this temperature rapidly, as the contributions from new files are weighted by a factor N^{-1}, as explained in Eq. (3.1).

As can be seen in the black curve around day 13, the booster baseline increased suddenly by 30 K and continued to increase up to 80 K from the baseline value. This happened during a time when the MADMAX team had no access to the hardware, due to an intervention of the CERN maintenance team in the North Area. Since this happened in the raw files, it indicates a change in the hardware. It was decided to stop the data-taking and re-calibrate the system as soon as access was granted again. As shown, the curve recovered its regular values after the intervention.

On the other hand, the green and blue curves correspond to the physical temperature reading from two Platinum resistance Thermometer (PT)-100 sensors connected to the LNA housing and CB-100. The objective of this plot is to possibly correlate noise temperature fluctuations with physical temperature ones. Since the booster geometry determines the resonance frequency, temperature fluctuations in CB-100 could cause thermal shrinkage or expansion that could shift the temperature and/or the magnitude of the booster dip. Moreover, the gain of an amplifier is also temperature-dependent. Additionally, the power settings used to bias it could unintentionally fluctuate.

There were some crashes in the Temperature sensors DAQ software that caused $\sim 30\,\%$ of the total running time to be left without temperature information. These crashes were caused by miscommunication between the hardware and the computer. The software had to be manually restarted by the operator, as shown in Fig. 3.7, where the lack of data is represented with smooth curves without markers. Another type of crash caused some unphysical temperature readings of $-241\,^{\circ}\mathrm{C}$, as also evidenced in Fig. 3.7.

For future runs, care must be taken not to use many interconnections between the Local Area Network (LAN) switch that connects to the different temperature sensors and the DAQ machine. in 2023, due to the physical distance between both, several cables were used. However, it was later tested at MPP that using only one General Purpose Interface Bus (GPIB)-to-Universal Serial Bus (USB) cable ensured the stability of the software across multiple days without any crash of the temperature sensors readout.

Although some physical temperature data is missing, correlation studies suggest that the equivalent noise temperature fluctuations induced by room temperature variations are negligible for this setup. However, as will be shown in Chapter 4, this may no longer be the case for the cryogenic setup.

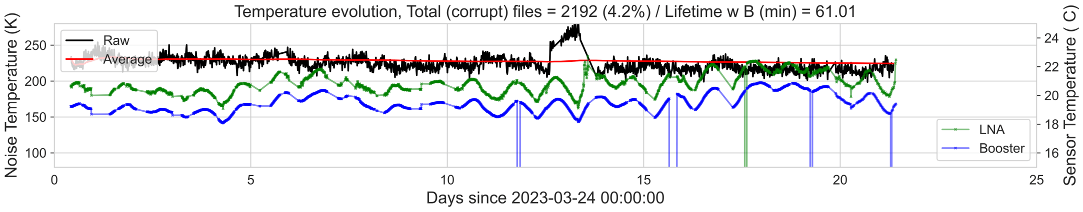

Figure 3.7: Equivalent noise temperature of CB-100 and booster dip for last raw and average file as well as physical temperature of LNA and CB-100.

Power Spectra and Savitzky-Golay filtering

Fig. 3.8 contains the plot for the *last raw* file and the *last avg* file. The last raw plot also shows the date and time when the file was recorded in Universal Time Coordinated (UTC). The Y-axis represents again noise temperature and the X-axis corresponds to the 40 MHz range around the booster dip. In light blue, the acquired power is shown as obtained by the power factor calibration. There are 6 dashed red vertical lines delimiting five 8 MHz frequency ranges. At the center (of the X-axis per width) there is a red cross denoting the average noise temperature of that particular range.

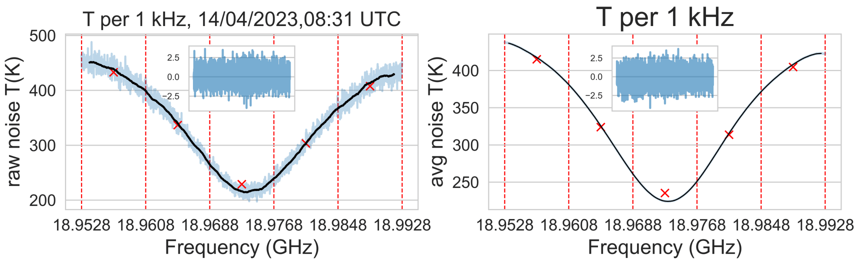

Figure 3.8: Measured power as a function of frequency in the 40 MHz for the last raw and average files. In black, is the computed Savitzky-Golay filter. In the inset, the filtered data is shown normalized to its standard deviation.

As new data files are analyzed, the averaged temperature-calibrated values of the five crosses are stored in a *csv* file that can be studied independently. This allows us to search whether there have been frequency-dependent gain fluctuations in the spectrum, which could signal instabilities in the system temperature T_{sys} distorting the expected noise shape. If the receiver works as expected, T_{sys} should be stable in time.

On the same plots, the black curve corresponds to the Savitzky-Golay filter P_{fit} applied to the calibrated power P. This curve should show the same shape as the "unfiltered" data. The inset of the plots shows the residuals P_{res} obtained by Eq. (3.2). Normalizing the measured power P by the Savitzky-Golay filter P_{fit} removes the frequency dependence of the variance σ.

This is explained below.

$$P^{\text{res}} = -1 + \frac{P}{P_{\text{fit}}}. \tag{3.2}$$

This process is a so-called *background subtraction* but care must be taken since that name is misguiding. Here, to reduce the *background* (i.e., the booster shape without axion present), a division is preferred instead of subtraction, as the noise Root Mean Square (RMS) is frequency-dependent. This is because for the SA to measure the 40 MHz range, it has to apply band-pass filters to ignore the frequencies outside the desired band. Since band-pass filters have a smooth rising edge, they are less effective near the edges of the filtered band and close to ideal near the center. This causes noise filtering near the center to be more effective, thus reducing the RMS, while noise near the edges appears to be larger.

Assuming that the fluctuations around the booster dip shape are white noise (an assumption that is crucial and checked in several ways throughout the monitoring code), then, as explained in Section 2.4, the frequency-dependent standard deviation $\sigma(\nu)$ should be proportional to the average in the vicinity of a data point $\overline{P}(\nu)$. Then, let $\left(\overline{P_1}, \sigma_1\right)$ be the RMS and mean power of a point near the edges of the spectrum, for example, in the first width delimited by the vertical red crosses. Then, let $\left(\overline{P_2}, \sigma_2\right)$ refer to another point close to the booster dip, for example in the third width. Let P_{fit} be the Savitzky-Golay curve that is used to remove the shape of the booster noise. By subtracting it one gets a new data set where points 1 and 2 have been replaced with σ_1 and σ_2 respectively, assuming the filter is ideal and only removes the overall shape without modifying the high-frequency features. Because $\overline{P_1} > \overline{P_2}$, then $\sigma_1 > \sigma_2$, which means that the residuals are not a *stationary* process, in the sense that the variance is not the same across all frequencies, complicating the statistical analysis.

Now, note what happens when P_{fit} is used to normalize instead of subtract, then the points are transformed as

$$\begin{aligned} P_1^{\text{res}} &= \frac{\overline{P_1} \pm \sigma_1}{P_{\text{fit}}(\nu_1)}, \\ P_2^{\text{res}} &= \frac{\overline{P_2} \pm \sigma_2}{P_{\text{fit}}(\nu_2)} \end{aligned}$$

which, assuming again an ideal filter, can be simplified to

$$\begin{aligned} P_1^{\text{res}} &= 1 + \frac{\pm\sigma_1}{P_{\text{fit}}(\nu_1)}, \\ P_2^{\text{res}} &= 1 + \frac{\pm\sigma_2}{P_{\text{fit}}(\nu_2)} \end{aligned}$$

Finally, because the expected noise is white (i.e., Gaussian), then $\sigma_i \propto \overline{P_i} \approx P_{\text{fit}}(\nu_i)$. Therefore, $-1 + P_1^{\text{res}} \approx 1 + P_2^{\text{res}}$. which means that the residuals calculated as proposed in

Eq. (3.2) can be described as stationary: the standard deviation is not x-axis dependent.

The Y-axis of the inset is normalized by the standard deviation of the residuals calculated in the 40 MHz range, so it can be seen that most of the points are within 2.5σ around the mean. More about this is discussed in Fig. 3.10. A hypothetical axion signal would appear as an upward fluctuation in this plot if the noise is low enough to uncover this power excess.

Magnetic field evolution

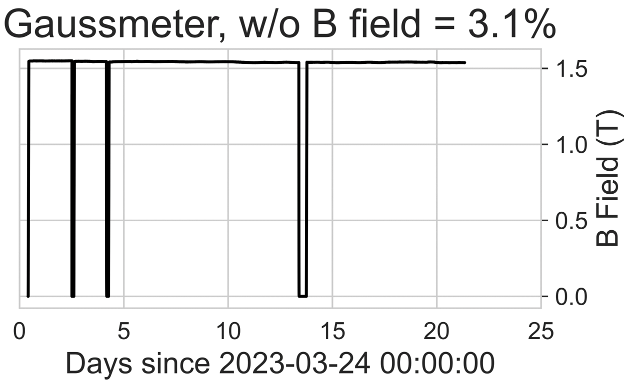

Figure 3.9: Magnetic field evolution measured by a gaussmeter on top of CB-100.

Fig. 3.9 shows the magnetic field strength measured by the Gaussmeter Lake Shore LM475 [60] placed on top of CB-100. On the header, the fraction of time, since the DAQ started without the Magnetic (B) field on, is shown. The Morpurgo magnet exhibited remarkable stability. For 2023, there are only 4 times where the B field decreased from its nominal value, clearly seen by the spikes on the plot. Below a description of each ramp-down is provided:

- $\boldsymbol{t = 0}$: Initial ramp-up of the magnet. The purpose was to measure the time needed to reach the nominal value. The measured value for the ramp-up speed was 37 mT min^{-1}.
- $\boldsymbol{t = 3}$ **days**: Unplanned ramp-down of the magnet due to sudden power shutdown in the CERN North Area caused by an electric storm. The on-site shifter team ramped up the magnet after 3 hours.
- $\boldsymbol{t = 4}$ **days**: Planned electrical intervention by the CERN staff as some non-MADMAX related tests of the area had to be performed. Duration of 3 hours
- $\boldsymbol{t = 13}$**days**: Planned intermediate calibration that was needed as explained in Section 3.2.1, due to the sudden increase in noise temperature around the booster dip seen in Fig. 3.7. Duration of 9 hours.

We were able to minimize the dead time caused by the unplanned ramp-down of the magnet thanks to the alarm system incorporated in MADMON explained in Appendix A, and the quick response of the operators on-site.

White noise distribution of fluctuations

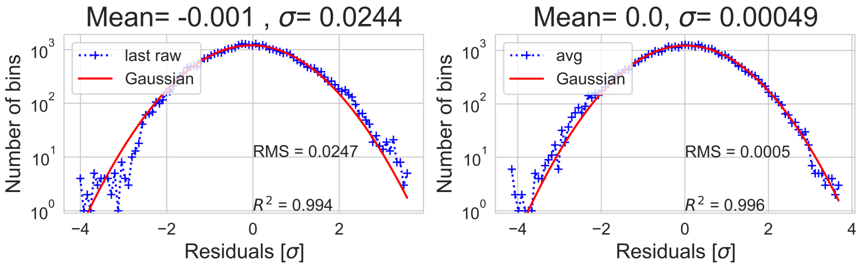

Figure 3.10: Distribution of fluctuations around the booster dip shape normalized to the standard deviation, along with the expected histogram for white noise behavior.

These plots show the distribution of residuals in units of the standard deviation σ as derived from the residuals obtained and shown in Section 3.2.1. Fig. 3.10 contains the histogram from the *last raw* file (left) and from the *last avg* (right). To obtain these histograms, the residuals plot shown as an inset in Fig. 3.8 are projected onto the Y-axis. The X-axis of the histogram is normalized to the standard deviation of the residuals dataset, which makes it more direct to see whether there is an unexpected number of counts. The red curve is a Gaussian fit to the histogram expected for white noise behavior, with mean and variance as free parameters. The optimal parameters are displayed in the header of the plots. The mean and standard deviation computed for the dataset (that is, without assuming any particular distribution) are also displayed. Also, the value of the R^2 of the fit shows a criterion used for constant-variance datasets to judge whether a fit describes the dataset, $R^2 = 0$ meaning that no data points are described by the obtained fit, while $R^2 = 1$ indicates perfect agreement between both.

To estimate whether the number of counts above 4σ is consistent with the white noise picture, a simple calculation can be made: in the 40 MHz range, the RBW is set to 1 kHz due to the expected axion-induced signal. This means that there are 40.000 points in the histogram. If the noise registered is Gaussian, then the probability of finding data points above 4σ is

$$1 - P(\mu - 4\sigma \leq X \leq \mu + 4\sigma) \approx 0.0063\,\%,$$

where $\mu = 0$ is the mean of the distribution and X is the random variable. For a set of 40.000 points, it is expected that around $0.0063\% \times 40.000 \approx 3$ are found above 4σ. For the raw data files, it is usually found that there are 1 to 5 points depending on the file, while for the last average after the complete run, exactly 3 points were found above this level.

We noted that these tests, which are common practice in different experiments [19, 26], are not sensitive to subtle non-gaussianities that were observed in the data acquired in 2023. New proposals inspired by the *SQUARES* statistics method [61] have been shown to be more sensitive to these effects and are therefore proposed to be added to MADMON in the future.

Lifetime calculation

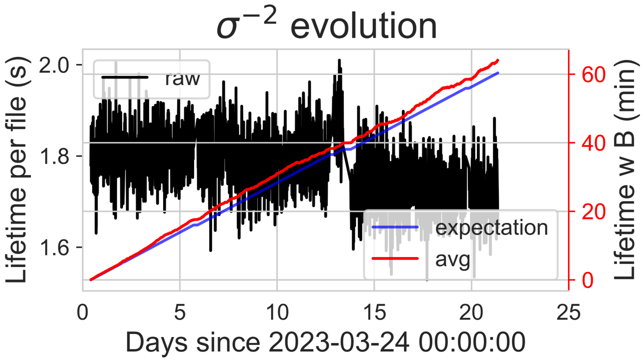

Figure 3.11: Inverse variance for the raw and average files as a function of time, together with the expected evolution for white noise being integrated over time.

Fig. 3.11 shows the lifetime of the raw data files and the integrated lifetime of all files averaged as a function of time, which provides a measure of the integration time of a signal when the noise is white (see Section 2.5). On the first Y-axis, on the left, the integration time per raw file is shown. These lifetimes are around 1.8 s. It is possible to calculate the deadtime of the DAQ system as follows: A new raw file is stored every ~ 12 min and represents an integration time of ~ 1.8 s. Therefore, the deadtime is around

$$100 \times \frac{1.8}{12 \times 60} \approx 99.7\,\%.$$

The second Y-axis on the right shows in red the lifetime of the *last avg* file as a function of time, ignoring the files where there was no B field, and the theoretical expectation from Eq. (2.12) in blue, assuming the noise acquired is white and taking the first point y_0 as the RMS of the first raw data file acquired. It can be seen that both curves are slowly drifting apart. The fact that the experiment appears to have a higher lifetime than the theoretical expectation might be an artifact of the initial condition y_0.

For the future, it is planned to replace SA with a dead-time-free spectrum analyzer suggested by the Max Planck Institute for Radio Astronomy.

CHAPTER 4

Towards a cold calibration and operation of CB-100

In Section 1.2.2, the main challenges of a cryogenic calibration and operation of CB-100 were introduced. In this chapter, the single thermal cycle calibration setup that we propose is described. The measurements needed to ensure a stable and reliable setup with reproducible results are discussed. We also show which measurements were performed to estimate the systematic uncertainties induced by the setup. They are compared to the case at room temperature.

4.1 Proposed cryogenic setup

Up to now, the MADMAX prototype CB-100 is calibrated at room temperature by performing different measurements and manually changing the setup as described in Section 3.1. However, once the setup is placed in a cryogenic environment, minimizing the number of steps and manual tampering of the setup is crucial, as explained in Section 1.2.2.

The calibration measurements needed are listed in Table 4.1. Note that all these measurements are already performed manually at room temperature, as explained in Table 3.2 and Section 2.7. As in the room temperature case, all the listed measurements need to be done twice, once in the frequency range 18 to 20 GHz, and once in the 40 MHz around the booster dip.

We propose the scheme shown in Fig. 4.1 as a way to obtain a single thermal cycle setup for calibration and operation of CB-100. The idea is that after characterizing the individual components at room temperature and cryogenic temperature and mounting the completely characterized setup inside the cryostat, no manipulation is needed to obtain all the 12 calibration measurements for ALP searches, thus reducing the total calibration time from several weeks to some hours, while increasing at the same time the stability and reproducibility of the experiment.

The setup components are as follows:

Measurement	**Instrument**	**Purpose**	**SP2T port**	**SP6T port**
LNA off	SA	Spectrum analyzer baseline noise	1	-
LNA with terminated attenuator	SA	Correlation between noise voltage and current in LNA noise model	1	3
LNA with open	SA	Noise current in the LNA noise model	1	5
LNA with short	SA	Noise voltage in the LNA noise model	1	6
LNA with mismatch	SA	Cross-check measurement for the LNA noise model	1	4
LNA with heated attenuator	SA	Warm load for power calibration	1	3
LNA with terminated attenuator	SA	Cold load for power calibration	1	3
LNA with CB-100	SA	Geometry, booster frequency, and DAQ run	1	1
Calibration standards (SOLM[a])	VNA	1-port calibration to move reference plane	2	3 to 6
CB1-100	VNA	Group delay for booster characterization	2	1

Table 4.1: Calibration measurements required for a full calibration at cryogenic temperature.

---

[a] short, open, load, and mismatch

- **SA**: Spectrum analyzer to be used for noise calibrations, as well as the receiver for the data-taking in the data-taking runs.
- **VNA**: Used for the *reflectivity calibration* of the system
- **Single port double throw switch (SP2T)**: used at room temperature to switch between the SA and the VNA without manipulating any of the cables. We are using a Radiall SP2T switch of reference R570f32000 [62].
- **LNA**: Used to amplify the incoming signal from the booster above the internal noise level of the SA. We are using the reference LNF_LNC6_20C [56].

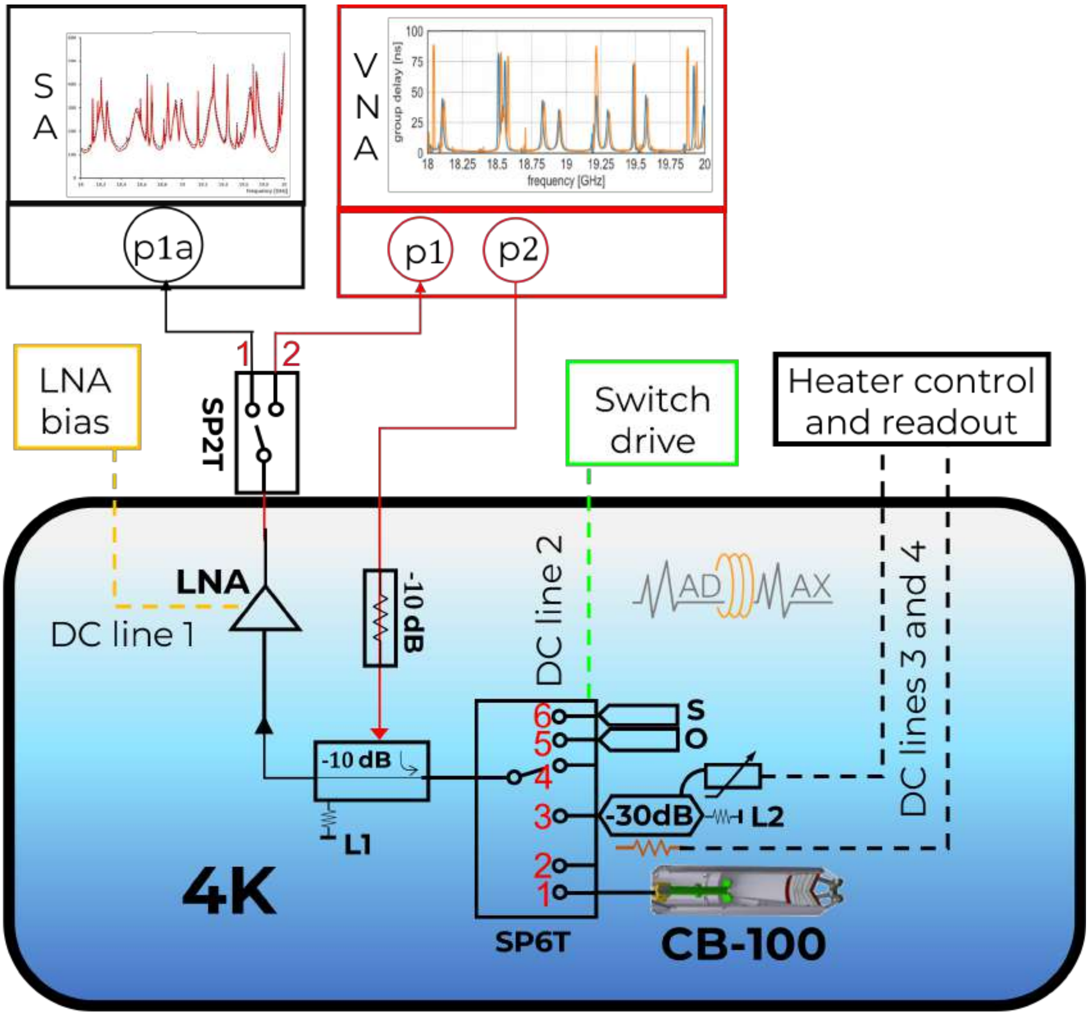

Figure 4.1: Setup idea for a single thermal cycle calibration and operation of CB-100 at cryogenic temperatures.

- **attenuator**: A 10 dB attenuator is placed to reduce the thermal noise leaking into the cryostat through the RF cables connected to the VNA. This component would not be needed if the coupling provided by the directional coupler were 20 dB instead of 10 dB.

- **Directional coupler**: The directional coupler provides a way to receive the incoming power from CB-100 in the SA as well as to perform reflectivity measurements by sending a signal from the VNA for calibration purposes. We are currently using the Marki CE10-1R540 [63]. The coupler is match-terminated on one of the four ports as only three are needed for measurements.

- **Single port six throws switch (SP6T)**: We are using the Radiall R591722600 [64]. It allows to switch from the outside and collects the measurements from the devices connected to the right, which correspond to the calibration standards and CB-100. It is connected to an external switch drive by DC lines from the cryostat feedthrough to the switch. Usually, the center port, called a *pole* can be connected to either of the six outer ports, called *ports* by latching the switch into the desired position. The *ports* are always isolated from one another.

- **S,O,L1,L2**: These corresponds to the *Open*, *Short*, and *load* calibration standards used for calibration purposes. We use Rosenberger standards with references 22300, 02b70, and 01b50 respectively (S-parameters shown in Fig. 4.5). Additionally, a 30 dB attenuator from microwave circuits is connected to the load to ensure high signal absorption at low temperatures.

- **heater**: A heater is placed near the load, along with a temperature sensor, to be able to provide different temperatures and perform the power calibration explained in Section 2.4.

With the SP2T switched into the VNA position, the reflectivity calibration can proceed as follows:

First, the reflectivity S_{11} is measured for the different calibration standards (open, short, attenuated load, and optionally a mismatch) placed on the ports of SP6T. To do this, a VNA signal is sent through the second port of the VNA (*VNAp2*) and received on the first port (*VNAp1*) after amplifying the signal by the LNA. Ideally, when solving the 1-port calibration model with these measurements, the systematic effects produced by the path traversed by the waves (including the effect of attenuators, couplers, amplifiers, and temperature gradients) will be corrected for [55].

To explain the necessity of this apparently cumbersome way to define S_{11} let us imagine what would happen if a conventional measurement was attempted. Usually, to measure S_{11}, the signal is sent and received with the same VNA port. If this is done with *VNAp2*, the signal sent would be attenuated by 20 dB from the attenuator and the coupling of the directional coupler. Therefore, only 1 % of the original signal would arrive at the DUT. This in principle is not a problem. On the contrary, it is intended this way, as the thermal noise coming through the cable will also be attenuated in the same amount. Considering that this noise is generated by a room temperature of ~ 300 K, 1 % of that amount would correspond to thermal noise coming from a body at ~ 3 K, which is in the same order of the temperature of the DUT is inside the cryostat. However, once the reflection travels back outside the cryostat, it will again be attenuated by the same path (as the coupler and attenuator are reciprocal devices). Therefore, only 0.01 % of the original signal would get back to the VNA, a proportion potentially insufficient for reliable analysis.

If, on the contrary, the *VNAp1* is used to send and receive the signal, the problem arises by the fact that amplifiers are *one-way* (i.e., non-reciprocal) devices, which amplify the signal from input to output and acts like an open-circuit from output to input. Therefore, no signal would reach the switch. In our case, we measured the transmission coefficient from output to input to be below 50 dB, which on the other hand is useful to provide an isolation from the thermal noise at 300 K. The use of a LNA cannot be avoided because the thermal noise of CB-100 (and a potential ALP signal) are below the internal noise from the SA, so a second path for the VNA input signal must be provided.

The approach of using both ports of the VNA to perform a measurement of S_{11} has also been used by other authors mainly in quantum computing applications at lower frequencies [36, 65, 66]. In principle, the only difference at higher frequencies is the higher precision required.

By using this setup and de-embedding the internal length of each switch port we obtain a set of three independent reflectivity measurements that can be used to perform a 1-port calibration [53], moving the reference plane to the switch. After the one port calibration has moved the reference plane, CB-100 can be measured and the booster peak frequency can be obtained by studying the group delay of the reflected S_{11} signal. Care must be taken to de-embed the path used for the reflected signal. The LNA and coupler S-parameters need to be known beforehand.

On the other hand, When the SP2T is switched to the SA connection, the noise calibration can be performed. First, the short, open, and attenuator standards are measured to obtain the relevant files for the noise model of the LNA (Section 2.3). Then, the load is heated up and new noise measurements are acquired. This provides the calibration files needed to perform a power calibration as explained in Section 2.4. Next, CB-100 is measured. This is done for both the 2 GHz and the 40 MHz SA setups. Finally, the switch is left unchanged in the CB-100 position and the 40 MHz setup, and the data-taking run can begin.

To test whether this idea can be implemented with enough stability and to ensure a high reproducibility of our results, different measurements need to be performed. These are described and discussed in Section 4.2.

4.2 Characterization of setup components

4.2.1 Reproducibility and stability

To determine the stability and reproducibility of the CB-100 cryogenic setup, we took a bottom-up approach, where we start by determining the stability of the VNA itself, the first building block for our setup- and then increase the complexity by adding more components. The underlying assumption to follow this strategy is that there are no emerging phenomena when treating incoming and outgoing waves. This is justified by the T-matrix formalism introduced in Section 2.1, which states that the transfer matrix of a system can be computed as the matrix multiplication of the T matrices of each component in the system. Moreover, this approach allows us to pinpoint the problematic components of the setup and permits the determination of the uncertainty of a reflectivity measurement. We estimate the setup to be stable enough if the phase stability $\Delta\Phi$ at 20 GHz is in the order of a few degrees, corresponding to systematic length uncertainties in the order of a few µm. These values are based on Montecarlo simulations for the boost factor as presented in Section 4.3. In the present section, the stability results of different RF components are discussed.

Vector Network Analyzer

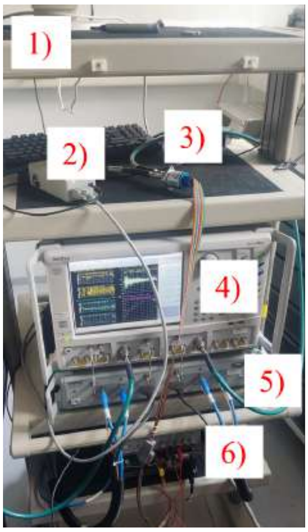

Figure 4.2: Example of a VNA measurement. 1): torque-wrench to reduce variability in connections, 2): Auto-calibration kit 36585K. 3): RF switch R591722600. 4: VNA MS4647B. 5): Rosenberger RF cables (green). 6: Switch drive Keithley 7001 and DC power supply.

The stability and reproducibility of the VNA itself depends on the reliability of the calibration used to minimize the systematic uncertainties [53, 55], which depend on the drift of internal components such as local oscillators, the ambient temperature at which the calibration was performed, hardware changes, for example of cable bending, and time elapsed since the VNA was turned on. Additional uncertainties can show up if the frequency span modulus of the number of frequency points is not an integer, as the post-processing might induce rounding errors. Finally, higher precision is achieved on a measurement if the power sent by the VNA is high (for example, 0 dBm instead of −10 dBm). This is because weak signals have lower Signal to Noise ratio (SNR), and the VNA might not determine with high accuracy the S parameters, an example of this is the typical noise seen in S_{11} when measuring a load standard. However, care must be taken not to overload the VNA power receiver, especially when dealing with active components like amplifiers, that could enhance the sent signal to levels above the indicated range by the VNA datasheet (for the Anritsu MS4647B, the maximum power is 27 dBm). An example of a measurement at room temperature with the VNA is shown in Fig. 4.2. To obtain the *baseline* stability, i.e., the best achievable stability and reproducibility of a measurement, the following VNA configuration is used:

- **Frequency**: All the measurements were performed in the range of 18 to 20 GHz, which matches the frequency range used for the 2 GHz calibration with the spectrum analyzer Chapter 4. A total of 2001 points are selected (the last one is not included) as a compromise between reducing the interpolation-induced error while saving on disk space and measuring time.

- **Power**: Set to 0 dB to gain more sensitivity in the low-signal regions. This value is within the specifications of the VNA for all the components that are foreseen to be tested except for the amplifier, as its gain is around 30 dB at room temperature, while the VNA safety limits indicate an upper limit of 27 dBm.
- **Calibration**: 2-port calibration with true through [67] using an adapter previously characterized, or the internal through provided by the autocalibration kit 36585K from Anritsu.
- **Cables**: The stability with different sets of cables were tested, including phase stable (PS) cables without significant improvement. This is probably because the improvements provided by phase stable cables come mostly in the higher-frequency regime. Therefore, the cables used for all the reflectivity measurements at room temperature were the Rosenberger LU8-101-1500. In the cryogenic tests, these cables are also used between the VNA and the cryostat feedthroughs.
- **cable positioning**: roughly in the same position as when the calibration was performed, we use cable ties and tape to ensure this positioning, without exerting too much pressure as the cross-section of the cable would change.

After performing the 2-port automatic calibration, each VNA port is closed with a short or an open calibration standard, thus maximizing the reflection. Repeated measurements of S_{11} and S_{22} are performed over time to study the stability of the device. Results for the variation of S_{11} and S_{22} with respect to the first measurement after calibration are shown in Fig. 4.3.

Because this measurement is subject to daytime temperature changes, the temperature of the room was monitored during the 24-hour period. We concluded that the stability of the magnitude measurements is below 0.03 dB °C^{-1} (or $\lesssim$ 0.9 dB in a period where temperature fluctuated in the range of 21 to 24 °C), which is in agreement with the VNA datasheet [52] when the measurements are performed after a full calibration within the safety temperature range for operation.

Moreover, we also studied the phase stability which is crucial for determining the electrical path lengths that the signals will travel in the setup. The result is shown in Fig. 4.4.

It can be seen that the maximum variation was measured on the second VNA port, corresponding to a 0.9° drift in a 24 h period and a standard deviation between measurements of 0.3°. Although the VNA datasheet specified slightly different values (0.1° in systematic uncertainty for measurements taken at the same temperature within 1 °C), the temperature fluctuations of the laboratory could have affected the test, especially considering that it spanned a full day, and the corresponding temperature variations. Although more frequent calibrations could reduce this factor, the stability found is already high enough for all our purposes.

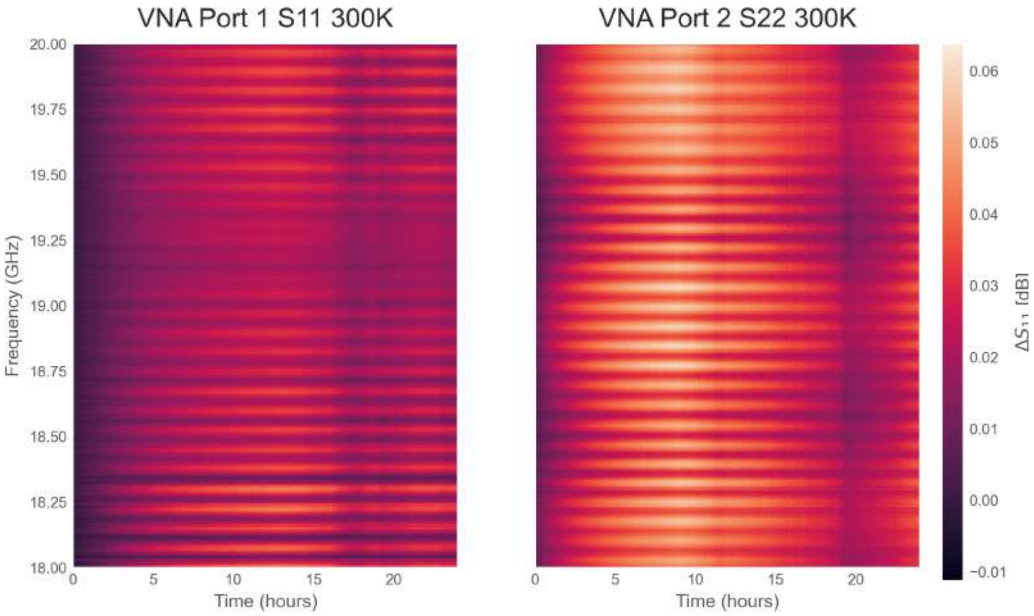

Figure 4.3: Magnitude stability measurements for the VNA after a full calibration during a 24 hour period.

Calibration standards

At room temperature, the calibration standards used throughout this project are from Rosenberger and have the following references:

- Open standards: 22300 and 02b13 with internal length of 25.02 ps reported by Rosenberger calibration certificate.
- Short standard: 02b70 and 02b68 with internal length of 28.35 ps reported by Rosenberger calibration certificate.
- Load standards: 01b50 and 01b80 with $S_{11} < 30$ dB between 18 to 20 GHz (both reported by Rosenberger and measured with the VNA).
- Mismatch: 46A24. However, as it is common for these devices, the phase is not specified, only the magnitude of the impedance mismatch with respect to 50 Ω, in this case, $S_{11} \approx 0.2$.

The standards 01b50,02b70, and 22300 were used for the amplifier noise model calibration at room temperature, as described in Section 2.3. To avoid jeopardizing their already well-characterized frequency response, they were not used at cryogenic temperatures, as they are

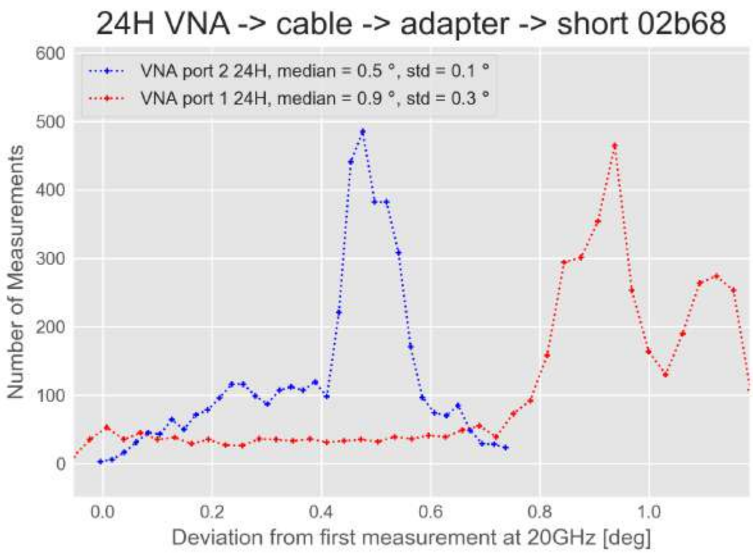

Figure 4.4: Phase stability measurements for the VNA after a full calibration during a 24 hour period.

certified for operation in the range of 20 to 26 °C only. The reflectivity response of the standards at room temperature used for the reflectivity calibration is shown in Fig. 4.5.

To compute the actual S-parameters shown for the calibration standards, an adapter was de-embedded from the measurement by subtracting 61.7 ps, as the standards and the VNA cables were both male-connected, so a female-to-female adapter had to be used in-between. Note that the measured reflection coefficients are in the expected region on the Smith chart [38] but have an extension instead of being point-like objects. This is because of the internal length of the standards, which causes an additional time for the wave to come back to the VNA, developing more phase as the frequency increases. The only standards that matched the ideal expectation correspond to the load, because most of the signal is absorbed anyway, so the internal length does not cause any phase accumulation as there is practically no wave being reflected back.

At cryogenic temperatures, it is well known that the load standards can degrade considerably [36]. Therefore, instead of a Short-Open-Load (SOL) calibration [53], a terminated 30 dB attenuator can be used to mimic the load behavior. Attenuators can perform better across a large temperature range, so for our purposes, we preferred a Short-Open-Attenuator (SOA) one-port calibration at cold temperature, using a 30 dB attenuator, which has a comparable S_{11} response as the load used at room temperature.

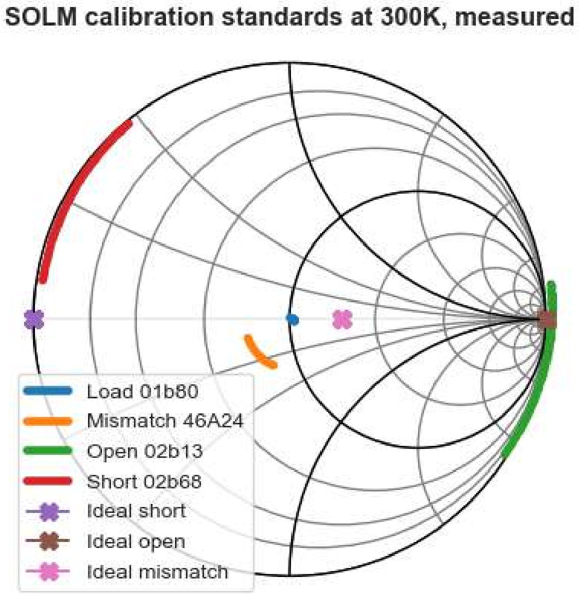

Figure 4.5: Smith chart (see Section 2.1.2) of the calibration standards used for the VNA measurements compared to the ideal values expected as obtained in the lab with the VNA. After de-embedding the internal length, the measurements convert to the expectations (tested but not shown here).

RF cables and cryostat

To compute the length of the cables plus the standard we measured S_{11} using the calibrated VNA the following relation was used:

$$L = (\Phi(\nu_f) - \Phi(\nu_i)) \times \frac{c}{(\nu_f - \nu_i) \times 360 \times 2\sqrt{\epsilon_r}}. \tag{4.1}$$

Here L is the length traveled by the signal in meters, $\nu_{f,i}$ are the initial and final frequencies from the frequency sweep, $\Phi(\nu)$ is the unwrapped phase (see Section 2.1.1) measured in degrees at the frequency ν, and ϵ_r is the relative permittivity of the media. This is derived by noting that when the wave travels a distance of one wavelength λ, it accumulates a phase of 360°, and that the wavelength depends on the group velocity, which is defined as proportional to the speed of light and inversely proportional to the square root of the dielectric constant. Finally, in an ideal propagation the unwrapped phase Φ should behave linearly as $\Phi = m\nu$ where m is the slope of the linear trend. The intercept should be zero because at 0 Hz no phase should be

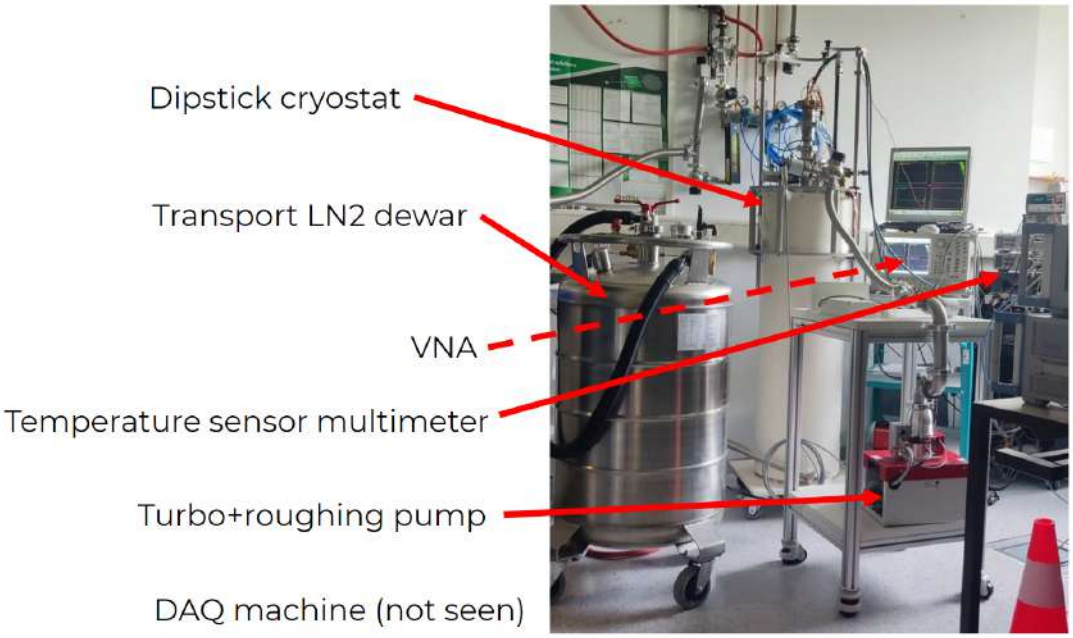

Figure 4.6: Setup used for the stability test in the dipstick cryostat. Inside, there are two RF cables connecting to open and short standards, immersed in either Liquid nitrogen (LN2) or Liquid helium (LHe).

accumulated, therefore, the slope can be quantified as:

$$m = \frac{d\Phi}{d\nu} = \frac{\Phi(\nu_2) - \Phi(\nu_1)}{\nu_2 - \nu_1}.$$

For example, for the measurement in the LHe cryostat, we derive using Eq. (4.1) that the length traveled by the wave from the reference plane is of $L \approx 1.52\,\mathrm{m}$ assuming that the dielectric media is teflon ($\epsilon_{\mathrm{PTFE}} \approx 2.1$), which is in agreement with the physical measurement of the RF cable that connects the feedthtrough to the cold plate, reported to be of 1.5 m. A slightly larger value is obtained because the feedthrough and the standard lengths add an additional length.

We checked the loss and phase stability of the cables connecting from the VNA to the cold stage at cold temperature by connecting high-reflective calibration standards (open and short) at the end of the cables and measuring S_{11} repeatedly as a function of time with the remote acquisition code we developed and stored in Anritsu_MS4647B remote control (link available in pdf version). First, we used a setup with a dipstick cryostat, as shown in Fig. 4.6, which allowed for fast testing since it does not require cooldown of the cryostat from room temperature to LHe temperature for independent measurement cycles.

This measurement test was done twice, first with SMA flexible RF cryo-compatible cables

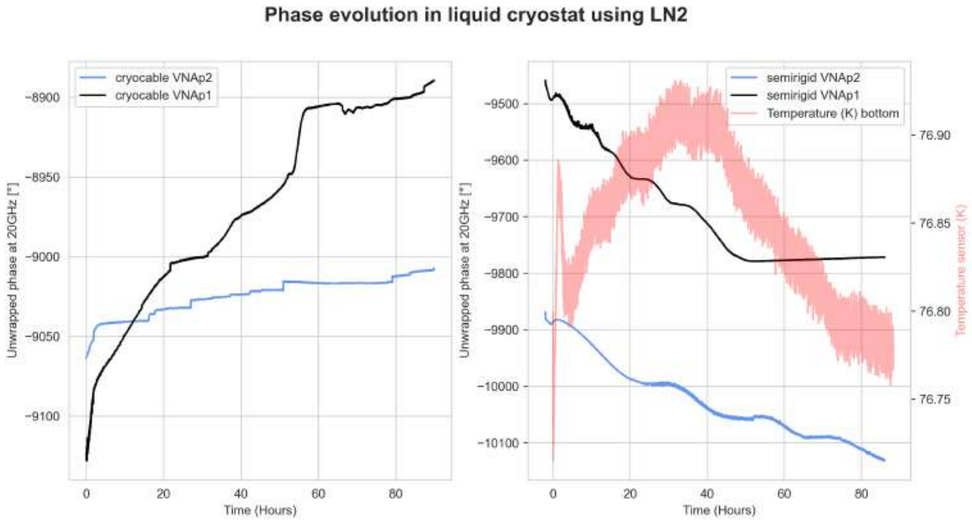

.

Figure 4.7: Phase stability study in the dipstick cryostat at LN2 temperature. On each run, two independent measurements were taken with both VNA ports. First, run with SMA cryo-compatible flexible cryo-cables from El-spec and second one with Rosenberger semi-rigid ones in the frequency range of 18 to 20 GHz

from El-spec (referred to as cryo-cables) and then with Rosenberger semirigid cables which should exhibit better phase stability. The temperature in the vicinity of the calibration standards was recorded to look for possible correlations between temperature and phase changes. The results are shown in Fig. 4.7.

We found that there is no stable region even after waiting for some hours for the components to thermalize. Also, there is not a strong correlation between the temperature at the DUT and the phase of the signal, and between runs, and even in the same run between both cables, there is not any predictable evolution of the phase at 20 GHz. The use of semi-rigid cables did not improve the stability either. Our hypothesis is that as the LN2 evaporates, the fraction of the RF cables that are immersed in the liquid changes continuously. This time-dependent thermal gradient causes not only physical length changes, but also changes in the lumped-element properties of the cables displayed in Eq. (2.1).

To increase the stability, we mounted a second setup using a cold plate cryostat, in which the RF cables and DUT are outside of the liquid and cooled by conduction from a cold copper plate which sits at the bottom of the LHe vessel. The conceptual difference between both approaches is sketched in Fig. 4.8. In this configuration, the thermal gradient on the components (cables, attenuators, etc.) is much more controlled, hence the phase stability should improve considerably.

Another important advantage of the cold plate cryostat is that the LNA can be operated in

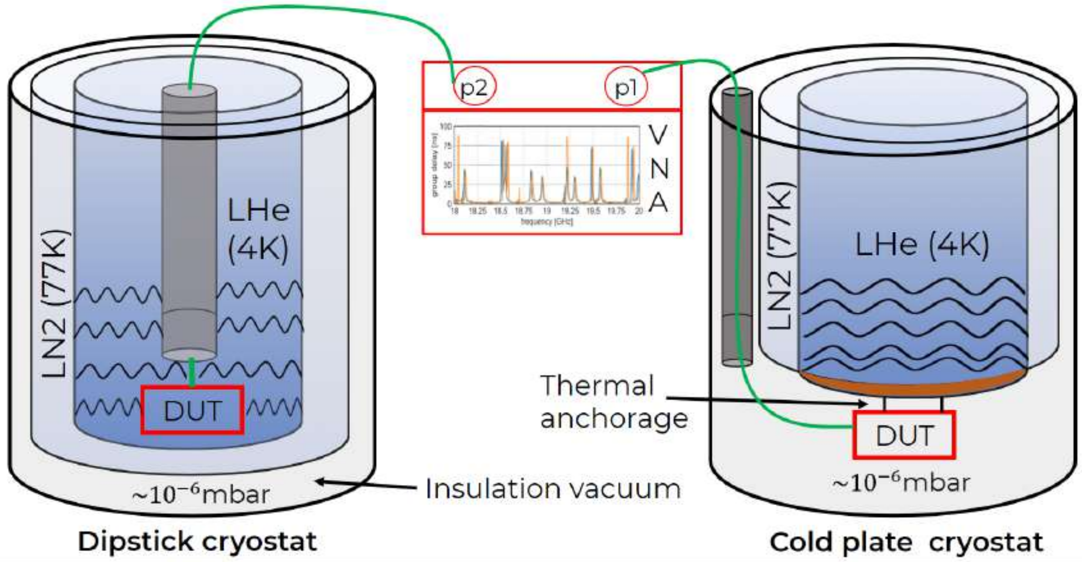

Figure 4.8: Sketch of the dipstick cryostat (left) and the cold plate cryostat (right). While the dipstick cryostat enables cooling the DUT by full immersion into the liquid, the cold plate one works by thermally anchoring the DUT to a highly thermal conductive plate sitting at the bottom of the liquid. The DUT in this case is inside an insulation vacuum.

the vacuum, as the housing is not rated for immersion in liquid helium. The new setup is shown in Fig. 4.9.

The disadvantage of this setup is the inconvenient positioning of the RF components in the copper plate, as it is done upside down, and especially the fact that each cooldown requires considerable time also if the DUT is changed, the cryostat needs to be opened.

The result of the phase stability test inside the cold plate cryostat is shown in Fig. 4.10. The system requires some hours to thermalize, which has the effect of decreasing phase as a function of time during cooldown. Some hours of data were lost due to an unplanned power shutdown in the laboratory. but thermalization is consistent with the measurements recorded again starting from the 22nd hour.

After that, for over 30 hours the phase only changed by $\sim \pm 1^\circ$ at 20 GHz, corresponding to $\sim 30\,\mu\mathrm{m}$ in Teflon, or 0.15 ps. This is a sufficient time span to perform the whole calibration plus a physics run. We also obtained longer stability periods by performing regular LHe refills before the liquid level drops below a couple of centimeters.

Compared to the baseline VNA stability shown in Fig. 4.3, it can be seen that the presence of this complex cryogenic setup degrades phase stability by roughly one order of magnitude. However, micrometer systematic uncertainties in the electrical length or picosecond systematic uncertainties in group delay are in the same order as the mechanical tolerances used to build CB-100.

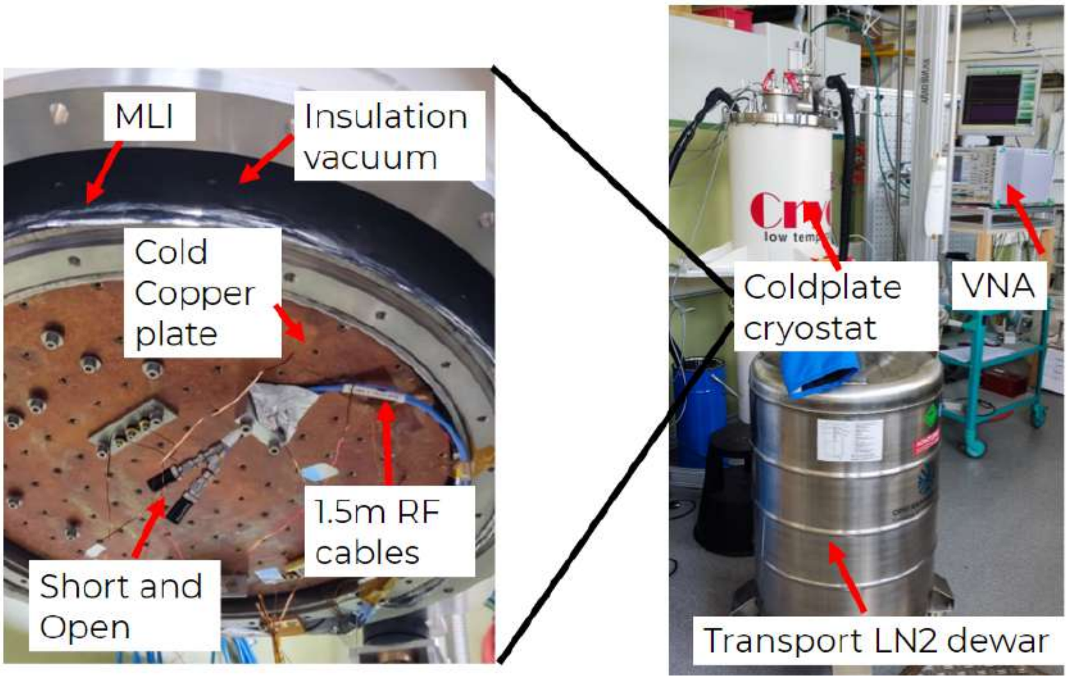

Figure 4.9: Setup used for the RF stability test using the cold plate cryostat. On the left, a zoom-in to the copper plate, where the RF cables and the calibration standards are thermally anchored from the bottom, while the liquid stays on the top.

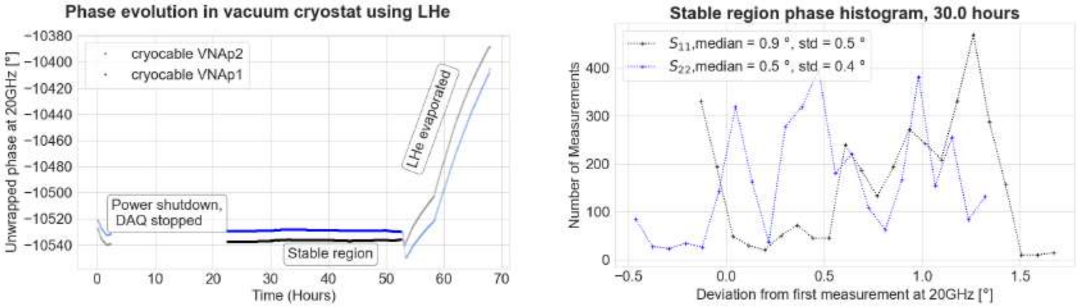

Figure 4.10: Stability of the cold plate cryostat, by measuring a short and an open standard at the end of the RF cables. Left: Unwrapped phase at 20 GHz as a function of time. Right: histogram of the phase variations with respect to the first measurement in the stable region of the cooldown.

We also measured the stability in the magnitude of S_{11}, as shown in Fig. 4.11. Note that the magnitude variations correspond to $\Delta S_{11} > 0$, or $S_{11}(t_2) > S_{11}(t_1)$ for $t_2 > t_1$, this suggests that the variations could still be dominated by the thermalization of the cables. Compared to the VNA baseline stability shown in Fig. 4.3, it is concluded that the stability degradation by

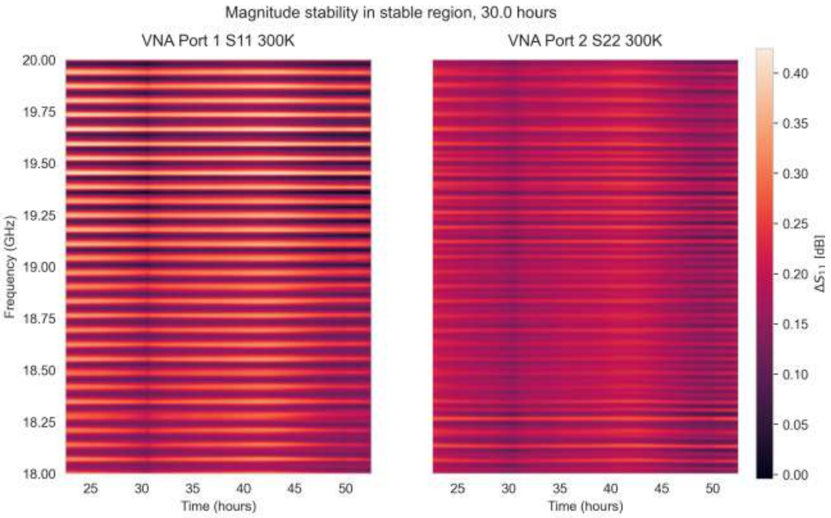

Figure 4.11: Magnitude stability of the cold plate cryostat setup measured by connecting Open and Short standards and measuring S_{11}.

the complex cryogenic system is greater than the baseline stability of the most simple setup at room temperature but still acceptable.

Finally, we ordered a set of semi-rigid cables from ICE-Oxford that will be used to connect the different components shown in Fig. 4.1. At the moment where I write this document they have not yet arrived, so no tests have been done. However, we made sure by a continuous discussion with the provider that they are cryo-compatible and feature an insertion and return loss below -15 dB between 18 to 20 GHz. Moreover, the cables are SMA-connected as they provide more stability than K-connectors and work properly for frequencies below 26 GHz. Finally, the connectors are non-magnetic to ensure that the connections do not suffer external forces inside the magnet during the ALP search run inside a magnetic field.

4.2.2 SP6T RF switch

A key component of the cryogenic setup shown in Fig. 4.1 is the SP6T RF mechanic switch used to move the reference plane to perform the reflectivity and receiver chain calibrations by means of the calibration standards. The standards are connected to the different switch ports. The propagation length for each position of the switch needs to be known with good precision, to determine the boost factor with enough precision.

The switch used is the SP6T Radiall R591722600 electro-mechanical switch. It is operated with a Keithley 7001 switch driver with a dedicated compatibility card developed by the electronics department at MPP, and powered by a DC power supply at 12 V that outputs a current of 50 mA when the switch is latched, and 0 mA otherwise. This switch was chosen because the different positions can be latched by sending a current to the component and activating a mechanical arm that closes the ports. This working principle is compatible with a cryogenic operation, in contrast with solid-state switches, where semiconductors might not work properly at low temperatures.

Room temperature characterization

As a first test, to determine the systematics induced by incorporating the switch in the signal path, we measured continuously each switch port with the VNA for 48 h to obtain the S_{j0} magnitude and phase stabilities as a function of time per port, where 0 denotes the center port (or pole), and j the different ports from 1 to 6. Fig. 4.12 shows the results of these tests.

It can be seen that the magnitude variation ΔS_{21} of S_{0j} (or S_{21} with respect to the VNA ports, where the VNA port 1 is connected to the switch pole and the VNA port 2 to one of the ports) was below 0.1 dB for all ports. This is one order of magnitude higher than the same study performed with the VNA only without the switch, shown in Fig. 4.3. In terms of phase, it can be seen that the measurements deviated at most 1.5° with a standard deviation of up to 0.38° at 20 GHz. This is higher but in the same order as the baseline phase stability obtained from the VNA only displayed in Fig. 4.4. It is possible that the day-to-day temperature fluctuations change the internal path lengths.

Another source of systematic uncertainty comes from the fact that when the switch is latched, a metallic arm physically falls in place and electrically connects the center port to one of the outer ports. The differences in how exactly the arm falls into place can lead to slightly different propagation lengths, hence it is an uncertainty source that needs to be characterized. The company states that the device features an excellent repeatability rate, but no measurement confirming this finding was found in the datasheet.

Even though the switch can be left in the same position for the data taking of the physics campaign, the calibration steps require sweeping through the different switch ports to perform all the required measurements for calibration, hence reproducibility is of utmost importance. To measure this, the switch transmission was measured with the VNA port by port, latching it first in the clockwise direction (1 to 6) ten times, and then doing the same in the counterclockwise direction (6 to 1). Table 4.2 and Fig. 4.13 show the results of this test.

Based on this test, we saw that the switch should be changed in counter-clockwise switching, as the magnitude variations are significantly smaller, and the phase variations are slightly lower. According to these measurements, we can state that the systematic error induced by switching is around 4° at 20 GHz, which is higher than the uncertainty induced by the cold plate cryostat and the VNA itself. It is worth noting that this uncertainty is intertwined with the uncertainties caused by the temperature changes from morning to evening, as completing the cycles required two full days of measurements (one for the clockwise switching, one for the counter-clockwise). In cryogenics, however, this effect would be suppressed.

Finally, it is important to know the propagation length from the switch pole to each of the switch ports. At room temperature this can be directly determined by doing a 2-port

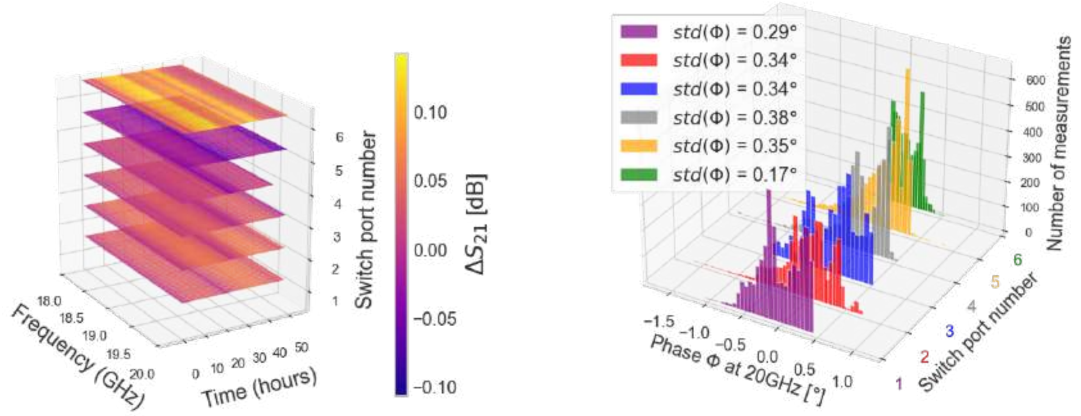

(a) Magnitude deviations from the first measurement after a calibration.

(b) Phase deviations from the first measurement after a calibration.

Figure 4.12: Radiall SP6T Magnitude and phase stability per switch port at room temperature using a two-port measurement in a 48 h period at room temperature. Once the switch is latched to a certain position, measurements are taken every 30 s, amounting to a total of $O(25.000)$ measurements to produce this study.

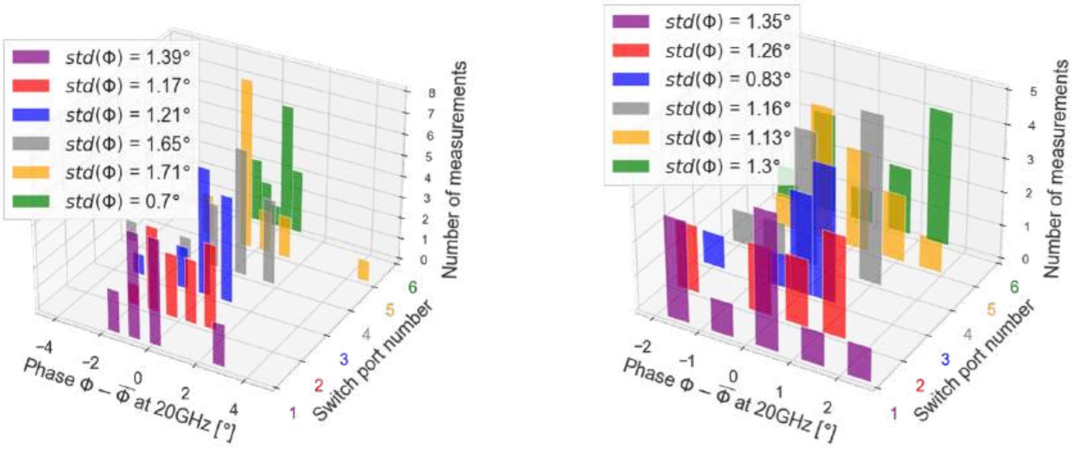

(a) Clockwise cycling at room temperature

(b) Counterclockwise cycling at room temperature

Figure 4.13: Switch cycling phase stability study at room temperature for clockwise (1 to 6) and counterclockwise (6 to 1). The setup used is shown in Fig. 4.2.

measurement where one of the VNA ports is connected to the center port (the pole) and the other VNA port is connected to one of the switch ports (as in Fig. 4.2). Then, by measuring $\angle S_{21}$, the propagation length can be obtained. Table 4.3 lists the electrical length found per port. We decided to study the propagation length in terms of phase because obtaining a group

	$\Delta\left\|S_{21}\right\|$ (dB)	$\Delta\angle S_{21}$ (°) (min-max)	$\Delta\angle S_{21}$ (°) (std)
Clockwise Cycling			
port 1	0.2	5	1.39
port 2	0.17	4	1.17
port 3	0.26	5	1.21
port 4	0.18	7	1.65
port 5	0.16	8	1.71
port 6	0.17	2	0.7
Counterclockwise Cycling			
port 1	0.05	5	1.35
port 2	0.07	4	1.26
port 3	0.02	3	0.83
port 4	0.08	4	1.16
port 5	0.1	4	1.13
port 6	0.1	4	1.3

Table 4.2: Results from the clockwise and anticlockwise switching of the Radiall SP6T R591722600 switch (Fig. 4.13).

Switch port	**Propagation length** ($\angle S_{21}$) $\pm 1.3^\circ$
1	-947.6
2	-948.4
3	-948.6
4	-945.9
5	-948.2
6	-949.1

Table 4.3: Measurement of the propagation length per port at room temperature by measuring the accumulated phase in a transmission measurement. Uncertainty provided from the switch cycling study at room temperature (Fig. 4.13)

delay induces statistical errors as a numerical derivative on noisy data needs to be done.

Cryogenic characterization

The stability of the switch was also characterized at cryogenic temperatures by inserting it on the cold-plate cryostat and driving it from the outside via seven ~ 1.5 m DC lines connected from the switch in the cold plate to the switch drive and the DC power supply at room temperature

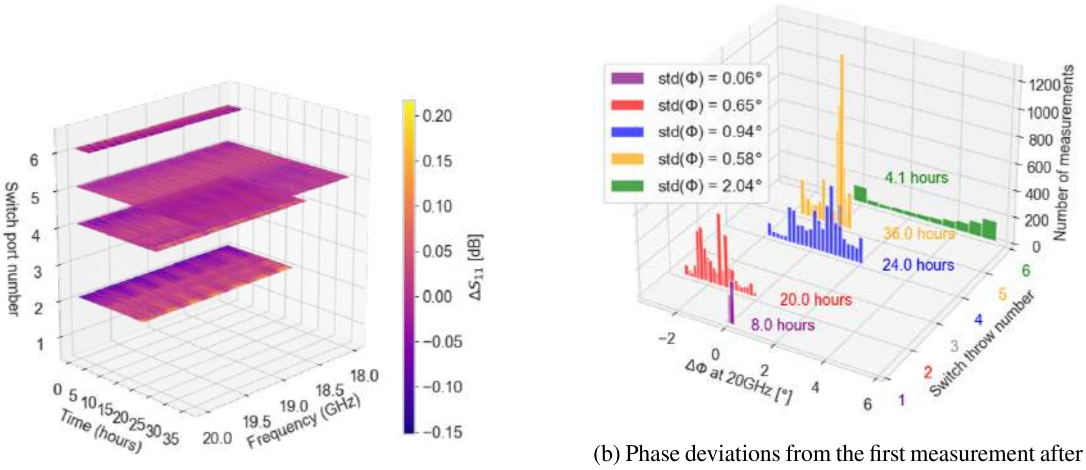

(a) Magnitude deviations from the mean.

(b) Phase deviations from the first measurement after thermalization.

Figure 4.14: Radiall SP6T Magnitude and phase stability per switch port at cryogenic temperatures using a one-port reflectivity measurement. Once the switch is latched to a certain position, measurements are taken every 30 s.

(corresponding to DC line 2 in Fig. 4.1). Fig. 4.14 shows the magnitude and phase stability for a continuous measurement over several hours per port. One of the differences from the study at room temperature (see Fig. 4.12) is that the study was performed by measuring the reflection S_{11} instead of the transmission S_{21}, as it was not possible to manually connect the VNA cables to the different switch ports in the same thermal cycle.

Port 1 could not be measured because a mismatch standard (Rosenberger 46A24) was connected to it and proved to degrade its frequency response at low temperatures. port 3 was not measured either because the switch did not close the path correctly, distorting considerably the reflected signal. This had not been observed at room temperature, but later we learned that it could be easily fixed by unlatching and latching again the port of interest. port 6 was measured for a short period of time because it was the last one to be latched and the helium evaporated completely after ∼ 4 h, this is why for port 6 the phase variation is skewed to positive values, indicating that the electrical path (including RF cables) began to thermally change.

Comparing these results to the ones displayed in Fig. 4.12, an uncertainty roughly twice as high was found. Note that this uncertainty not only comes from the switch but also from the cryostat with RF cables without the switch (see Section 4.2.1). In fact, the uncertainties found here are comparable to those found for the mentioned study, so we conclude that the switch uncertainty (once the port is latched) is sub-dominant with respect to the uncertainty generated by the cold plate cryostat.

Another important reproducibility test, as motivated in Section 4.2.2, is the estimation of the uncertainty generated by the randomness in the latching. At room temperature, we found that the switch should be operated in a counter-clockwise manner (switching from 6 to 1). At 8 K,

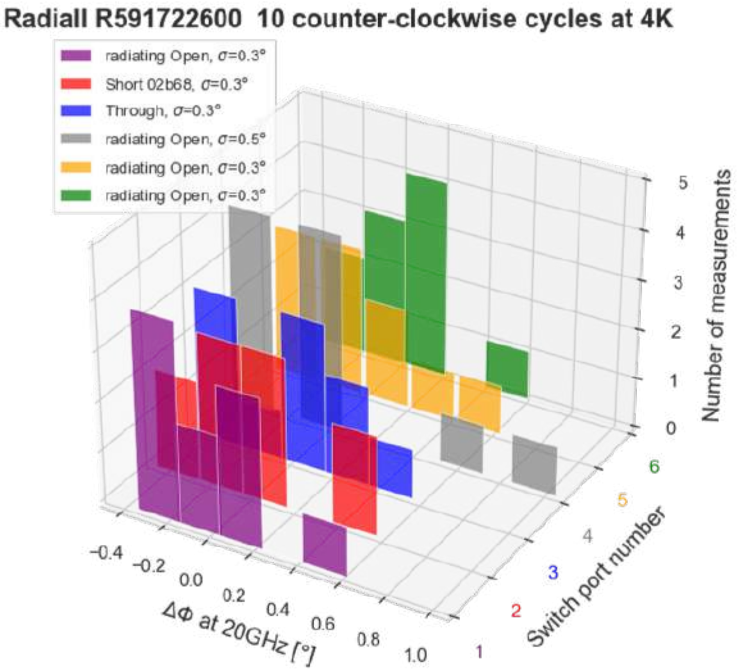

Figure 4.15: Switch phase stability for 10 full counter-clockwise cycles at 8 K

10 full counter-clockwise cycles were performed. Results are shown in Fig. 4.15.

A temperature sensor sensitive to mK variations was placed on the housing of the switch. We noticed that when performing this test the switch could easily heat up by more than 1 K every few cycles. This can change the propagation length inside the switch and therefore we allowed for some time in between measurements to allow the switch to thermalize again. Hence, we could control doing the full study at a constant temperature of (8.5 ± 0.5) K. This had not been possible at room temperature and explains the improved performance in phase stability (see Table 4.2).

Finally, when determining the propagation length between the RF switch ports at room temperature, doing a calibrated $\angle S_{21}$ per port was enough. This cannot be done inside the cryostat: On the one hand, this would require six independent thermal cycles, each taking several days. On the other hand, the propagated length corresponds not only to the switch but also to the system made up of cryostat RF cables and feed-throughs. To address these problems, we performed two thermal cycles to measure the S-parameters of the setups sketched in Fig. 4.16. Here, the second VNA cable was connected to the third switch port. Switch port 2 was connected to the short calibration standard, and the other switch ports were radiating open[1].

Then, we calculated the additional accumulated phase in Fig. 4.16B with respect to the

---

[1] A radiating open refers to leaving the port physically open without connecting any standard.

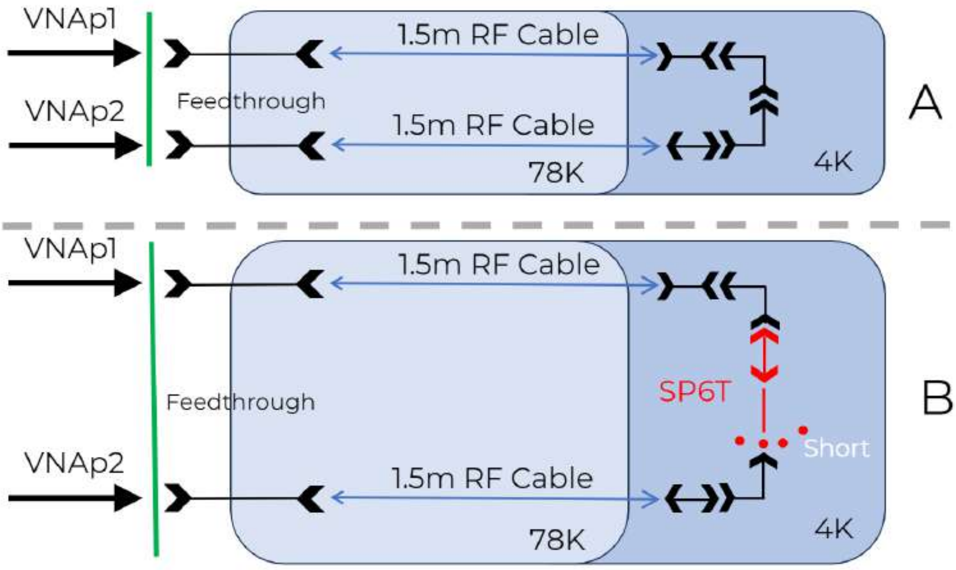

Figure 4.16: Switch internal propagation length measurement inside the cryostat after cooldown. First, a through is measured as a reference, and then in a second cycle the switch is connected in between. One of the VNA ports is connected to the switch pole, and the other to one of the ports.

reference *through* measurement, Fig. 4.16A, thus obtaining the propagation length from the switch center port to the third port (abbreviated as $L_3^{8\,\mathrm{K}}$). To obtain the length from the pole to each switch port, we consider that by cooling down the device, the physical dimensions and the electrical permittivity of the devices change. These properties are shared among all the switch ports (which are machined with the same materials thus having the same permittivity). Therefore, we postulate that the relative change for the propagation length of port 3 at 8 K is the same as the relative change for any other switch port:

$$\frac{L_3^{8\,\mathrm{K}}}{L_3^{300\,\mathrm{K}}} = \frac{L_i^{8\,\mathrm{K}}}{L_i^{300\,\mathrm{K}}}. \tag{4.2}$$

Where i denotes any of the switch ports, and each length is measured in terms of the accumulated phase. Rearranging this equation, we obtain

$$L_i^{8\,\mathrm{K}} = \frac{L_3^{8\,\mathrm{K}}}{L_3^{300\,\mathrm{K}}} \times L_i^{300\,\mathrm{K}}. \tag{4.3}$$

Where all the terms on the right-hand side are known, the propagation length for each switch port at 8 K can be obtained. The uncertainty is calculated by the Gaussian propagation in Eq. (4.4) and is dominated by the uncertainty between thermal cycles (Section 4.2.2), the phase stability in the cryostat setup (Section 4.2.1), and counterclockwise cycling at 8 K (Fig. 4.15)

$$\Delta T_i^{8\,\mathrm{K}} = T_i^{8\,\mathrm{K}} \sqrt{\left(\frac{\Delta T_i^{8\,\mathrm{K}}}{T_i^{300\,\mathrm{K}}}\right)^2 + \left(\frac{\Delta T_i^{8\,\mathrm{K}}}{T_3^{8\,\mathrm{K}}}\right)^2 + \left(\frac{\Delta T_3^{300\,\mathrm{K}}}{T_3^{300\,\mathrm{K}}}\right)^2}. \tag{4.4}$$

Switch port	**Propagation length at 4 K [°]**	**Propagation length at 300 K ±1.3°**
1	-1304 ± 2	-1307.6
2	-1304 ± 2	-1308.4
3	-1304 ± 0.8	-1308.6
4	-1302 ± 2	-1305.9
5	-1304 ± 2	-1308.2
6	-1305 ± 2	-1309.1

Table 4.4: Measurement of the propagation length per port at 8 K by measuring the additional accumulated phase in a transmission measurement at switch port 3 with respect to a through measurement.

Results are listed in Table 4.4. Note that to perform the through measurement, a female-2.92mm to female-2.92mm connectors (fk-fk) adapter was used to connect both male-ended RF cables. Then, a male-male adapter was connected to the center port of the switch, so that the RF cables could be connected to it without removing the fk-fk adapter. The male adapter has a propagation length of $\sim 360^\circ$ and has not been incorporated in the room temperature measurements shown in Table 4.3. For comparison purposes, Table 4.4 also contains the propagation lengths at room temperature of the switch including this adapter. Since the male adapter does not need to be disconnected from the switch in the final setup, this can be effectively understood as having defined a new switch, with a longer propagation length.

Accuracy in the normalization measurements

To verify that the procedure outlined in Fig. 4.16 is valid, we carried out the following test: Fig. 4.17 shows the two thermal cycles used for this study. These measurements had already been made for different purposes: Fig. 4.17A corresponded to the switch stability measurement at 8 K shown in Fig. 4.14, while Fig. 4.17B corresponded to the measurement taken to determine the propagation length between the switch pole and its different ports, as shown in Fig. 4.16.

Note that the addition of adapters in the cold stage adds an additional unknown propagation length, which cannot be de-embedded because measuring the accumulated phase in the adapters would require yet another thermal cycle. Instead, considering that in both cycles port 2 has the standard short connected, and ports 4, 5, and 6 radiating open, then, ideally

$$\left.\frac{\angle S_{22}}{\angle S_{44}}\right|_{\text{cycle A}} = \left.\frac{\angle S_{22}}{\angle S_{44}}\right|_{\text{cycle B}}, \tag{4.5}$$

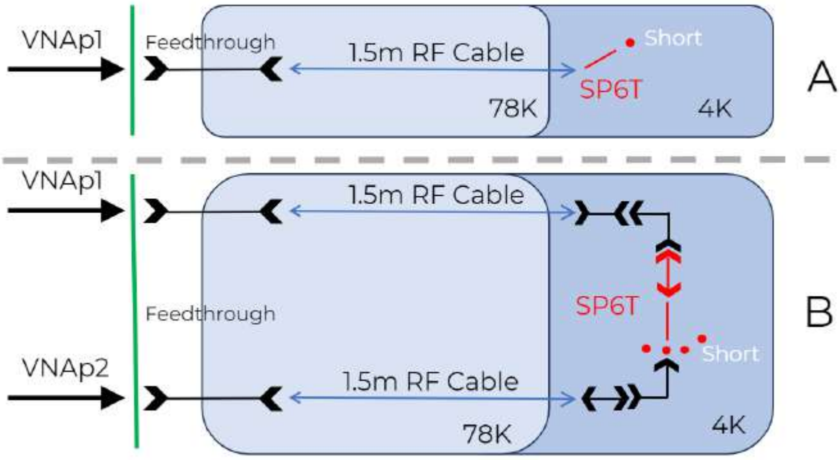

Figure 4.17: Measurements used to estimate the systematic uncertainty induced by performing different thermal cycles in the cold plate cryostat.

as only the relative length between ports 2 and 4 would change the ratio, and this relative length is the same on both thermal cycles. Note that similar ratios can be defined with the other switch ports. Table 4.5 shows all the ratios that can be derived and the values obtained.

Ratio	**Cycle A**	**Cycle B**	Rel. diff. [%]
2 to 4	1.00463	1.00411	0.051
2 to 5	1.00460	1.00397	0.063
2 to 6	1.00465	1.00450	0.015
4 to 5	1.00002	1.00014	0.012
4 to 6	1.00000	0.99962	0.036
5 to 6	1.00005	1.00053	0.048

Table 4.5: Ratios defined for the determination of the uncertainty caused by performing multiple thermal cycles to measure the ratio between two propagation lengths, and their relative differences. *X to Y* means the ratio between the unwrapped phase of switch ports *X* and *Y*. Ports 1 and 3 were not used because they had different components connected on each cycle

The mean error $\overline{e}$ and standard deviation σ_e from these six measurements is 0.037 % and 0.019 %, respectively, so $\overline{e}+\sigma_e \approx 0.056\,\%$. The maximum deviation found is similar, at 0.063 %. Therefore, the phase uncertainty produced by normalizing two uncalibrated propagation lengths is estimated as ±0.03 %.

4.2.3 LNA

The LNA used is the model **LNC_6_20** from Low Noise Factory [56], as it is cryo-rated and provides a low system temperature and high gain. In terms of the frequency range in which the setup can be used, the LNA is suitable for the CB-100 setup but also for the limiting factor, as it is rated for operation between 6 to 20 GHz both at room temperature and cryogenic temperature. As motivated in Section 2.3, measuring the internal length from the input port of the LNA and the distance to the gain point, as well as the input impedance, modeling the noise interference produced by the LNA and CB-100 noise(see Section 2.7 and Section 2.3) is crucial. At room temperature, a measurement of the internal length can be done by simply calibrating the VNA with the auto-calibration kit, and connecting the input LNA port to the VNA after providing the correct bias current and voltage. The input impedance can be obtained by measuring S_{11}: the incident wave will travel some distance and then be partially reflected at the gain point of the amplifier. The reflected part will travel back to the VNA port. This can then be plotted on the Smith chart, as shown in blue in Fig. 4.18 (left).

As expected, S_{11} corresponds to a line on the Smith chart, that cycles through the chart as frequency increases. Because the S-parameter can be parameterized as $S = |S|\, e^{i\phi}$, it is clear that a full cycle on the Smith chart will happen each time the phase ϕ varies from 0 to 2π. However, if the reference plane is moved to the gain point exactly, there is no electrical length over which the wave can accumulate phase, so the S-parameter reduces to a point in the chart: $S = |S|\, e^{i\phi(\nu)} = |S|\, e^{i\phi_0} = S_0$. Moreover, since impedance at that point should be real only (no capacitive or inductive reactance)[2], then $S_0 = \Re(S_0)$ and $\Im(S_0) = 0$ for all frequencies. In particular, if we now define the parameter P as

$$P(L) = \sum_{i}^{N} \left| \Im(S_{11}^{i}) \right|^2 . \tag{4.6}$$

Where the dependence of P on the length that the reference plane was changed is explicit. Here, the frequency points measured are $\nu \in (\nu_1, \nu_N)$ and S_{11}^{i} is the S-parameter S_{11} measured at the frequency point ν_i. From the previous reasoning, P is zero when the length between the reference plane and the gain point of the amplifier is zero.

From this reasoning, we created an algorithm that changes the reference plane in a loop by small distances ΔL and then calculates and stores $P(L_k)$ in a list $\bar{P}$. This is done within a user-defined range $[x_i, x_f]$. The algorithm chooses the length L_0 such that $\min(\bar{P}) = P(L_0)$[3].

Fig. 4.19 shows the result of this procedure at 4 K, while the convergence curve for both cryogenic and room temperature can be found in Appendix B. The reference plane has effectively been moved from the VNA to the LNA reflection point from the input, which we assume to be

---

[2] This is because if the distance between the reference plane and reflection plane is zero, then for all frequencies (down to DC), the phase should be exactly the same, and at 0 Hz the phase must be 0° by definition, so for all frequencies, the phase must be 0°, leaving the point on the smith chart on the real axis.

[3] The implementation of this algorithm is stored in this thesis' repository under the name **LNA_Optimization**.

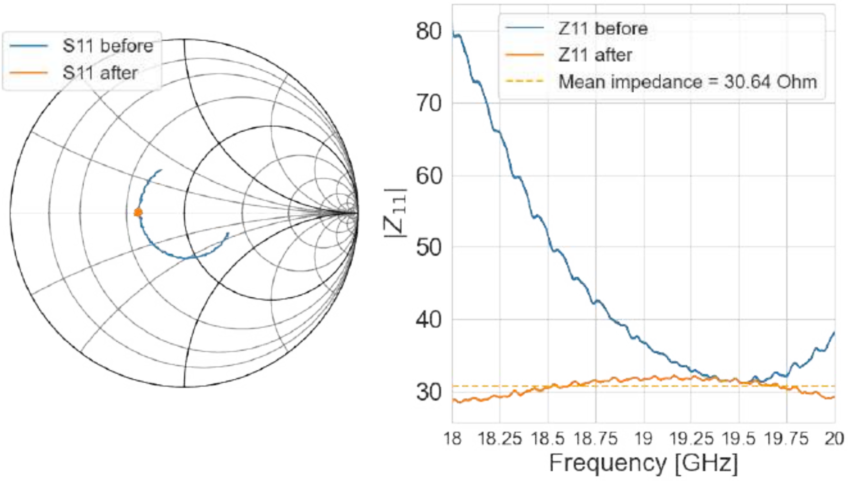

Figure 4.18: Room temperature reflectivity measurement of the LNA input, and de-embedding result from the optimization algorithm, showing the impedance at the reflection point.

the gain point. L_0 corresponds to the distance to be applied in the LNA-CB-100 noise model and the impedance at that point determines the impedance mismatch between CB-100 and the amplifier.

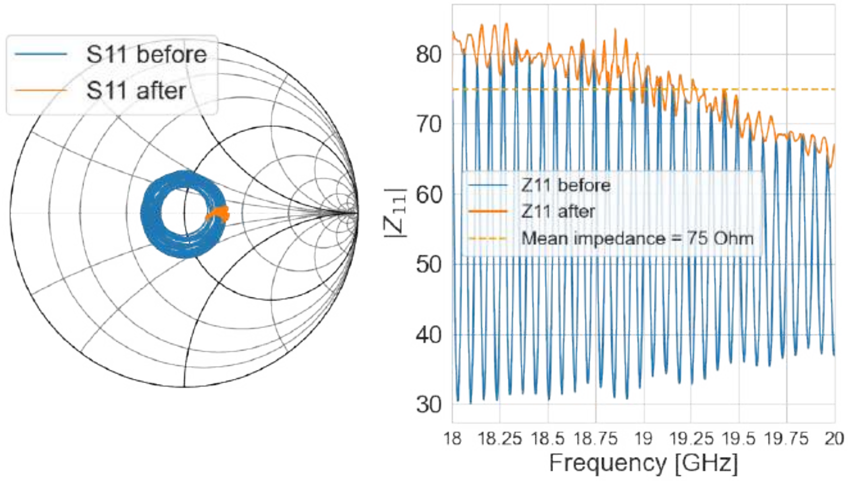

Figure 4.19: LNA internal length de-embedding algorithm results at 4 K. Comparison between the original measurement and the length-de-embedded network for S_{11} and the input impedance Z_{11}

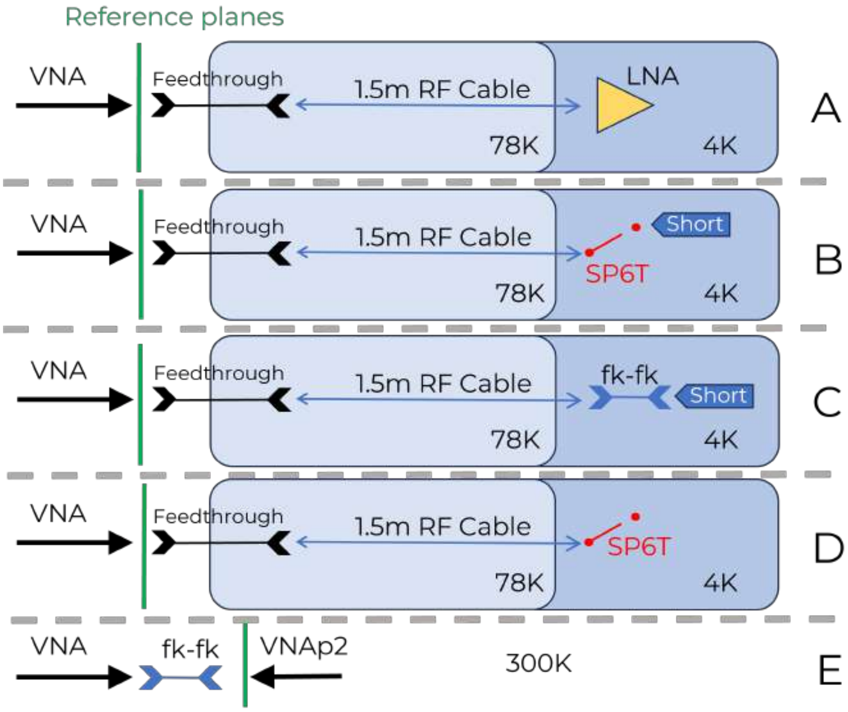

Figure 4.20: Different measurements were performed to obtain the internal lengths of the switch ports and the LNA at cryogenic temperatures without an in-situ calibration. Each measurement is independent from each other, all of them use one port of the VNA.

Note that the length propagated by the wave does not correspond to the internal length of the LNA, but to the combination of the feedthrough, cryostat cables, and amplifier, as displayed schematically in Fig. 4.20A. By applying the algorithm described above, we obtain a length of 1 523 mm assuming that the dielectric media is Teflon, with $\epsilon_r = 2.1$. The cryostat cable was physically measured to be 1.5 m long. A few centimeters result from the other components. By using the found impedance $Z_{LNA}(4\,\text{K}) = (75 \pm 5)\,\Omega$, the LNA reflection coefficient at 4 K can be computed to be $\Gamma_{LNA}(4\,\text{K}) = 0.20 \pm 0.03$.

As the length found using the configuration shown in Fig. 4.20A. corresponds to the full setup and not only the internal length. Fig. 4.20 B to E denote the measurements that need to be done to calculate the internal length of the LNA. The phases accumulated by different components attached to the LNA need to be arithmetically subtracted to obtain the phase accumulated by the LNA only. Specifically, note that

$$\angle S_{11}^{\text{LNA}} = \angle S_{11}^{A} - [\angle S_{11}^{C} - (\angle S_{11}^{B} - \angle S_{11}^{D}) - 2 \cdot \angle S_{21}^{E}]. \tag{4.7}$$

Then, using the measured accumulated phases as shown in Table 4.6, the internal electrical

Measurement	**Φ(20 GHz)** [°]
S_{11}^A	-106012 ± 32
S_{11}^B	-109790 ± 33
S_{11}^C	-105435 ± 32
S_{11}^D	-109285 ± 33
S_{21}^E	-366.0 ± 0.4

Table 4.6: Obtained unwrapped phases at 20 GHz for the measurements sketched in Fig. 4.20. Uncertainty is given by thermal cycle reproducibility (see Section 4.2.2)

distance from the LNA input to the gain point can be calculated with Eq. (4.1) up to the permittivity factor, which is not required for this study.

The results yield $\Phi_{\text{LNA}}(4\,\text{K}) = (-1\,841 \pm 67)^{\circ}$, which corresponds to a group delay of $\tau_{g,\text{LNA}}(4\,\text{K}) = (127.85 \pm 4.65)$ ps, and a length of $L_{\text{LNA}}(4\,\text{K}) = \epsilon_r^{-1/2}(4K)(38 \pm 1)$ mm.

Assuming a relative permittivity of $\epsilon_{4K} = 32$ as in the room temperature case [4], this becomes $L_{\text{LNA}}(4\,\text{K}) = (6.7 \pm 0.2)$ mm, which is in the same order of magnitude as the length found at room temperature $L_{\text{LNA}}(300\,\text{K}) = (8.180 \pm 0.010)$ mm. The difference between both partly comes from thermal shrinkage at cold, and partly due to the unknown temperature-induced change of the permittivity.

In terms of the gain of the LNA, as usual in amplifiers, we choose an amplifier with a gain such that any amplified measurement is at least 10 dB above the baseline of the SA, low enough such that the maximum expected incoming power from any measurement does not exceed, after amplification, the saturating power of any other component in the setup. In this case, 30 dB in gain both at room temperature and at 4 K fulfills both conditions.

All the phases measured in Fig. 4.20 are listed in Table 4.6. The phase stability of the LNA measurements was also derived by repeating the measurement A in Fig. 4.20 at cold over three days. The results are shown in Fig. 4.21.

It can be seen that the stability of these measurements is comparable to the phase stability found measuring the calibration standards and the RF cables inside the cryostat, shown in Fig. 4.10. Therefore, we conclude that the addition of the LNA does not degrade the phase stability of the setup, as its systematic is dominated by the RF cables inside the cold plate cryostat.

4.2.4 Directional coupler

As explained in Section 1.2.2, a directional coupler or circulator is needed to provide independent paths for the incoming and the outgoing waves in the S_{11} measurement. In literature, many

---

[4] This value was used in the room temperature study because the physical length becomes roughly half of the LNA physical dimensions

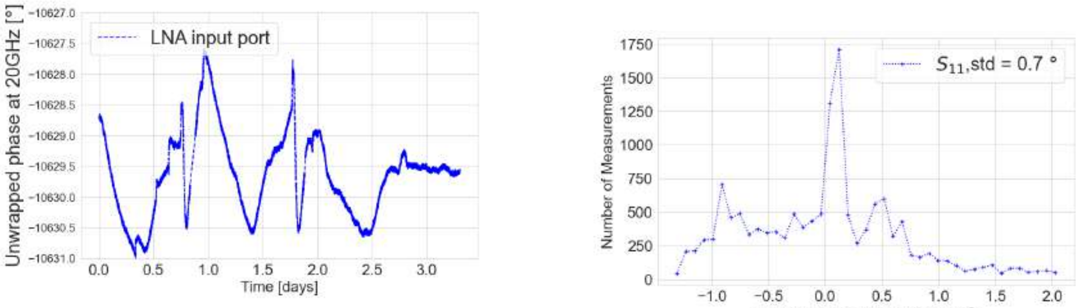

(a) Time evolution of the unwrapped phase. The y-values correspond to the unwrapped phase in a span of 2 GHz, whereas in Table 4.6 they correspond to a span of 20 GHz.

(b) Stability histogram of the phase deviations at 20 GHz with respect to the mean after the setup had thermalized.

Figure 4.21: Phase stability from the LNA S_{11} measurements at 4 K over a period of three consecutive days.

authors have used circulators as they offer the additional advantage of minimizing back-reflections [19, 36, 65]. Applications of these setups include quantum computing where the setup is not inside a strong magnetic field, or alternative axion-search experiments where an active magnetic shield is put above the cavity to protect the electronics. However, in the case of MADMAX where the full prototype setup is planned to be inside a 1.6 T dipole magnet, and later potentially at ~ 10 T, circulators can be problematic as they are ferrite-based components that feature large magnetic field dependence, especially in terms of the pass-band frequency. As an alternative, we propose the use of a directional coupler, which should not change its RF response considerably in the presence of a strong magnetic field. We ordered the 10 dB coupler from Marki microwave CE10-1R540 [63] and performed reflectivity measurements with the VNA at room temperature to determine whether the device is fully reciprocal, and if not, which orientation provided the best values for our tests. The directional coupler is a 4-port device, hence in total 16 S-parameters are needed to determine the $S_{4\times4}$ matrix. These parameters can be obtained in a series of measurements with the VNA.

The results are displayed in Fig. 4.22. To choose the port configuration in which the coupler should be used, the following parameters need to be considered: lowest return loss (Fig. 4.22(b)) to avoid reflections from the signal back to the source, highest isolation (i.e., lowest transmission coefficient in the isolating direction) (Fig. 4.22(c)), and lowest insertion loss on the direct path (i.e., highest transmission) (Fig. 4.22(e)). We conclude that the coupler features a better RF response when selecting ports 1 and 4 as direct paths and 3 and 2 as coupled paths. Moreover, S_{44} features the lowest insertion loss for the most part of the frequency range studied, so it should be connected to the output of CB-100 in the calibration scheme shown in Fig. 4.1. With that orientation, the VNA input port should be connected to the second port of the coupler, and port 1 to the LNA input, as shown in Fig. 4.22(a).

Finally, we determined the internal path traversed by the signal in the direct path, as this

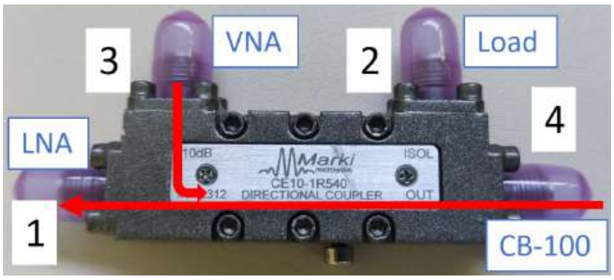

(a) Directional coupler used for the cold calibration. The ports are numbered in the results as displayed on this picture, and in blue the components that should be connected to each port given the selection based on return and insertion loss of the direct path.

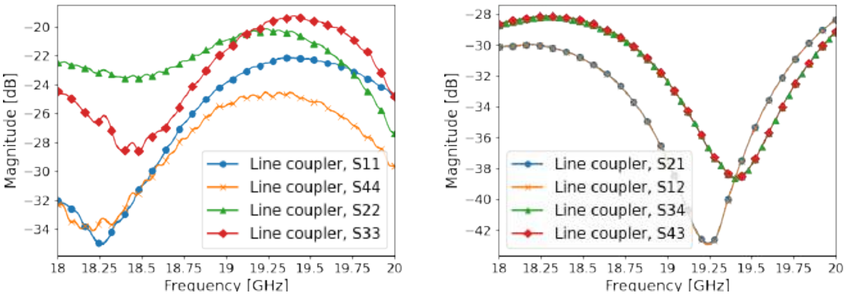

(b) Return loss

(c) Isolation

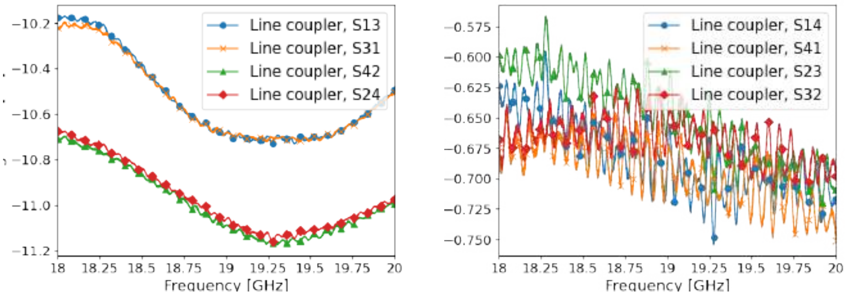

(d) Insertion loss on coupled path

(e) Insertion loss on direct path

Figure 4.22: Reflectivity measurements for the four possible Marki microwave 10 dB directional coupler orientations at room temperature.

additional length will change the noise interference pattern. From the S_{14} measurement, we obtain at room temperature $L_{\mathrm{coupler}} = \epsilon_r^{-1/2} \times (92.48 \pm 0.02)\,\mathrm{mm}$, or $\Phi = (2\,219.6 \pm 0.3)^\circ$ at 20 GHz.

4.3 Montecarlo simulation of the boost factor

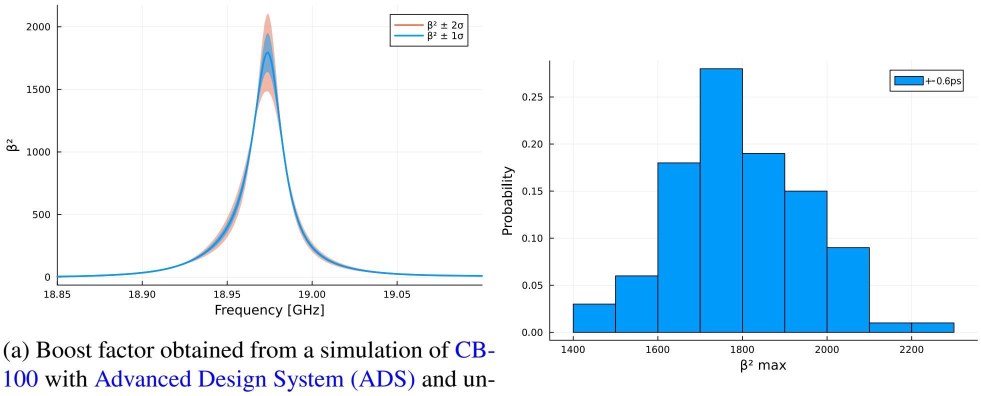

(a) Boost factor obtained from a simulation of CB-100 with Advanced Design System (ADS) and uncertainty generated by phase instabilities in the order $\sigma_\phi \approx 0.6\,\text{ps}$.

(b) Boost factor distribution. the standard deviation obtained is $\sigma_{\beta^2} \approx 200$.

Figure 4.23: Resulting uncertainty on the boost factor obtained by running a Montecarlo simulation of the setup on ADS with 100 samples.

Variable	**Uncertainty σ**	**How it was Obtained**
Vacuum cryostat stability over three days	0.4 dB, 1.7°	48 h Stability measurement of S_{11} with short and open standards (Fig. 4.10,Fig. 4.11, Fig. 4.21).
Accuracy in derived phase measurements for different thermal cycles	0.03 %	Six identical measurements with a full warm-up and cool-down cycle of the vacuum cryostat (Section 4.2.2).
SP6T switching reproducibility at 8 K	0.1 dB, 0.5°	ten full counter-clockwise switching cycles from throw 6 to 1 in decreasing order, measuring S_{11} within ±0.5 K(Fig. 4.15).
Estimated total phase uncertainty	10 %	Gaussian propagation with the uncertainties found in the listed measurements.

Table 4.7: Summary of systematic uncertainties found at cryogenic temperatures below 9 K in the cold plate cryostat. Phase uncertainties are provided at 20 GHz

The dominant uncertainties found in this work that could induce a systematic uncertainty on the determination of the boost factor are listed in Table 4.7 (a more comprehensive list can be found in Appendix C). These uncertainties correspond to actual physical changes in the electrical path where the waves propagate and therefore induce instabilities in the boost factor that can be quantified as a resulting systematic uncertainty.

It is possible to simulate CB-100 as an electrical circuit with sources of current that mimic the electromagnetic emission from the discs due to the dielectric discontinuities in the presence of an axion field (see Fig. 1.2(b)). This simulation was created by the MADMAX collaboration in ADS [68] and can also be used to run a Montecarlo simulation with the propagation length uncertainty found in this work.

With a propagation length of $\sim 60\,\mathrm{cm}$ between LNA input and booster, the thermal cycle reproducibility test yields an uncertainty of $\sim 4.3^\circ$ for air permittivity, which is the case for most of the booster. Then, the total uncertainty from the tests in Table 4.7 yields $\sigma \approx 4.6^\circ \approx 0.6\,\mathrm{ps}$, calculated by Gaussian propagation. Assuming a uniform distribution for the phase stability uncertainty, the distance between LNA input and booster can be perturbed to estimate its effect on the boost factor. The result is displayed in Fig. 4.23.

With this simulation, and the systematics determined for the proposed cryogenic setup in this work, the uncertainty induced on the boost factor is in the order of $10\,\%$ at 2σ.

CHAPTER 5

Conclusions and outlook

This work comprises two main developments within the MADMAX experiment. The first one is a monitoring system to control the data quality and estimate the total integration time during data-taking. It also allows for fast response from the experiment operators in case intervention is needed. This system was used for the first time during the 2023 MADMAX campaign in Morpurgo at CERN.

The main achievement of this work is the proposal and development of a single thermal cycle calibration and operation setup for the CB-100 prototype setup at cryogenic temperature, allowing semi-automatic *in-situ* reflection and receiver calibration, as well as data-taking. The systematic uncertainties induced by this setup were studied and minimized at cryogenic temperatures below 9 K. The tests performed include phase stability as a function of time for the VNA, RF components and the cryostat setup, impact in reproducibility and stability generated by mechanically latching a six-port RF switch, and reproducibility of measurements from different thermal cycles. As a result of this thesis, the systematic uncertainty due to these factors could be individually assessed and partly reduced. They were determined to be $\sigma \lesssim 0.6\,\mathrm{ps} \approx 4.5^\circ$ at 20 GHz.

The noise-interfering pattern generated by the LNA mismatch with respect to the booster needs to be understood to determine the boost factor. Measuring the propagation length for each switch port positioned between the LNA and CB-100 is crucial. For the switch ports, we indirectly derived these propagation lengths at 8 K with an uncertainty of $\lesssim 0.3\,\mathrm{ps} \approx 2^\circ$ at 20 GHz. For the LNA, we developed an optimization algorithm to find the propagation length based on a reflectivity measurement. We found this propagation time and length within $\sim 67\,\mathrm{ps} \approx 0.2\,\mathrm{mm}$ assuming a relative permittivity of $\epsilon_{8\,\mathrm{K}} = 32$.

By introducing the reproducibility and stability uncertainties found in this work in a Montecarlo simulation we were able to estimate that the proposed cryogenic setup will induce an uncertainty of $\Delta\beta^2 \sim 5\,\%$ on the boost factor of the experiment. These simulations considered only the phase instabilities caused by the setup and not the magnitude variations, which although expected to be sub-dominant, should be included in the future. From the boost factor expected precision, we conclude that this setup should be further investigated as it constitutes a promising avenue for the cryogenic operation of the dielectric haloscope prototype in the frequency range 18 to 20 GHz.

We conclude that the proposed setup in Fig. 4.1 profiles as a promising avenue to achieve the cryogenic operation of CB-100 for ALP searches. However, important tests still need to be performed to determine the systematics induced by the cryogenic setup in full and the consequent boost factor uncertainty. We suggest the following measurements to continue this investigation:

- One port reflectivity calibration: We propose initially a SOA one-port calibration to move the reference plane to the booster input port. This proposal needs to be tested and optimized. Moreover, systematic uncertainties from the semi-automatic calibration with the RF switch and calibration standards at cryogenic temperature need to be determined.
- Cryogenic load: We propose a terminated attenuator, which will act as a cryogenic load. The reflectivity response of this component needs to be tested to check if it behaves as a *load* (as a rule of thumb, $S_{11} < -30\,\mathrm{dB}$ for the frequency range of interest).
- Power calibration: We propose a power calibration by attaching a heater to the cryogenic load and taking noise measurements with the SA at different temperatures by heating the load, to then perform a power calibration as outlined in Section 2.4. The feasibility of this approach and induced uncertainties need to be determined.
- User-induced reproducibility: When the cryogenic setup is fully mounted inside the cryostat, the operator has a degree of variability in the torque applied to each connection and the position and bending of each cable (even if using specialized tools such as a torque wrench). This induces a physical change in the overall propagation length for the waves that can be characterized as a phase uncertainty.
- Thermal cycle reproducibility: When a new thermal cycle is performed, the difference in the temperature gradients of the RF cables produce a change in the electrical length for the waves propagated. To quantify the systematic uncertainty induced by this variable at least two identical measurements need to be performed after two independent cooldowns, without manipulating the RF circuitry (i.e., without reconnecting any component).

APPENDIX A

MADMON implementation details

User-defined parameters

All the user-defined parameters are located on top of the script, before importing the needed libraries. Each parameter contains a brief explanation of what is expected and should be self-explanatory on its own. However, some remarks could be useful:

- **boundaries**: For plotting purposes, what is the expected range of noise temperature and physical temperatures in the experiment? This only changes the visualization of the monitoring plot, not the calculations and derived parameters.

- **paths**: They specify which folder contains the required files for the script to run, as it was desired that the code could run not only on the DAQ machine but on any that has the files to be monitored to increase the reproducibility, understanding, and confidence of the measurement campaign.

- **filter window and exclude points**: These parameters define how the Savitzky-Golay filter will be applied. As this filtering can cause problems near the edges of the dataset, some points are excluded, usually corresponding to half of the filtering window. These parameters are important as they can cause under-fitting of the noise measured, thus leaving non-gaussianities present for the subsequent data analysis, or over-fitting, thus hiding a possible axion-induced excess power.

- **calibrations**: In principle, during a long data-taking run several calibrations must be performed once the inverse variance shows a non-Gaussian time evolution. By providing the date and time at which these calibrations are performed, the code can automatically apply the calibrations to the datasets based on the times that they were acquired.

Libraries needed

After the user parameters are defined, the required libraries are imported. Most of these libraries are included by default in a comprehensive Python installation, more specialized libraries such as smptplib,ssl, and email.message might have to be installed, which can be simply done using *pip*.

In particular, it is worth noting the use of the garbage collector library. This is a good memory safety measure for codes that should run for longer periods, such as a monitoring system. The use of this library to free up unused allocated memory proved to be useful in avoiding sudden crashes in this case, as there are constantly new files being acquired and processed.

Functions

get_B_field

This function retrieves the data read by the gaussmeter and stored by the DAQ machine and saves it to a list including its timestamp. If the value is under some threshold (here set to 1.5 T, an alarm is triggered and an e-mail is sent to the operators.

Get_time_days

All the data shown in the monitoring plot should be synchronized in time. This is difficult because there are different DAQ systems for different variables: the power measured by the SA has a dedicated DAQ system, whereas the temperature sensors have a different one. There is a third one for the magnetic field measurements. Each DAQ system has a different sampling rate, name conversion, and time with respect to which the date and time are stored. More specifically, the power files are stored every $\sim$ 12 min in different *.smp* files which store the date and UTC time when the file was acquired in the filename, with the format YYYYMMDDHHMMSS. Then, the temperature readings are stored every minute by appending rows to a notepad. The first two columns of each row contain the date (DD/MM/YYYY) and time (HH:MM:SS) by using the DAQ machine clock, which is synchronized with Central European Time (CET). Finally, the B field is stored in a similar way to the temperature, but synchronized with the local time. Since the European time change from winter saving to summer saving happened in the middle of the run, for some files the B field and temperature were synchronized, while for the other, there was an offset of 1 hour.

The difference between all the conventions comes from the fact that each DAQ system was developed independently. This was a nuisance that could have been easily avoided but was found only when we started taking data, so an alternative more complex solution had to be implemented. This function shifts all the dates and times to synchronize all the files with respect to the UTC time.

Send_alert

We organized a shifter group to look at the monitoring system three times a day, as many possible data irregularities would need some time to develop before deciding whether to interrupt the experiment or not. However, there were some possible problems that would require immediate attention. These problems include:

- The magnetic field measured falling below 1.5 T would mean that an unplanned ramp-down was taking place. The time when $B \approx 0\,\mathrm{T}$ is effectively additional deadtime for the experiment, as we rely on the strong magnetic field to produce the axion-induced signal.
- Corrupt files: It is possible that a miscommunication between the SA and the DAQ machine caused a corrupt file to be stored. This however is usually fixed by the DAQ code. However, if several corrupt files have been stored uninterruptedly, this could mean that the cause needs to be manually investigated.
- No files: If the DAQ machine fails to trigger the SA, no new files will be received, which means loss of data. In this case, a manual restart of the DAQ code needs to be performed
- Overheating: DC power instabilities could lead to overheating of the active components, namely the LNA and the SA. Therefore, an alarm is triggered if the physical temperatures read by the PT-100 sensors on these devices are greater than 25 °C, which would represent a 20 % increase with respect to the nominal temperature of the experimental area.

If MADMON detects any of these problems, an alarm is sent via e-mail to all the operators. For 2023, this proved to be useful to quickly solve many of these problems as quickly as possible. In particular, when the electric storm in Prevessin caused a power shut-down in the North Area that turned off the magnet, a manual on-site ramp-up of the magnet was performed, thus having only 3 hours of 0 B field, instead of the $\sim$ 12 h that it would have taken a shifter to notice without any alerts.

Power_to_NoiseT

This function receives the uncalibrated power spectrum from the SA and returns the Y-factor calibrated spectrum, by following the procedure outlined in Section 2.4. Additional parameters that need to be provided are the line-de-embedded input impedance of the LNA, and the 40 MHz calibration files corresponding to the hot, cold, and baseline measurements.

Avg_noise_bins

This function divides the frequency span into several bins and computes the average noise temperature per bin. It receives the calibrated noise temperature spectrum and outputs an array containing the temperature per bin and average frequency per bin in a 2-column data frame. A free parameter is the desired number of bins, which was set to 5 for 2023.

Expectation

This function computes as a function of the time elapsed since the beginning of the data-taking process the expected integration time assuming the noise measured is Gaussian. This is done by using Eq. (2.12)

Running_Avg

When the DAQ code is restarted, either because of a crash or an intended intermediate calibration, it loses memory of the previously acquired files and does not take them into account to compute the average power spectrum. Therefore, MADMON computes the *last avg* file recursively, by saving the previous average and adding up a weighted new file. This means that MADMON is capable of producing a final average file by the end of the run, which can be used directly for data analysis and peak searches.

Save_data

All the quantities (measured and derived) shown in the monitoring plot are stored in different files as a checkpoint to ensure no data is lost and the evolution of the data acquired can be reconstructed. These files are light and therefore do not require binary or compressed storing. Simple *csv* files are thus preferred because they also allow an easier inspection.

MADMON_plot

This function takes all the measured and derived parameters and structures them on the different subplots. Finally, it saves the resulting plot in high-definition, overwriting the previous one to save disk space.

Script explanation

After the functions have been defined, MADMON can be run from the terminal by typing *python MADMON_9.py*. The code should be able to run at any time, not necessarily from the start of the run, as it might be wanted to update it or debug it in the middle of the run. Therefore, the first step of the script is to run all the needed calculations for all the existing files in the folders specified. The script will then output a monitoring plot and monitoring data files and will enter an infinite loop which can be stopped by typing *FINISH* in the terminal. In this loop, the code looks every 6 minutes for new data files stored by the SA DAQ code. If it finds new files, re-runs the monitoring, and updates the plot and the data files. Moreover, if any of the alarms are triggered, e-mails are sent to the operators every 10 minutes until the code is silenced or the error is fixed.

APPENDIX B

Convergence of optimization algorithm

The optimization algorithm objective parameter introduced in Eq. (4.6) shows a high degree of convergence and no local minima. Fig. B.1 shows $P(L)$ computed for a range of possible lengths that include the de-embedding length. This was repeated in broader length ranges, always reaching the same minimum.

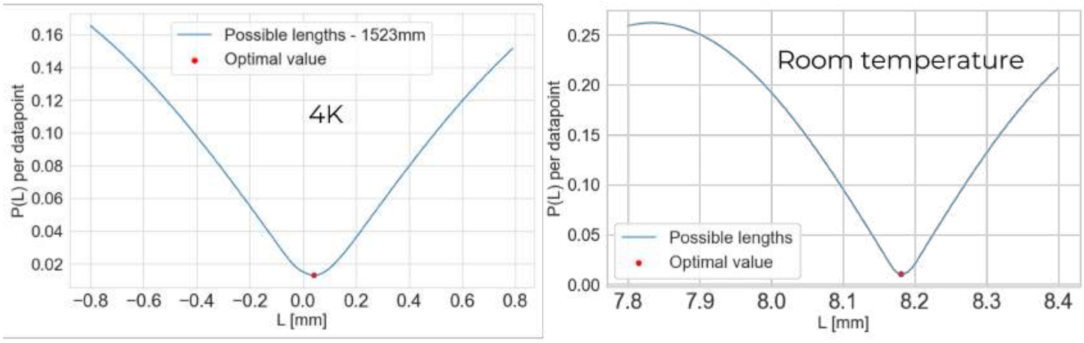

Figure B.1: Convergence of the optimization algorithm for the measurements at room temperature and at 4 K. Local minima were not found regardless of the initialization of L or the step size ΔL

APPENDIX C

Systematic uncertainties

Table C.1: Table summarizing the systematic uncertainties induced by the full cryogenic setup proposed in Fig. 4.1. TBD stands for *to be determined*. Phase uncertainties are always given at 20 GHz

Variable	**Uncertainty σ**	**How it was Obtained**
VNA measurement stability	0.06 dB, 0.3°	24 h stability measurement of S_{21} in minimal setup (Fig. 4.4,Fig. 4.3), in agreement with [52].
Vacuum cryostat stability	0.4 dB, 0.7°	48 h Stability measurement of S_{11} with short and open standards (Fig. 4.10,Fig. 4.11).
LNA phase stability at 4 K	1.7°	3-day stability study of S_{11}(Fig. 4.21), dominated by the vacuum cryostat stability.
LNA input impedance at 4 K	(75 ± 5) Ω	Optimization algorithm on S_{11} measurement (Fig. 4.19).
LNA internal length at 4 K	$\epsilon_r^{-1/2}(38 \pm 1)$ mm	derived from phase subtraction of cold measurements (Fig. 4.20).
Switch ports internal length at 4 K	±2°	derived from phase subtraction of cold measurements (Fig. 4.20).
Accuracy in derived phase measurements for different thermal cycles	0.03 %	Six identical measurements with a full warm-up and cool-down cycle of the vacuum cryostat (Section 4.2.2).
SP6T [64] stability at room temperature	0.15 dB, 0.4°	48 h stability measurement of S_{21} (Fig. 4.12), phase dominated by VNA stability.

Continued on next page

Table C.1 – continued from previous page

Variable	**Uncertainty σ**	**How it was Obtained**
SP6T [64] stability at 4 K	0.2 dB, 1°	stability study measuring S_{11} for different standards and radiating open ports. Dominated by vacuum cryostat Fig. 4.12.
SP6T switching reproducibility at room temperature	0.1 dB, 1.4°	ten full counter-clockwise switching cycles from throw 6 to 1 in decreasing order, measuring S_{21} (Table 4.2).
SP6T switching reproducibility at 4 K	0.1 dB, 0.5°	ten full counter-clockwise switching cycles from throw 6 to 1 in decreasing order, measuring S_{11} (Fig. 4.15).
User-induced reproducibility	TBD	Systematic uncertainty induced by changes in torque applied for each connection to mount the full setup.
One-port cryogenic calibration	TBD	left-over systematics from the one-port semi-automatic calibration using the switch and the calibration standards at 4 K shown in Fig. 4.1.
Power calibration	TBD	Systematic uncertainties from the power calibration proposed with the heated attenuator shown in Fig. 4.1
1D model boost factor	10 %	**ADS model plus Monte Carlo simulation including the sum of the previously determined systematics (Section 4.3).**

References

[1] S. Weinberg, *A new light boson?* Physical Review Letters **40** (1978) 223 (cit. on p. 1).

[2] F. Wilczek, *Problem of Strong P and T Invariance in the Presence of Instantons*, Physical Review Letters **40** (1978) 279 (cit. on p. 1).

[3] A. Ringwald, *Axions and axion-like particles*, arXiv preprint arXiv:1407.0546 (2014) (cit. on p. 1).

[4] J. Smith, E. Purcell, and N. Ramsey, *Experimental limit to the electric dipole moment of the neutron*, Physical Review **108** (1957) 120 (cit. on p. 1).

[5] K. Smith et al., *A search for the electric dipole moment of the neutron*, Physics Letters B **234** (1990) 191 (cit. on p. 1).

[6] C. Abel et al., *Measurement of the permanent electric dipole moment of the neutron*, Physical Review Letters **124** (2020) 081803 (cit. on p. 1).

[7] V. Plakkot and S. Hoof, *Anomaly ratio distributions of hadronic axion models with multiple heavy quarks*, Physical Review D **104** (2021) 075017 (cit. on pp. 1, 7).

[8] R. D. Peccei and H. R. Quinn, *CP Conservation in the Presence of Instantons*, Phys. Rev. Lett **38** (1977) 1440 (cit. on p. 1).

[9] L. Di Luzio, F. Mescia, and E. Nardi, *Window for preferred axion models*, Physical Review D **96** (2017) 075003 (cit. on p. 1).

[10] D. J. Marsh, *Axion cosmology*, Physics Reports **643** (2016) 1 (cit. on p. 1).

[11] J. Preskill, M. B. Wise, and F. Wilczek, *Cosmology of the invisible axion*, Physics Letters B **120** (1983) 127 (cit. on p. 1).

[12] P. Sikivie, “Axion cosmology,” *Axions: Theory, Cosmology, and Experimental Searches*, Springer, 2008 19 (cit. on p. 1).

[13] G. Bertone and D. Hooper, *History of dark matter*, Reviews of Modern Physics **90** (2018) 045002 (cit. on p. 1).

[14] A. H. Peter, *Dark matter: a brief review*, arXiv preprint arXiv:1201.3942 (2012) (cit. on p. 1).

[15] I. G. Irastorza and J. Redondo, *New experimental approaches in the search for axion-like particles*, Progress in Particle and Nuclear Physics **102** (2018) 89 (cit. on p. 2).

[16] W. DeRocco, P. W. Graham, and S. Rajendran, *Exploring the robustness of stellar cooling constraints on light particles*, Physical Review D **102** (2020) 075015 (cit. on p. 2).

[17] P. W. Graham, I. G. Irastorza, S. K. Lamoreaux, A. Lindner, and K. A. van Bibber, *Experimental searches for the axion and axion-like particles*, Annual Review of Nuclear and Particle Science **65** (2015) 485 (cit. on p. 2).

[18] A. Hook, *TASI lectures on the strong CP problem and axions*, arXiv preprint arXiv:1812.02669 (2018) (cit. on p. 2).

[19] C. Bartram et al., *Axion dark matter experiment: Run 1B analysis details*, Physical Review D **103** (2021) 032002 (cit. on pp. 2, 3, 8, 39, 68).

[20] P. Sikivie and Q. Yang, *Bose-Einstein condensation of dark matter axions*, Physical Review Letters **103** (2009) 111301 (cit. on p. 3).

[21] A. Caldwell et al., *A new experimental approach to probe QCD axion dark matter in the mass range above 40 μeV*, The European physical journal/C **79** (2019) 186 (cit. on pp. 3–5).

[22] P. Sikivie, *Experimental tests of the" invisible" axion*, Physical Review Letters **51** (1983) 1415 (cit. on p. 3).

[23] O. Kwon et al., *First results from an axion haloscope at capp around 10.7 μ ev*, Physical Review Letters **126** (2021) 191802 (cit. on p. 3).

[24] B. T. McAllister et al., *The ORGAN experiment: An axion haloscope above 15 GHz*, Physics of the dark universe **18** (2017) 67 (cit. on p. 3).

[25] D. Alesini et al., *Search for invisible axion dark matter of mass m a= 43 μ eV with the QUAX–a γ experiment*, Physical Review D **103** (2021) 102004 (cit. on p. 3).

[26] B. Brubaker, L. Zhong, S. Lamoreaux, K. Lehnert, and K. van Bibber, *HAYSTAC axion search analysis procedure*, Physical Review D **96** (2017) 123008 (cit. on pp. 3, 8, 39).

[27] I. G. Irastorza et al., *Towards a new generation axion helioscope*, Journal of Cosmology and Astroparticle Physics **2011** (2011) 013 (cit. on p. 3).

[28] E. Arik et al., *Probing eV-scale axions with CAST*, Journal of Cosmology and Astroparticle Physics **2009** (2009) 008 (cit. on pp. 3, 7).

[29] T. Dafni and J. Galán, *Digging into Axion Physics with (Baby) IAXO*, Universe **8** (2022) 37 (cit. on p. 3).

[30] A. J. Millar, J. Redondo, and F. D. Steffen, *Dielectric haloscopes: sensitivity to the axion dark matter velocity*, Journal of Cosmology and Astroparticle Physics **2017** (2017) 006 (cit. on pp. 3, 4).

[31] J. Jaeckel and J. Redondo, *Resonant to broadband searches for cold dark matter consisting of weakly interacting slim particles*, Physical Review D **88** (2013) 115002 (cit. on p. 3).

[32] T. Hortala, *MADMAX and CERN's Morpurgo magnet*, https://home.cern/news/news/experiments/madmax-and-cerns-morpurgo-magnet, Accessed on September 11 2023 (cit. on p. 5).

[33] S. Beurthey et al., *Usage of the CERN MORPURGO magnet for the MADMAX prototype*, tech. rep., 2020 (cit. on p. 6).

[34] K. Yau, E. Dacquay, I. Sarkas, and S. P. Voinigescu, *Device and IC characterization above 100 GHz*, IEEE Microwave Magazine **13** (2012) 30 (cit. on p. 8).

[35] S. Shahramian, Y. Baeyens, N. Kaneda, and Y.-K. Chen, *A 70–100 GHz direct-conversion transmitter and receiver phased array chipset demonstrating 10 Gb/s wireless link*, IEEE Journal of Solid-State Circuits **48** (2013) 1113 (cit. on p. 8).

[36] L. Ranzani, L. Spietz, Z. Popovic, and J. Aumentado, *Two-port microwave calibration at millikelvin temperatures*, Review of scientific instruments **84** (2013) (cit. on pp. 8, 45, 49, 68).

[37] J. Gong, Y. Chen, F. Sebastiano, E. Charbon, and M. Babaie, "19.3 A 200dB FoM 4-to-5GHz cryogenic oscillator with an automatic common-mode resonance calibration for quantum computing applications," *2020 IEEE International Solid-State Circuits Conference-(ISSCC)*, IEEE, 2020 308 (cit. on p. 8).

[38] D. M. Pozar, *Microwave engineering*, John wiley & sons, 2011 (cit. on pp. 10, 11, 14–18, 49).

[39] J. D. Kraus, M. Tiuri, A. V. Räisänen, and T. D. Carr, *Radio astronomy*, vol. 66, McGraw-Hill New York, 1966 (cit. on pp. 11, 18).

[40] ElectronicsTutorials, *Phasor Diagrams and Phasor Algebra*, https://www.electronics-tutorials.ws/de/actheorie/phasor-diagramme.html, Accessed on September 21 2023 (cit. on p. 12).

[41] K. Microwave, *Why measuring the calibration standards on a VNA results in arcs, not dots on a Smith Chart as most people expect.* https://www.kirkbymicrowave.co.uk/Support/FAQ/Why-do-I-not-see-a-dot-on-the-Smith-Chart-for-the-opens-and-shorts/, Accessed on September 11 2023 (cit. on p. 13).

[42] F. Caspers, *RF engineering basic concepts: S-parameters*, https://cds.cern.ch/record/1415639/files/p67.pdf, Accessed on September 3 2023 (cit. on p. 14).

[43] L. A. Glasser, *An Analysis of Microwave De-Embedding Errors (Technical Notes)*, IEEE Transactions on Microwave Theory and Techniques **26** (1978) 379 (cit. on p. 14).

[44] C.-C. Chiong, Y. Wang, K.-C. Chang, and H. Wang, *Low-noise amplifier for next-generation radio astronomy telescopes: Review of the state-of-the-art cryogenic LNAs in the most challenging applications*, IEEE Microwave Magazine **23** (2021) 31 (cit. on p. 15).

[45] S. Kamalijam, A. Arvandi, M. Ashtarayeh, B. Safaei, and A. M. H. Monazzah, "A novel LNA circuit in the L band with the purpose of increasing gain in GSM & GPS in wireless multi-receiver systems," *2019 2nd International Conference on Communication Engineering and Technology (ICCET)*, IEEE, 2019 112 (cit. on p. 15).

[46] A. Álvarez Melcón et al., *First results of the CAST-RADES haloscope search for axions at 34.67 μeV*, Journal of High Energy Physics **2021** (2021) 1 (cit. on p. 15).

[47] S. Withington, *Quantum electronics for fundamental physics*, Contemporary Physics **63** (2022) 116 (cit. on p. 15).

[48] B. Schiek, H.-J. Siweris, and I. Rolfes, *Noise in high-frequency circuits and oscillators*, John Wiley & Sons, 2006 (cit. on p. 15).

[49] C. University, *Summary of trigonometric identities - Product identities*, `https://www2.clarku.edu/faculty/djoyce/trig/identities.html`, Accessed on September 16th 2023 (cit. on p. 18).

[50] H. Landau, *Sampling, data transmission, and the Nyquist rate*, Proceedings of the IEEE **55** (1967) 1701 (cit. on p. 18).

[51] Keysight, *N9040B UXA X-Series Signal Analyzer, Multi-touch*, `https://www.keysight.com/de/de/assets/7018-04541/data-sheets/5992-0090.pdf`, Accessed on September 16th 2023 (cit. on pp. 18, 26).

[52] *VectorStar MS464xB Series VNA Technical Data Sheet*, `https://dl.cdn-anritsu.com/en-us/test-measurement/files/Brochures-Datasheets-Catalogs/datasheet/11410-00611AL.pdf`, Accessed on August 29 2023 (cit. on pp. 19, 27, 47, 81).

[53] *UVNA-63 Application Note Error Correction*, `https://www.minicircuits.com/app/AN49-016.pdf`, Accessed on September 2 2023 (cit. on pp. 19, 45, 46, 49).

[54] Scikit-rf, *One-port tiered calibration*, `https://scikit-rf.readthedocs.io/en/latest/examples/metrology`, Accessed on September 4 2023 (cit. on p. 19).

[55] D. Rytting, *Network Analyzer Error Models and Calibration Methods*, `https://www.rfmentor.com/sites/default/files/NA_Error_Models_and_Cal_Methods.pdf`, Accessed on September 2 2023 (cit. on pp. 19, 44, 46).

[56] *LNF-LNC6_20D 6-20 GHz Cryogenic Low Noise Amplifier*, `https://quantummicrowave.com/wp-content/uploads/2016/10/lnf-lnc6_20d.pdf`, Accessed on August 29 2023 (cit. on pp. 26, 42, 64).

[57] L. N. Factory, *Manual LNF-PS3b Low Noise HEMT Power Supply*, `https://lownoisefactory.com/wp-content/uploads/2023/06/lnf-ps3b_.pdf`, Accessed on September 24 2023 (cit. on p. 26).

[58] M. electronic, *Keysight Technologies E3620A and E3630A Non-programmable DC Power Supplies*, `https://www.meilhaus.de/cosmoshop/default/articleMedia/e3630a/de/Datasheet_Keysight_E3620A-E3630A_en.pdf`, Accessed on September 24 2023 (cit. on p. 26).

[59] C. Lee, X. LiJ, D. Strom, O. Reimann, M. Collaboration, et al., "MADMAX: a QCD dark matter axion direct-detection experiment," *Journal of Physics: Conference Series*, vol. 2156, 1, IOP Publishing, 2021 012041 (cit. on p. 30).

[60] L. S. cryotronics, *Model 475 Specifications*, `https://www.lakeshore.com/products/categories/specification/magnetic-products/gaussmeters-teslameters/model-475-dsp-gaussmeter`, Accessed on September 20th 2023 (cit. on p. 37).

[61] F. Beaujean, A. Caldwell, and O. Reimann, *Is the bump significant? An axion-search example*, The European Physical Journal C **78** (2018) 1 (cit. on p. 39).

[62] Radiall, *R570F32000 Datenblatt (PDF)*, `https://www.mouser.de/datasheet/2/516/R570F32000-2502229.pdf`, Accessed on September 3 2023 (cit. on p. 42).

[63] *Elite 1.5-40 GHz Directional Coupler*, `https://www.markimicrowave.com/Assets/datasheets/CE10-1R540.pdf?v=072822`, Accessed on August 29 2023 (cit. on pp. 43, 68).

[64] *SPnT Coaxial Subminiature Switches DC to 6 GHz, DC to 26.5 GHz, DC to 40 GHz*, `https://www.mouser.de/datasheet/2/516/R591_Generic_TDS_09_02_18-1595491.pdf`, Accessed on August 29 2023 (cit. on pp. 44, 81, 82).

[65] H. Wang et al., *Cryogenic single-port calibration for superconducting microwave resonator measurements*, Quantum Science and Technology **6** (2021) 035015 (cit. on pp. 45, 68).

[66] M. Stanley, S. De Graaf, T. Hönigl-Decrinis, T. Lindström, and N. M. Ridler, *Characterizing scattering parameters of superconducting quantum integrated circuits at milli-Kelvin temperatures*, IEEE Access **10** (2022) 43376 (cit. on p. 45).

[67] A. Rumiantsev and N. Ridler, *VNA calibration*, IEEE Microwave magazine **9** (2008) 86 (cit. on p. 47).

[68] Keysight, *PathWave Advanced Design System (ADS)*, `https://www.keysight.com/us/en/products/software/pathwave-design-software/pathwave-advanced-design-system.html`, Accessed on September 24 2023 (cit. on p. 71).

List of Tables

Acronyms

ADS Advanced Design System. 70, 71

ALP Axion-like particle. 7, 20, 25, 32, 41, 45, 55, 74

B Magnetic. 37, 76, 77

CB-100 Closed Booster 100mm. 6, 7, 15, 17, 20–23, 25, 26, 30, 32–34, 37, 41, 43–45, 53, 64, 65, 68, 70, 71, 73, 74

CERN European Organization for Nuclear Research. 5–7, 25, 26, 28–30, 32–34, 37, 73

CET Central European Time. 76

CP Charge-Parity. 1

DAQ Data acquisition. 31–34, 37, 39, 75–78

DC Direct Current. 26, 44, 55, 58, 59, 77

DUT Device Under Test. 11, 14, 18–20, 44, 52, 53

ENR Excess Noise Ratio. 17, 26

FFT Fast Fourier Transform. 29

fk-fk female-2.92mm to female-2.92mm connectors. 62

FPGA Field Programmable Gate Array. 29

GPIB General Purpose Interface Bus. 34

LAN Local Area Network. 34

LHe Liquid helium. 51–53

LN2 Liquid nitrogen. 51, 52

LNA Low Noise Amplifier. 15–17, 20, 22, 23, 25–28, 30, 33, 34, 42, 44, 45, 52, 64–68, 71, 73, 77

MADMAX MAgnetized Disc and Mirror Axion eXperiment. 1, 3–8, 15, 17, 21, 25, 32, 34, 37, 41, 68, 71, 73

MADMON MADmax MONitoring system. 32, 33, 39, 77

mk-mk male-2.92mm to male-2.92mm connectors. 26

MPP Max Planck Institute for Physics. 5, 6, 25, 26, 28–31, 34, 55

PT Platinum resistance Thermometer. 34, 77

QCD Quantum Chromodynamics. 1, 4, 7

RBW Resolution BandWidth. 18, 38

RF Radiofrequency. 6, 7, 9, 10, 13–15, 18, 19, 28, 43, 51–53, 55, 59, 60, 62, 67, 68, 73, 74

RFI Radiofrequency Interference. 25, 30

RMS Root Mean Square. 36, 39

SA Spectrum Analyzer. 17, 18, 20, 22, 25, 26, 28–31, 36, 39, 42, 43, 45, 67, 74, 76–78

SNR Signal to Noise ratio. 46

SOA Short-Open-Attenuator. 49, 74

SOL Short-Open-Load. 49

SP2T Single port double throw switch. 42, 44, 45

SP6T Single port six throws switch. 44, 55

TE Tranverse electric mode. 30

UPS Uninterruptible power supply. 31

USB Universal Serial Bus. 34

UTC Universal Time Coordinated. 35, 76

VNA Vector Network Analyzer. 10, 12, 14, 19–21, 27, 42–51, 53, 54, 56, 57, 59, 60, 64, 68, 73